AD/A-007 032

COHERENT OPTICAL ADAPTIVE TECHNIQUES (COAT)

J. E. Pearson, et al

Hughes Research Laboratories

Prepared for:

Rome Air Development Center
Advanced Research Projects Agency

January 1975

UNCLASSIFIED

SECURITY CLASSIFICATION OF THIS PAGE *(When Data Entered)*

REPORT DOCUMENTATION PAGE		READ INSTRUCTIONS BEFORE COMPLETING FORM
1. REPORT NUMBER RADC-TR-75-46	2. GOVT ACCESSION NO.	3. RECIPIENT'S CATALOG NUMBER AD/A-007032
4. TITLE *(and Subtitle)* Coherent Optical Adaptive Techniques (COAT)		5. TYPE OF REPORT & PERIOD COVERED Final - Quarterly Tech Rpt 5 27 Mar 73 to 30 Jun 74
		6. PERFORMING ORG. REPORT NUMBER Quarterly Tech. Rpt 5
7. AUTHOR(s) J.E. Pearson R.M. Kubo W.B. Bridges T.J. Walsh L.S. Horwitz		8. CONTRACT OR GRANT NUMBER(s) F30602-73-C-0248
9. PERFORMING ORGANIZATION NAME AND ADDRESS Hughes Research Laboratories 3011 Malibu Canyon Road Malibu, Calif. 90265		10. PROGRAM ELEMENT, PROJECT, TASK AREA & WORK UNIT NUMBERS PE: 62301E JON: 12790016
11. CONTROLLING OFFICE NAME AND ADDRESS Defense Advanced Research Projects Agency 1400 Wilson Blvd Arlington, Va. 22209		12. REPORT DATE January 1975 13. NUMBER OF PAGES 148
14. MONITORING AGENCY NAME & ADDRESS *(if different from Controlling Office)* Rome Air Development Center (OCTM) Griffiss AFB, NY 13441		15. SECURITY CLASS. *(of this report)* UNCLASSIFIED 15a. DECLASSIFICATION/DOWNGRADING SCHEDULE

16. DISTRIBUTION STATEMENT *(of this Report)*
Approved for public release. Distribution unlimited.

17. DISTRIBUTION STATEMENT *(of the abstract entered in Block 20, if different from Report)*
Approved for public release. Distribution unlimited.

18. SUPPLEMENTARY NOTES
Robert F. Ogrodnik
RADC (OCTM)
AC315 330-4306

19. KEY WORDS *(Continue on reverse side if necessary and identify by block number)*
Laser Phased Array
Adaptive Optics
Atmospheric Turbulence and Thermal Blooming Compensation

20. ABSTRACT *(Continue on reverse side if necessary and identify by block number)*
Coherent Optical Adaptive Techniques (COAT) are designed to overcome degradations experienced by optical beams propagating in media with fixed or time-varying distortions. This report summarizes the status and operating characteristics of an experimental, visible wavelength, eighteen-element, self-adaptive optical phased array. Measurements on a well-characterized outdoor 100m propagation range have proved that such a system can remove almost all beam distortions produced by atmospheric turbulence. The system (cont)

DD FORM 1 JAN 73 1473 EDITION OF 1 NOV 65 IS OBSOLETE

UNCLASSIFIED

SECURITY CLASSIFICATION OF THIS PAGE *(When Data Entered)*

Item 20. Abstract (cont)

has demonstrated its ability to form a beam with a diffraction-limited beam-width and with 60% of the diffraction-limited peak intensity for turbulence levels characterized by structure constants (C^2_N) ranging from 1 X 10^{-16} $cm^{-2/3}$ to 6 X 10^{-14} $cm^{-2/3}$. Convergence times for the 18-element multidither system range from 1.5 to 3.0 xm for a servo system with a 400 Hz unity gain bandwidth. Spectral analysis of the COAT correction signals indicates, however, that only a 50 Hz bandwidth is required for correction to within tenth-wave residual wave front errors for static targets, even in strong turbulence. The experimental phase error spectra agree well with theoretical calculations which use a Von Karman spectrum for the refractive index fluctuations. Multiple glint discrimination and tracking of the strongest glint in a multiple target is demonstrated in high turbulence. Good tracking is observed at rates up to 14 mrad/s. The convergence stability of the COAT system is excellent, limited only by the inability of pure phase control to remove gross atmospheric beam steering effects. Receiver aperture size has had no appreciable effect on system performance except in multiple glint cases where the glints are within 1 to 2 db in net reflectance. A design is presented for a gas absorption cell to be used for scaled studies of convection-dominated thermal blooming.

COHERENT OPTICAL ADAPTIVE TECHNIQUES (COAT)

J. E. Pearson
W. B. Bridges
L. S. Horwitz
R. M. Kubo
T. J. Walsh

Contractor: Hughes Research Laboratories
Contract Number: F30602-73-C-0248
Effective Date of Contract: 27 March 1973
Contract Expiration Date: 30 June 1974
Amount of Contract: $307,692.00
Program Code Number: 3E20
Period of Work Covered: 27 Mar 73 - 20 Jun 74

Principal Investigator: J. E. Pearson
Phone: 213 456-6411

Project Engineer: R. F. Ogrodnik
Phone: 315 330-4306

Contract Engineer: R. Hawkins
Phone: 315 330-4731

This research was supported by the Defense Advanced Research Projects Agency of the Department of Defense and was monitored by Robert F. Ogrodnik, RADC (OCTM) GAFB NY 13441 under Contract F30602-73-C-0248.

ib

This report has been reviewed by the RADC Information Office (OI) and is releasable to the National Technical Information Service (NTIS). At NTIS it will be available to the general public, including foreign nations.

This technical report has been reviewed and is approved for publication.

APPROVED: Robert F. Ogrodnik

ROBERT F. OGRODNIK
Project Engineer

TABLE OF CONTENTS

LIST OF ILLUSTRATIONS

FOREWORD

This quarterly report was prepared by Hughes Research Laboratories, Malibu, California, under Contract F30602-73-C-0248. It describes work performed from 27 March 1974 to 30 June 1974. The principal investigator is Dr. James E. Pearson and the principal scientist is Dr. William B. Bridges.

SUMMARY

This report covers the fifth and final quarter of the contract from 27 March 1974 to 30 June 1974. The entire quarter has been devoted to performing and analyzing outdoor range measurements with the 18-element visible COAT system built on this contract.

The system hardware and the 100 m rooftop propagation range remain the same as reported during previous quarters. The target has been modified slightly to simplify the data analysis and presentation. The beam incident on the target is now viewed ahead of the target motion mechanism so the beam appears stationary with respect to the moving glints. A calibrated, linear TV camera is now used to view this beam.

The range measurements program includes a careful characterization of the turbulence levels on the propagation range. The atmospheric structure constant, C_N^2, is determined using two microthermometers, and a scintillometer which propagates a 0.6328 μm beam along the entire 100 m path. The instruments indicate that the range is very uniform in its turbulence characteristics and that the turbulence levels cover exactly the range desired for the COAT system tests. That is, the atmospheric correlation length varies from larger than the transmitter diameter to smaller than the width of a single transmitter element. The scintillometer and microthermometer readings correlate very well, but obey a relationship given by C_N(opt) 1.5 C_N (thermal).

The range measurements with the COAT system use single and multiple-glint targets in high and low turbulence. The system performance is nearly independent of the target configuration and the turbulence level. The observed convergence times are 1.5 to 3.0 ms. The COAT-formed beam has a diffraction-limited beamwidth and a peak intensity which is 60% of the diffraction limit. Convergence stability is excellent within the limits imposed by atmospheric beam steering effects. The system will lock onto and track the strongest glint in a multiple glint target at rates up to 14 mrad/s. At higher glint velocities, there is a gradual loss in the peak power formed on the glint. Receiver aperture size or shape has no significant effect on system performance until it becomes too small for sufficient signal-to-noise.

For good multiple glint discrimination, one glint must be at least 2 to 3 dB stronger than any other. With a two-glint target, the beam power will switch between the glints if they do not differ by 2 to 3 dB in net reflectivity. Under very carefully controlled conditions and with two equal glints (within 1 dB), we have observed power sharing: the COAT system forms the beam on two resolved glints simultaneously. This effect is observed even with large receiver apertures. Any change in glint position, relative glint strength, or receiver size or position, however, will cause the COAT system to pick one glint while ignoring the other.

Spectral analyses of the COAT-generated phase correction signals show that significant errors (larger than one-tenth wave) are present only at frequencies below 50 Hz. This observation is valid for stationary targets in any level of turbulence. At very low frequencies (2 to 5 Hz), peak-to-peak phase errors of 1.3 wavelengths are observed. The fast response of the RADC/COAT system is thus not essential here except for achieving rapid convergence. For situations which involve moving targets, slewing beams, or strong transverse winds, however, the 500 Hz response of this system will be required. The experimental phase error spectra agree well with theoretical calculations which use a Von Karman refractive index spectrum.

A gas absorption cell design is presented. The cell is to be used with the 18-element RADC/COAT system in laboratory-scaled studies of COAT correction for thermal blooming. The design has a stationary cell and uses a single moving mirror to produce a transverse "wind" (motion of the optical beam relative to the gas). The design is such that the output beam is always stationary so the beam analysis and target arrangement are simplified.

On the basis of this measurement program and work performed earlier on this contract, the principal conclusions of our work are as follows:

1. A multidither COAT system can produce a nearly diffraction-limited beam even for propagation through very strong turbulence. Residual errors in the optical system are also removed without affecting the turbulence compensation performance. The servo electronics for such a COAT system are relatively simple and can be compact and all solid-state.

2. The turbulence correction performance is not degraded by moving, multiple glint targets.

3. Moving targets can be tracked at rates exceeding 10 mrad/s.

4. Correction bandwidths of 50 Hz are sufficient for turbulence correction with static targets. Bandwidths up to the 500 Hz limit of the RADC/COAT system will be necessary for moving targets and slewing beams.

5. Peak-to-peak phase errors on the order of 1.3 wavelengths are present in strong turbulence for a 15 mm diameter beam transmitted across a 100 m path.

6. Adaptive xy-pointing control is desirable to remove atmospheric beam steering which cannot be removed by transmitter phase control.

7. Offset-pointing is straightforward to implement with this type of COAT system using sample-and-hold circuitry in the servo electronics. Pointing can be done either mechanically with microslewing mirrors or electronically using preprogrammed phase control of the transmit aperture.

8. Since the transmitter diameter, range, and turbulence levels can be scaled to scenarios of interest at 10.6 μm and 3.8 μm, all of the conclusions presented here based on visible wavelength results also apply to the infrared wavelengths.

I. INTRODUCTION

This document is the fifth quarterly report on Contract F30602-73-C-0248 and also serves as the final contract report. Follow-on Contract F30602-75-C-0001 beginning 2 July 1974 is a direct continuation of the work completed under the present contract and uses the 0.488 μm, 18-element, multidither COAT system built and developed under this program.

A. Program Objectives

There are two primary objectives of this program. The first objective is to determine the performance limits of coherent optical adaptive techniques through operation of an experimental, visible prototype multidither COAT system through a representative turbulent atmosphere against a complex dynamic target. The second objective is to determine the best methods of employing COAT in high power laser systems and to assess the status of necessary key high power components.

B. Organization of This Report

This report covers the range measurements phase of the contract during which detailed studies were made on COAT compensation for atmospheric turbulence using the 18-element visible system developed earlier in the contract. The report is written in the form of a final report to provide an overall summary of the contract work.

Section II summarizes the final configurations of the 18-element COAT system optics and electronics and of the target and propagation range. Some comments are made on the good and bad features of the hardware with some suggestions for future improvements.

Section III presents the results and analysis of the range measurements. The performance of the three atmospheric monitoring instruments, a scintillometer and two microthermometers, is discussed in detail. The COAT system performance under high and low turbulence conditions is presented with single and multiple glint targets, both stationary and moving.

Preceding page blank

Section IV contains the design for a gas absorbtion cell to be used in studies of scaled, convection-dominated thermal blooming. A novel method of wind generation provides a simple cell construction and facilitates output beam analysis.

Section V summarizes the important conclusions about COAT correction for turbulence based on the range measurements data. The report concludes with Section VI outlining suggestions for future work using the visible, 18-element RADC COAT system and the computer simulations developed on this contract and on other contracts.

Two addendums are part of this report. The first is a 16 mm movie and its associated script. The movie contains sequences from the range data showing the dynamic nature of the COAT system turbulence compensation. The second addendum is a report covering Task 3 of the contract statement of work: an assessment of high power COAT systems and associated key high power components. This Task 3 report will be published in a separate volume, and will contain Hughes Aircraft proprietary material.

II. SYSTEM HARDWARE SUMMARY

Most of the important features of the hardware involved in the RADC/COAT system have been presented in the four previous quarterly reports.[1-4] The block diagram shown in Fig. 1 illustrates the principal parts of the system, including the 18-element output array pattern. A few changes were implemented as we gained experience in using the system on range. This section summarizes the current configuration of various parts of the system. Suggestions for possible future changes or additions are also presented.

A. Target

The original target design[2] allowed for simultaneous viewing of the target plane and the beam profile incident on the target. This arrangement proved to be undesirable for a number of reasons. First, the target and beam images were reversed with respect to each other so that some mental correction was necessary to interpret the video presentation. Second, the usable camera magnification was limited by the target geometry leading to undesirably small images of the beam incident on the target. Third, the glints appeared stationary at all times. For stationary single or multiple glint runs, the split image thus provided no information which was useful on a continuous basis; a few video frames would be sufficient to record the glint positions although they were immediately obvious from observing where the COAT system formed the beam. For moving glints, the light beam appeared to move while the glints remained stationary. Although no detriment to analyzing system performance, this type of display is unappealing for visual presentation and much of the impact of the effective way the system can track a moving glint is lost.

The target configuration used for most of our tests employed a beam splitter ahead of the moving mirror as shown schematically in Fig. 2. The technique of achieving glint motion is similar to that discussed previously[2] and the physical layout is similar to that illustrated in the last report,[4] but with the beam splitter now placed ahead of the turning mirrors, the TV camera sees the stationary beam as it arrives at the target after transmission by the COAT system. The glint position information is not recorded

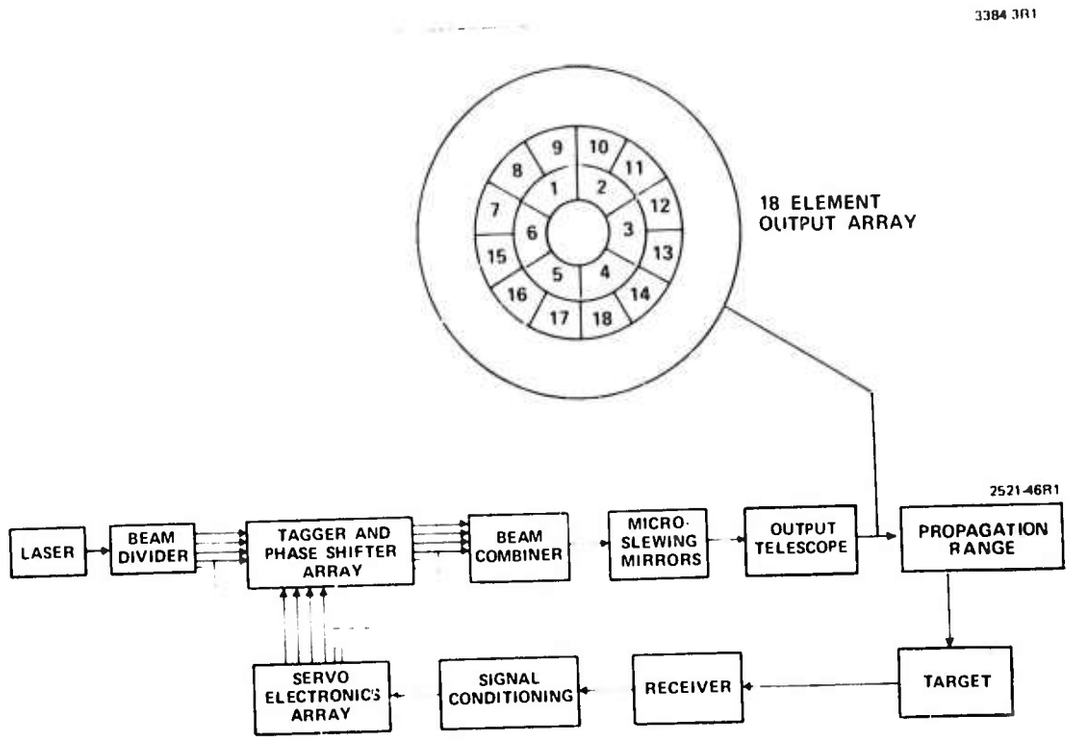

Fig. 1. 13-element system block diagram.

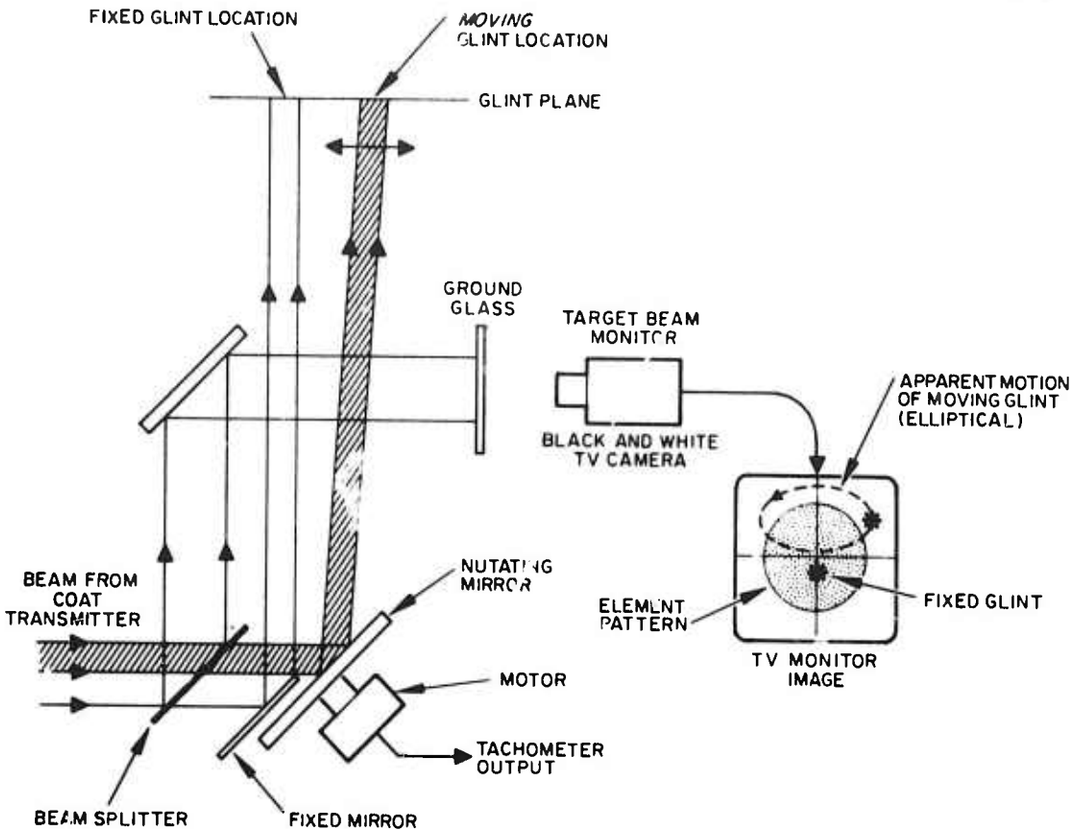

Fig. 2. Schematic of target configuration used in range measurements.

with the video data. Figure 3 illustrates a typical data sequence of one glint moving along an elliptical track with respect to one fixed glint. The pictures are taken directly off the black and white TV monitor which is fed by the target beam camera. The video data are much easier to interpret and the action of the COAT system is much more striking. The added complexity necessary to simultaneously view the glint plane has been removed since the information is of marginal value and can be conveniently recorded in a data notebook. The TV camera can now be adjusted so that the element pattern nearly fills the viewing screen.

If further improvement on this target is desired for any future work, the fixed and nutating mirrors could be replaced by a 50% beam splitter. One beam would be directed onto stationary glints and the other onto moving glints. Glint motion could be accomplished by any one of three methods: (1) moving the glints, (2) moving the beam splitter (provides linear glint motion), (3) moving a secondary mirror (simple angular scan for linear motion or nutating scan for elliptical motion). This arrangement has the advantage that two glints can be put in any relative position, even on top of each other. Also, since linear glint motion is easier to put in a computer program, it is more desirable for comparisons with computer simulation results.

B. Target Analysis Equipment

The target analysis equipment has also been described earlier.[3,4] The high speed motion picture camera discussed in earlier reports has not been used because the light levels avilable were too low for the fast frame rate even when using 1600 ASA film. The principal equipment used is listed in Table I. The equipment has proved to be adequate for recording and analyzing all the desired system performance data. Minor future improvements which would make data acquisition more convenient would include pause and single-frame controls on the video tape recorder and a low-frequency spectrum analyzer to replace the slower wave analyzer for spectral data. A video screen splitter together with a second TV camera could be used to simultaneously record the target configuration when desired.

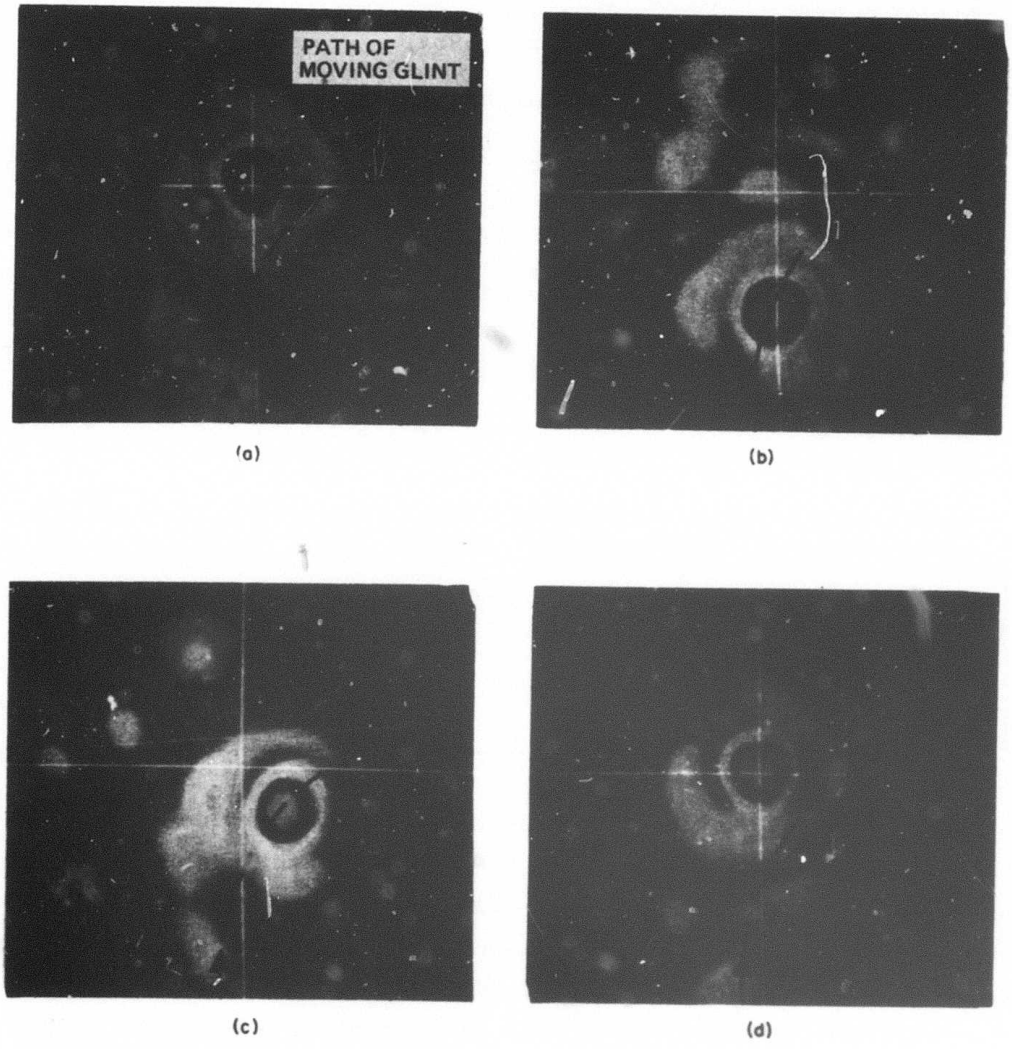

Fig. 3. Single frame TV monitor pictures illustrating a typical data sequence of a strong glint moving near a weaker glint as the moving glint comes into the transmitted element pattern. (a) Beam locked on stationary boresight glint, (b) and (c) COAT system selects the stronger moving glint and maintains a beam maximum on it. (d) Moving glint passes out of transmitter field of view; beam reforms on stationary glint.

TABLE I

Target Analysis Equipment Used in Range Measurements

Flat field, linear response black and white TV camera for monitoring formed beam at target (Cohu model 6954)
Black and white TV monitor (Concord model MR-700)
Image analyzer (color quantizer). (Interpretation Systems Inc. model VP-8)
Color TV monitor (Sony KV1710, 17 in. screen)
Cassette video tape recorder for permanent video records (Sony model VO-1600)
Photodetectors behind each glint for monitoring power on target
Oscilloscope displays (regular and stored mode) for observing power on glints and profile outputs from the color quantizer
Wave analyzer (Quan-Tech model 304DTL) for spectral data on glint power, receiver signals, control voltages, etc.
Multichannel instrumentation recorder (Ampex model FR1300A) for real-time records of control voltages, glint power, etc.
Polaroid and 35 mm still and super 8 motion cameras for permanent records

The image analyzer or "color quantizer" is a device which slices the black and white video signal into eight discrete and adjustable levels and then assigns a color to each level. When the output of this device is viewed on a color TV monitor, the result is a color display with each color corresponding to a different intensity level (actually, the borders between colors are the isointensity contours of the video frame). If a black and white monitor is used, the result is similar, but with an 8-level gray scale. Figure 4 shows two views of the COAT-formed beam pattern for a glint on the boresight axis. Figure 4(a) is a black and white photograph taken off a color monitor, and Fig. 4(b) is the same scene photographed off a black and white monitor. The image analyzer also has yz or xz, and xyz displays (x and y are target plane coordinates and z is intensity). Figure 5(a) is an example

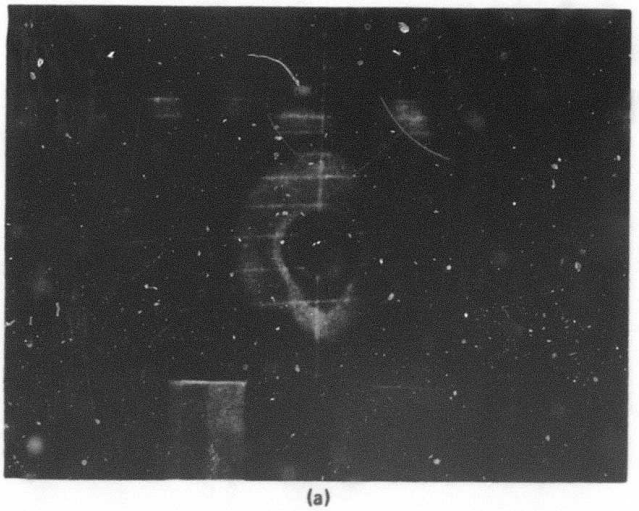

(a)

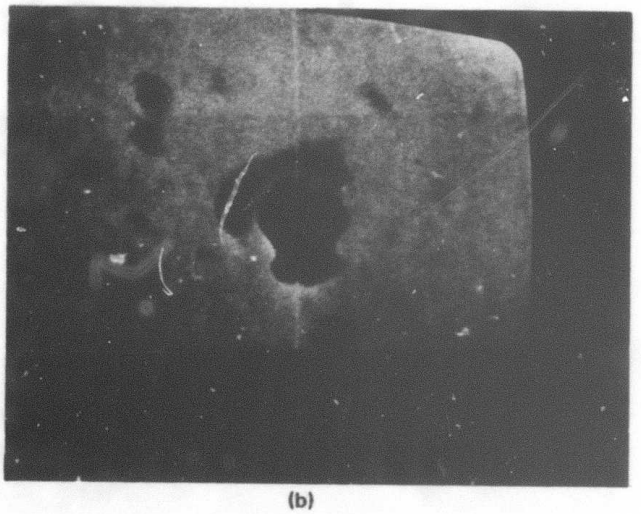

(b)

Fig. 4.
Black and white photographs of TV monitor displays of target beam monitor camera for a single boresight glint. (a) Color monitor image. (b) Black and white monitor image. The scales at the bottom show the colors or gray scale for intensity increasing left to right and 1.5 dB between levels.

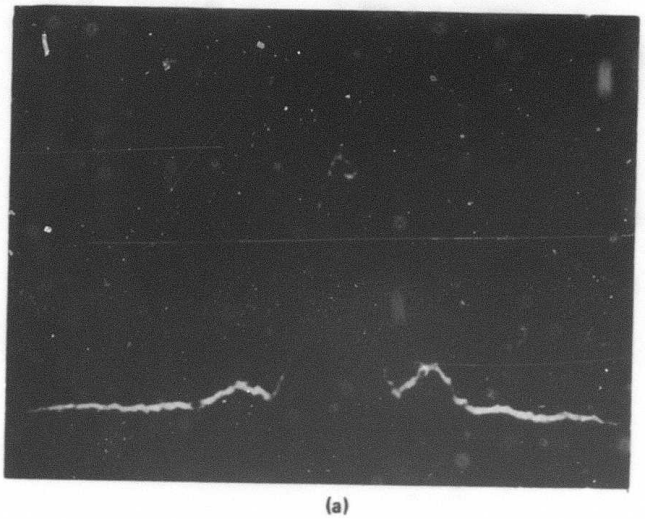

(a)

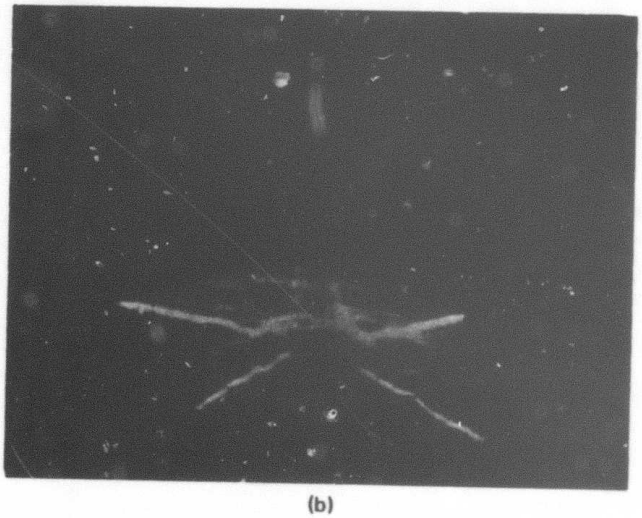

(b)

Fig. 5.
Examples of 2-D and 3-D display outputs of image analyzer corresponding to the photographs in Fig. 4. (a) xz display; cut taken along horizontal cursor shown in Fig. 3. (b) xyz display.

of the xz display corresponding to the same case as Fig. 4 with the cut taken along the horizontal cursor shown in Fig. 4; Fig. 5(b) is the corresponding xyz display.

C. Propagation Range

The propagation range is located at the Hughes Ground Systems Group (GSG) facility in Fullerton, California. It consists of a 6 m path in the laboratory where the COAT transmitter/receiver is located, 10 m in a periscope which connects the laboratory to the rooftop range, and 92 m across a white rock roof at a height of 1 m. A number of precautions were taken to ensure negligible turbulence in the periscope.[4] A view of the range looking from the periscope toward the target enclosure is shown in Fig. 6. The range has been very satisfactory for our tests. The uniformity of the path made it easy to characterize the turbulence in terms of the atmospheric structure constant, C_N and sufficient turbulence was produced on sunny days to significantly degrade a non-COAT-corrected beam.

The uniformity of the propagation path was checked by using two differential microthermometer instruments[2] (ΔT units) to simultaneously measure C_N at two locations. One unit was placed at midrange and the other one either near the periscope or near the target. Figure 7 shows typical results of these measurements and the excellent correlation between different instruments. Figure 7(a) plots the values of C_N measured at the target as a function of C_N measured at midrange and Fig. 7(b) compares C_N measured by the two instruments when they are both at the midrange location. The straight line fit to the data was obtained by a linear regression analysis. The square of the linear correlation coefficient, ρ_{xy}, measures the amount of variation in y that can be attributed to a variation in x according to the relation $Y = Ax + B$. The coefficient is defined by the following expression[5]:

$$\rho_{xy} = \pm \left[\frac{\text{explained variation in y}}{\text{total variation in y}} \right]^{1/2} = \pm \left[\frac{\langle (Y - \langle y \rangle)^2 \rangle}{\langle (y - \langle y \rangle)^2 \rangle} \right]^{1/2} \quad (1)$$

where the data points are (x_i, y_i) and the brackets indicate an ensemble average given by

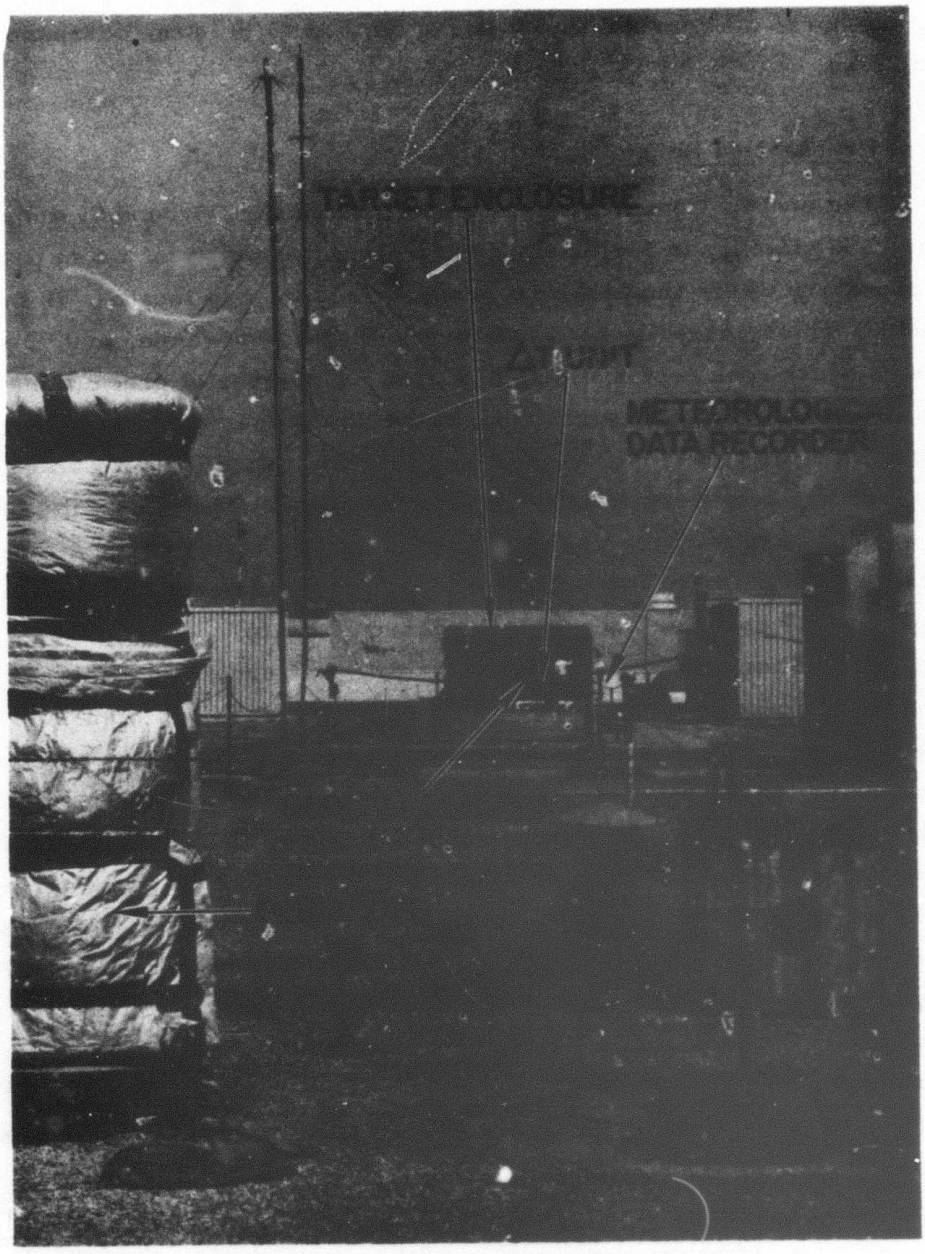

Fig. 6. Photograph of the 92m rooftop portion of GSG propagation range. View is looking toward the target from the periscope which connects the laboratory to the range.

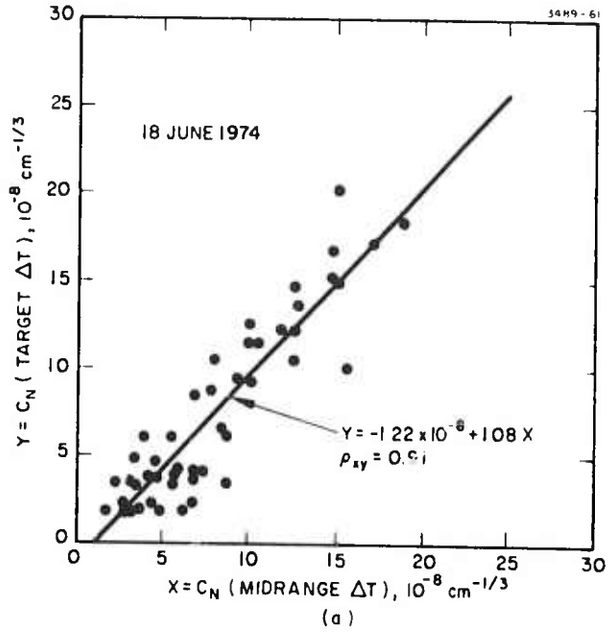

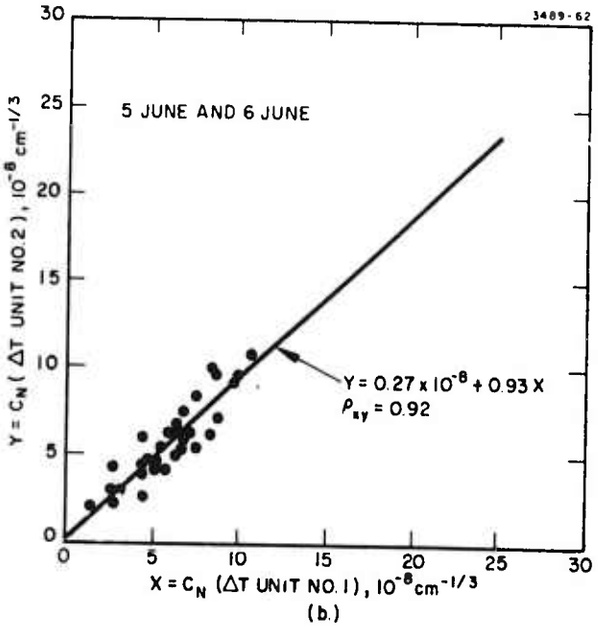

Fig. 7.
Comparison of C_N measured simultaneously at different locations along the rooftop propagation path with two separate differential microthermometers (ΔT units). (a) C_N measured near the target versus C_N at midrange. (b) C_N as measured by the two different ΔT units placed at the same location. The correlation coefficient, ρ_{xy}, is defined in the text.

$$\langle u \rangle = \frac{1}{N} \sum_{i=1}^{N} u_i \,. \qquad (2)$$

The value of ρ_{xy} ranges from 0 for completely uncorrelated data to ± 1 for linearly correlated data which exactly obey the relationship $y = Ax + B$.

The data in Fig. 7(b) indicate that the two T units are nearly identical since they track very closely when both are measuring C_N at the same location (the probe pairs were within 10 cm of each other). The large correlation coefficient of the data in Fig. 7(a) indicates that the propagation path is homogeneous to within 17% which is essentially the same as the 16% tracking error between the two ΔT units. This result provides us with some confidence in using a point measurement technique to derive an integrated-path quantity like C_N. More detailed discussions of the atmospheric measurements are given in Section III of this report.

D. Optics

1. System in General

The schematic diagram of the complete RADC/COAT transmitter/receiver shown in Fig. 8 illustrates the relative arrangement of the various optical components. A photograph of the system in the range laboratory (Fig. 9) shows the system and the periscope which connects the lab to the range. As discussed in earlier reports, every effort was made to use low loss, high quality optics throughout the system. All surfaces of mirrors and beam splitters are 1/4-wave or better, but no special coatings for antireflection or enhanced reflection were employed. The result is an optical system of low distortion, but fairly high loss. Table II lists the measured losses from the laser output through each optical element to the final system output. For 500 mW out of the laser (its maximum), we can put approximately 18 mW into the periscope, 12 mW onto the target, and 7×10^{-2} mW onto the glint detector (located behind an N. D. = 2.0 filter).

These low powers have caused no difficulty with our measurements except that we were unable to use the high speed motion picture camera for recording time resolved convergence sequences. In fact, the usual operating condition was with minimum laser power (~50 mW) which provided the system

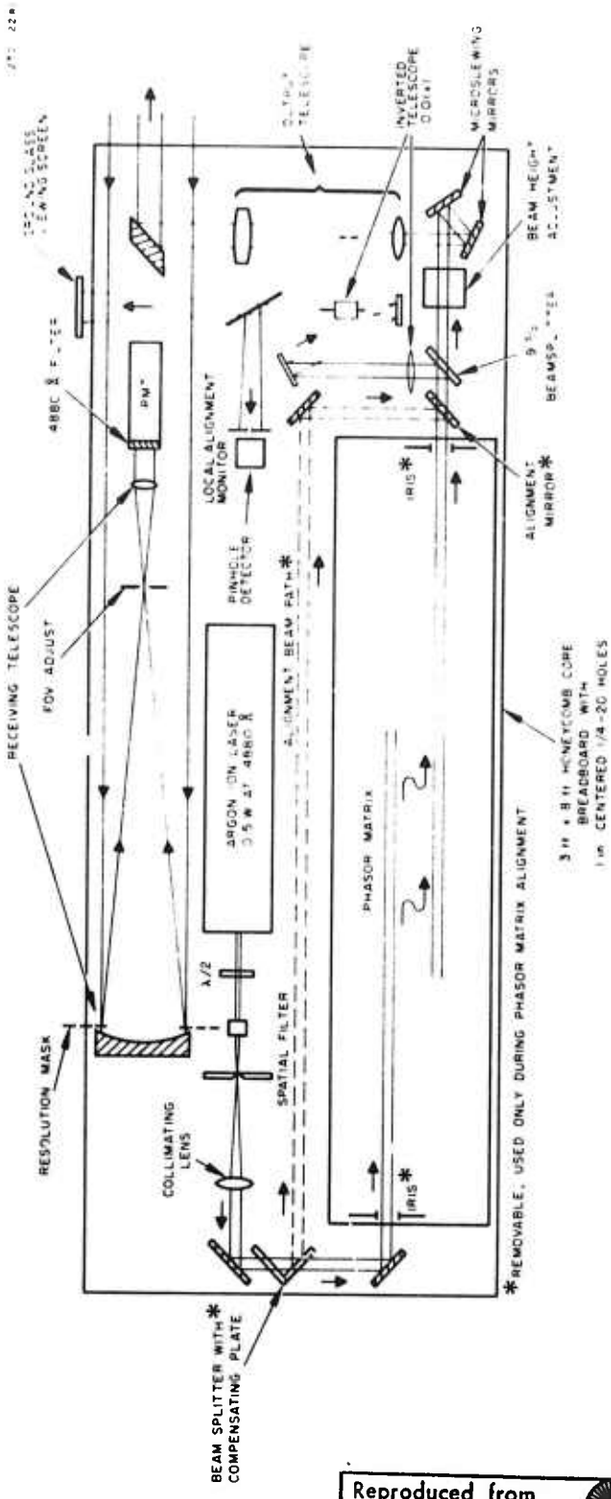

Fig. 8. Schematic of complete COAT transmitter/receiver layout.

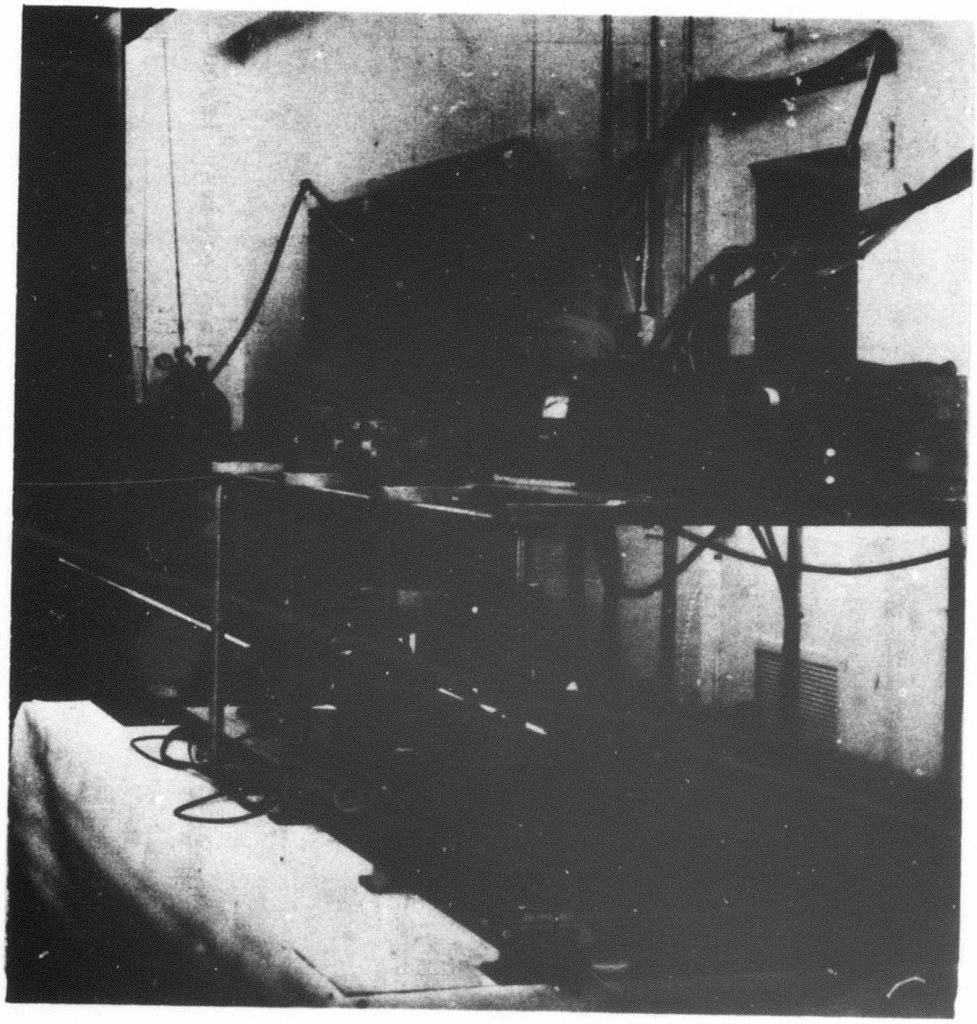

Fig. 9. Photograph of RADC/COAT system in the range laboratory at the Hughes GSG facility. The periscope which takes the beam to the rooftop propagation range can also be seen.

TABLE II

RADC/COAT SYSTEM OPTICAL LOSSES

Element	Transmission	Power Loss, dB
Transmitter		
Complete spatial filter (includes pinhole and objective)	0.71	1.42
Collimating lens	0.93	0.32
Turning mirrors (2)	0.71	1.42
Phasor matrix mirrors (4)	$(0.87)^4 = 0.57$	2.44
Phasor matrix beam splitters (17)	$(0.97)^{17} = 0.60$	2.22
Local alignment beam splitter	0.96	0.18
Height adjusting mirrors (2)	$(0.91)^2 = 0.83$	0.81
Microslewing mirrors (2)	$(0.87)^2 = 0.76$	1.19
Output turning mirror	0.85	0.70
Truncation and central obscuration (20x magnification of laser output)	0.44	3.56
Total	0.037	14.26
Periscope		
Mirrors (2)	$(0.85)^2 = 0.72$	1.42
Windows (2, AR one side)	$(0.95)^2 = 0.90$	0.46
Total	0.65	1.88
Target		
Turning mirror	0.85	0.70
45° beam splitter	0.90	0.46
Glint turning mirror	0.85	0.70
Glint lens	$(0.96)^2 = 0.92$	0.36
Total	0.60	2.22

T1459

with ample signal-to-noise, was sufficient for the target TV monitor, and minimized troubles with the laser. For future work involving thermal blooming studies, however, antireflection and enhanced reflector coatings on the optics will be required to minimize the system losses.

An important feature of the RADC/COAT system optics is the versatility and flexibility which is available in the system. The heart of the transmitter is the phasor matrix which forms the transmitter array pattern and applies the correction signals and dither modulation. The details of the design have been discussed elsewhere,[1,2] but we want to emphasize here that any array pattern containing up to 18 elements can be formed with this design by merely producing the appropriate reflecting patches on the beam splitter/combiner plates. Different array patterns can be put into the system and aligned in less than an hour as we have demonstrated using an 8-element linear array and an 18-element 0-6-12 annular array. Other elements of flexibility in the system listed in Table III provide the operating convenience necessary for a prototype research system.

The one element in the system optics which has not worked as well as we had hoped is the PZT bimorph used for the phase correction. Its sensitivity is adequate but, as noted in an earlier report,[3] the bimorphs do not always move perpendicular to the plane of the phase shifter. The element patterns are thus steered as the dc voltage level on the bimorph changes. A change of ± 120 V can steer some element patterns by as much as 1/2 of an element null-null beamwidth. All the units are not this bad, however. We have devised a technique[6] for overcoming this problem, but its implementation would involve a major redesign of the phasor matrix. Such a change is not warranted on this system now, but might be considered for a future improvement.

2. Propagation Paths

There are two propagation paths, each of which can be used to obtain the focused far-field transmitter diffraction pattern. The first, of course, is the propagation range which includes the periscope and the target. The second is referred to as the "local loop" and consists of an inverted telescope and a pinhole detector. The two paths are shown schematically in Fig. 10 (see also Fig. 8). Either path can be used to obtain the phasing

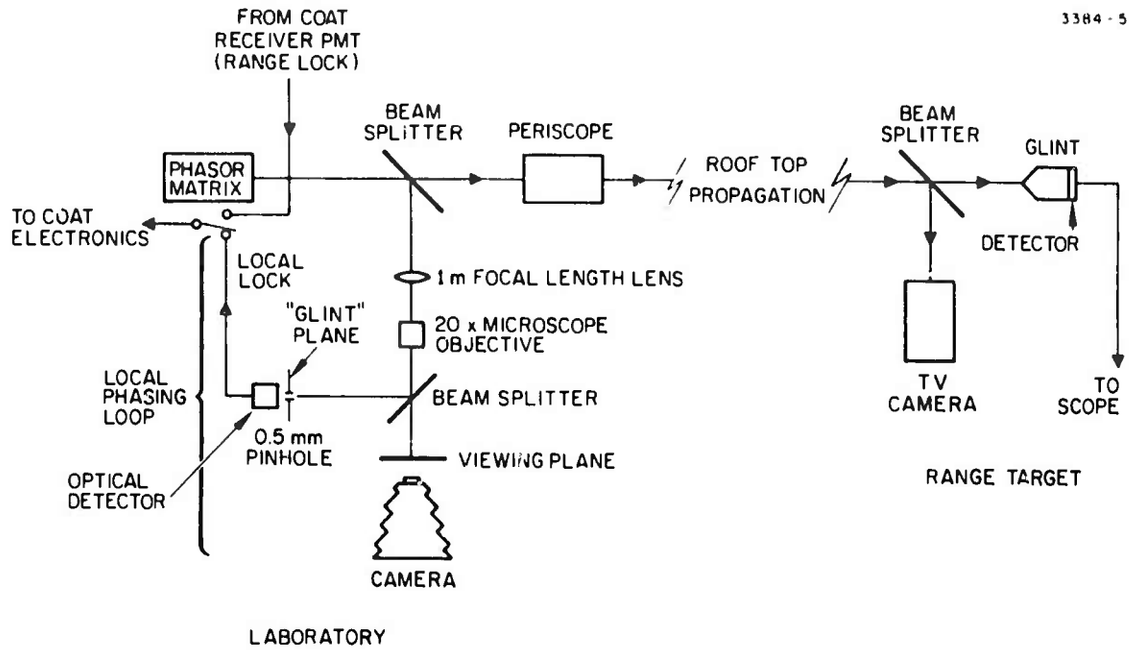

Fig. 10. Schematic of the two propagation paths, each of which can be used to obtain phasing information for the COAT system.

information for the COAT system, so if the two paths both have diffraction-limited optics and no turbulence, a diffraction-limited beam will be formed at both the target plane and the local "glint plane" when the servo loop is closed around a glint placed in either path.

Unfortunately, no special effort was made to use high quality optics in the periscope. The windows are just plate glass which are AR-coated on one side and flat to only a few wavelengths per inch. The mirrors are front-surface reflectors, but also have poor flatness of a few wavelengths per inch. The quality of the target mirrors and target beam splitter are less important since the propagation paths in the target are short; the surfaces there were also flat to no better than a few wavelengths per inch. The imperfect periscope and target optics have no effect on the beam formed by the COAT system at the target, however, since the system can completely correct for static errors as long as the rms errors across the transmit elements do not exceed 1/6 of a wave. In our system the rms errors across an element did not exceed 1/3 wave so most (but not all) of the static errors will be removed by the COAT system.

TABLE III

Flexibility Designed into RADC/COAT System

Any transmit array configuration containing up to 18 elements
Alignment adjustments on each individual element
Electrically-controlled shutter on each element for removing elements from output array
Adjustable output beam height
Output beam steerable in two dimensions by manual mirror or galvanometer-driven microslewing mirrors
Output telescope for adjusting diameter of output beam
Adjustable beam expander/collimator for varying the intensity taper across the transmit beam diameter

The optics in the local loop path were nearly diffraction-limited for the small beam sizes used. The 1 m focal length lens is an air-spaced achromat and the beam splitter has $\lambda/10$ surfaces. The poorest quality element is probably the microscope objective.

Small residual errors in the local loop path and the more substantial errors in the periscope optics caused some problem when the local loop path was used to phase the system with the hope of obtaining a nearly diffraction-limited beam at the range target. The effect of the propagation distortions is shown in Fig. 11 where the observed beams in each path are compared under conditions of very low turbulence (nighttime, $C_N^2 \leq 5 \times 10^{-16}$ cm$^{-2/3}$). The fact that there are different distortions in the two paths is immediately obvious (one beam is well formed, the other is not).

The whole purpose of the local alignment loop was to provide a means of propagating a beam down the range which, in the absence of any turbulence, would form a diffraction-limited intensity pattern on the target. The degradation caused by the atmosphere could then be measured as could the improvement effected by the COAT system. This distortions shown in Fig. 11 make this scheme impractical. We have, however, devised another way to form a nearly diffraction-limited beam at the target. The technique uses the sample-and-hold (S&H) circuitry built into the COAT electronics for use in offset pointing.

The technique uses the COAT system to initially form the beam so that all static distortions in the propagation path are removed. The correction signals are then held for a fixed time before a new sample of the propagation path is taken to update the correction signals. Since the convergence time of the system is 2 to 4 ms (see Ref. 4 and Section III of this report), a sample time of 10 ms is chosen. With very low nighttime turbulence conditions, a hold time is chosen which is as long as possible consistent with no appreciable degradation of the power on target. The results of such a test are shown in Fig. 12 where the power on the target glint is shown for various hold times, τ_H. A value for τ_H between 200 ms and 400 ms appears to be the best choice and is long enough for even moderate atmospheric turbulence to degrade the beam (only 20 to 30 ms required in strong turbulence – $C_N^2 = 1 \times 10^{-14}$ cm$^{-2/3}$). The comparison between (a) and (b) of Fig. 12 shows the imperfection in the S&H circuitry; occasional transients increase the power fluctuations and

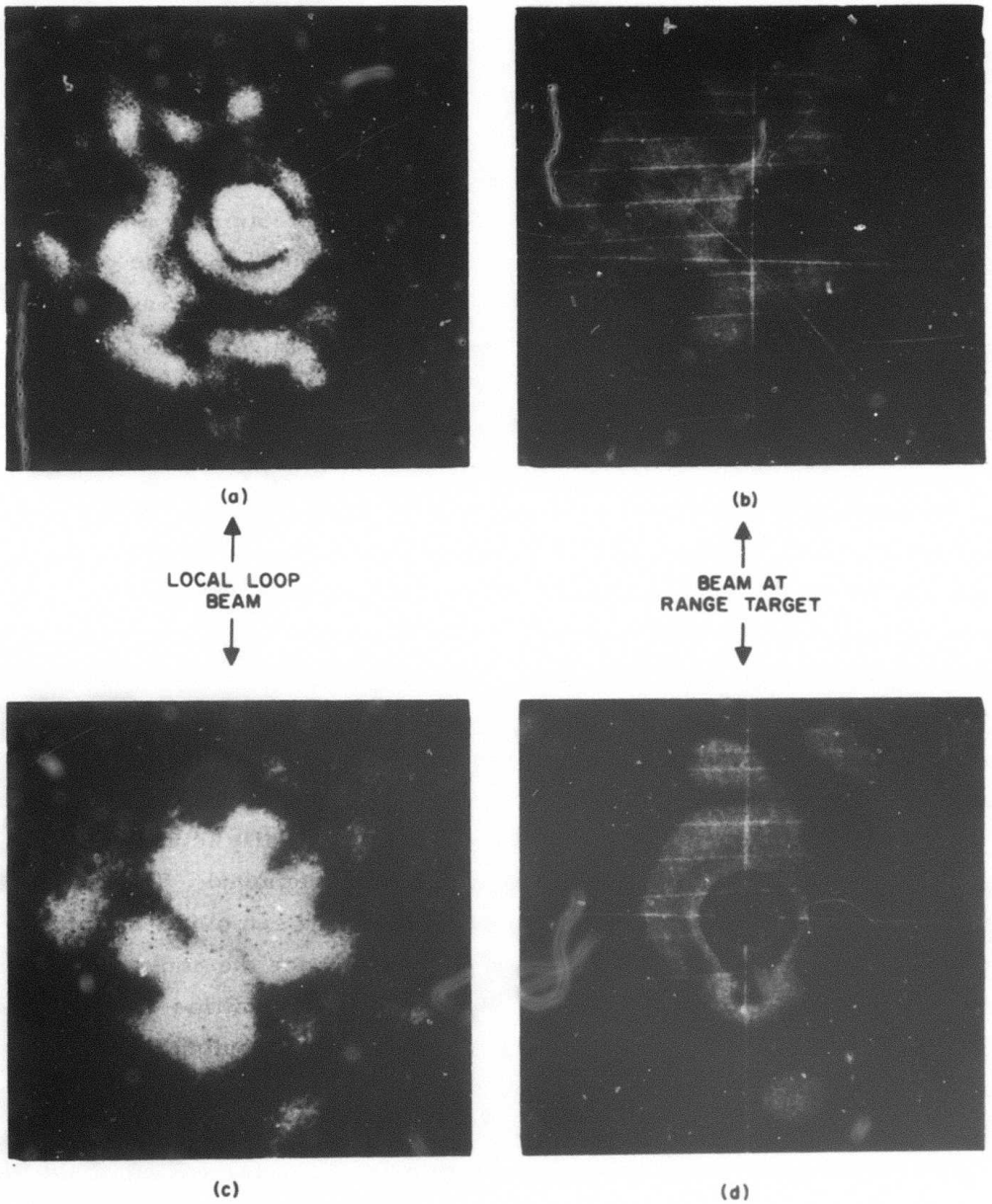

Fig. 11. Comparison of local loop and target beam profiles for very low turbulence. (a) and (b) Local loop lock. (c) and (d) Target glint lock.

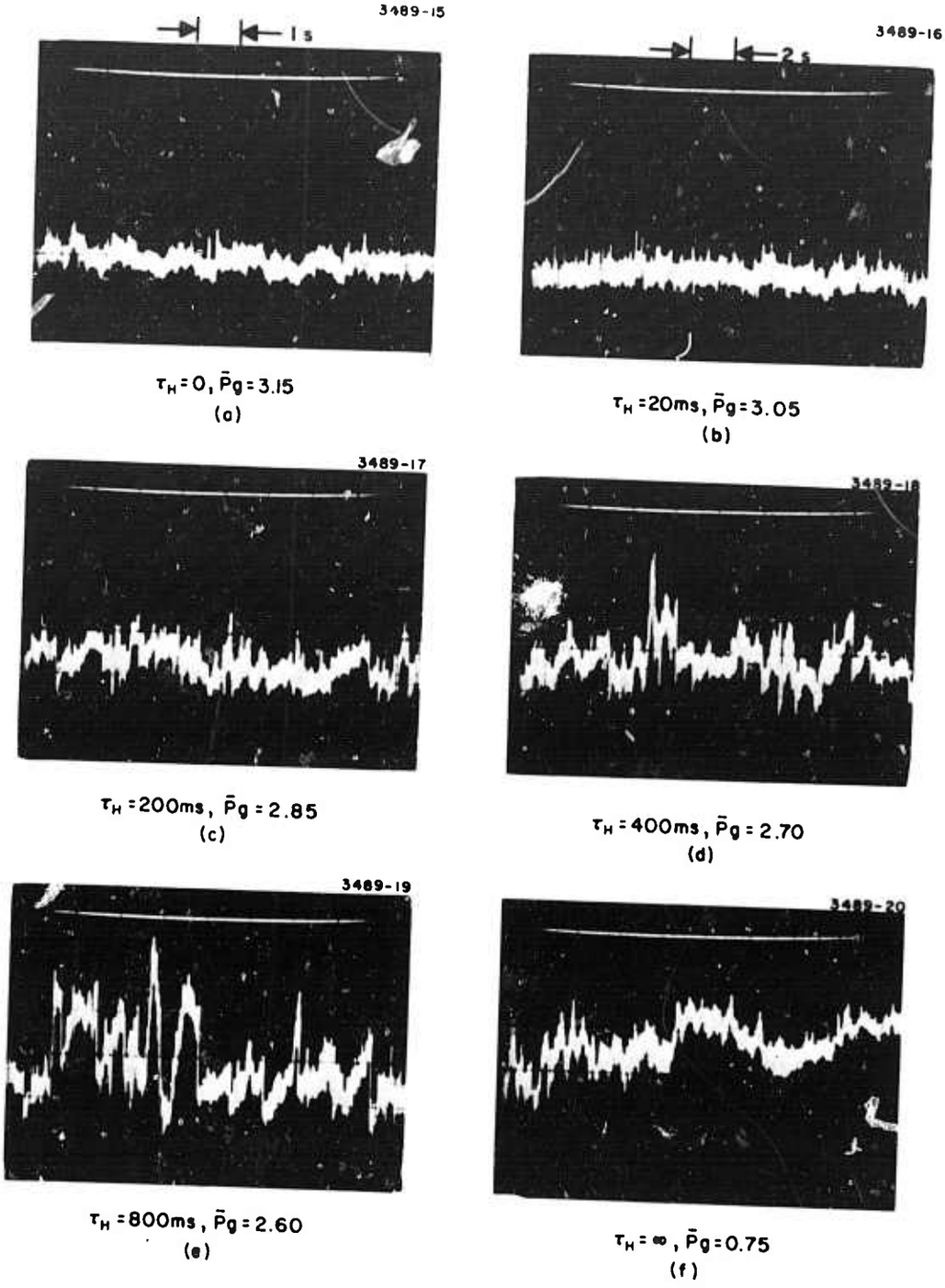

Fig. 12. Test of sample-and-hold alignment technique for a sample time τ_S = 10 ms and various hold times, τ_H. Turbulence level is very low.

reduce the average power by 3-10%. In later sections of this report the term "No COAT Correction" will be employed whenever this S&H technique is used for phasing the array and "COAT OFF" will be used when the servo loop is opened.

E. Electronics

All of the electronics for the RADC/COAT system were designed and built at the Hughes Research Laboratories (HRL). The total cost of the electronics was $20K for parts and $60K for labor, including design. Additional element control channels would cost about $2.3K parts and labor. The functional block diagram of the system in Fig. 13(a) shows that the receiver is a single photomultiplier and that the signal conditioning consists of a preamp, an AGC, a phase reversal switch, a clipper, and a loop gain adjustment. A loop break switch is also provided for "COAT OFF" operation. The available controls on each channel as shown in Fig. 13(b) include various monitor and input points distributed throughout the 5 low-pass filter stages. A photograph of all the all-solid-state electronics including power supplies and two different AGC networks is shown in Fig. 14. Figure 15 is a photograph of 3 two-channel control modules which fit in a standard 19 in. wide rack panel. If desired, it would be a simple matter to significantly reduce the size of the control electronics at the expense of some of the versatility built into this system. Most of the test points and controls shown in Figs. 13 and 15, for example, were put in only for experimental convenience.

One improvement in the servo electronics would be useful. The multipliers used in the synchronous detectors have sufficient thermal drift that substantial dc offsets occur after the dc gain in the low-pass filter. The dc offset is detrimental since it reduces the dynamic range of the correction and can even drive the output amplifiers into saturation.

We attempted to alleviate the offset drift problem by reducing the dc gain following the multipliers.[4] The decrease in loop gain was then made up with ac gain ahead of the multipliers. This scheme did not work very well mainly because of high noise levels in the amplified signal ahead of the multipliers which caused clipping of the signal. Future designs should include

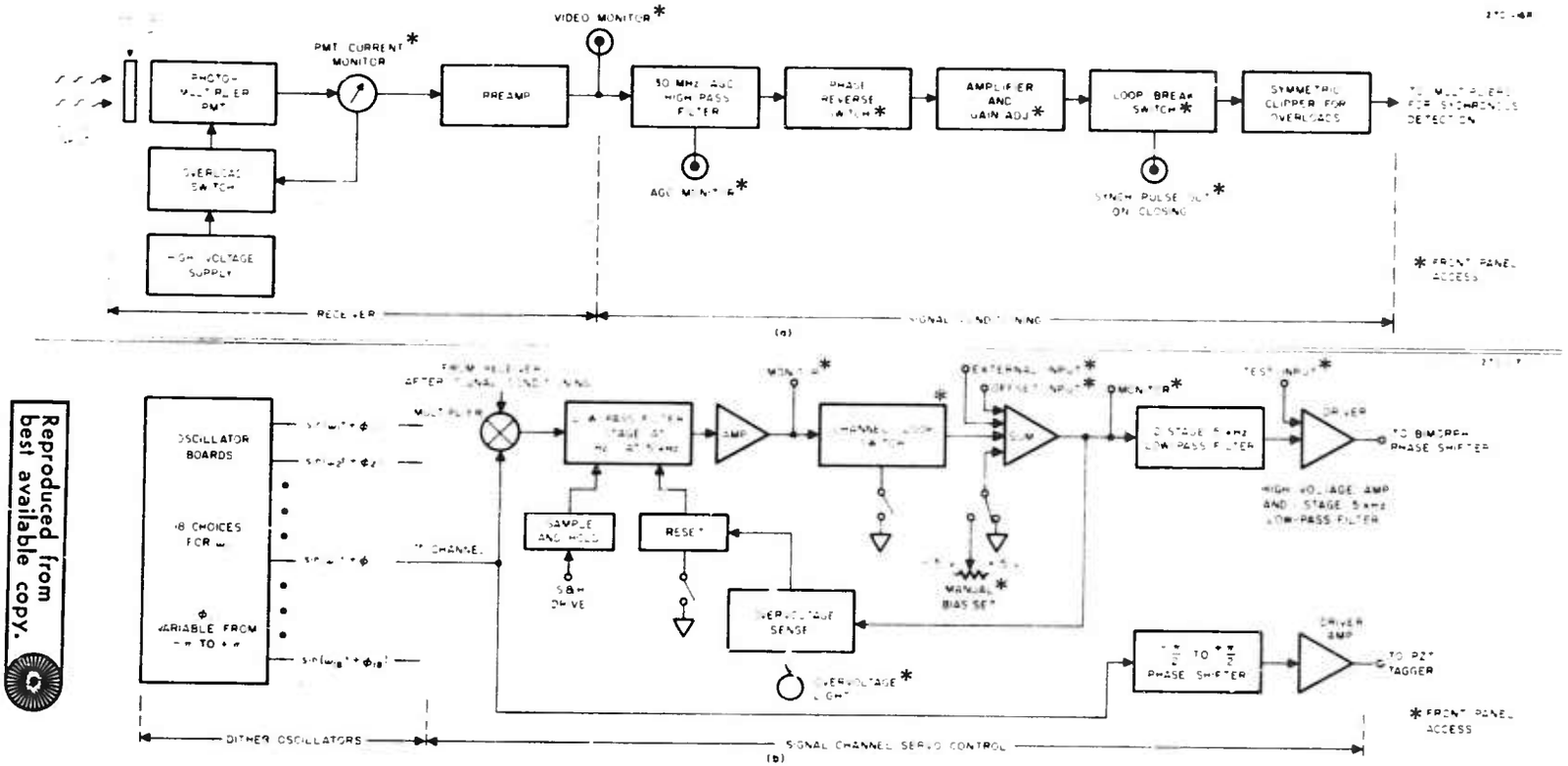

Fig. 13. COAT system block diagram. (a) Receiver and signal-conditioning. (b) Oscillator board and one of the 18 identical servo control channels.

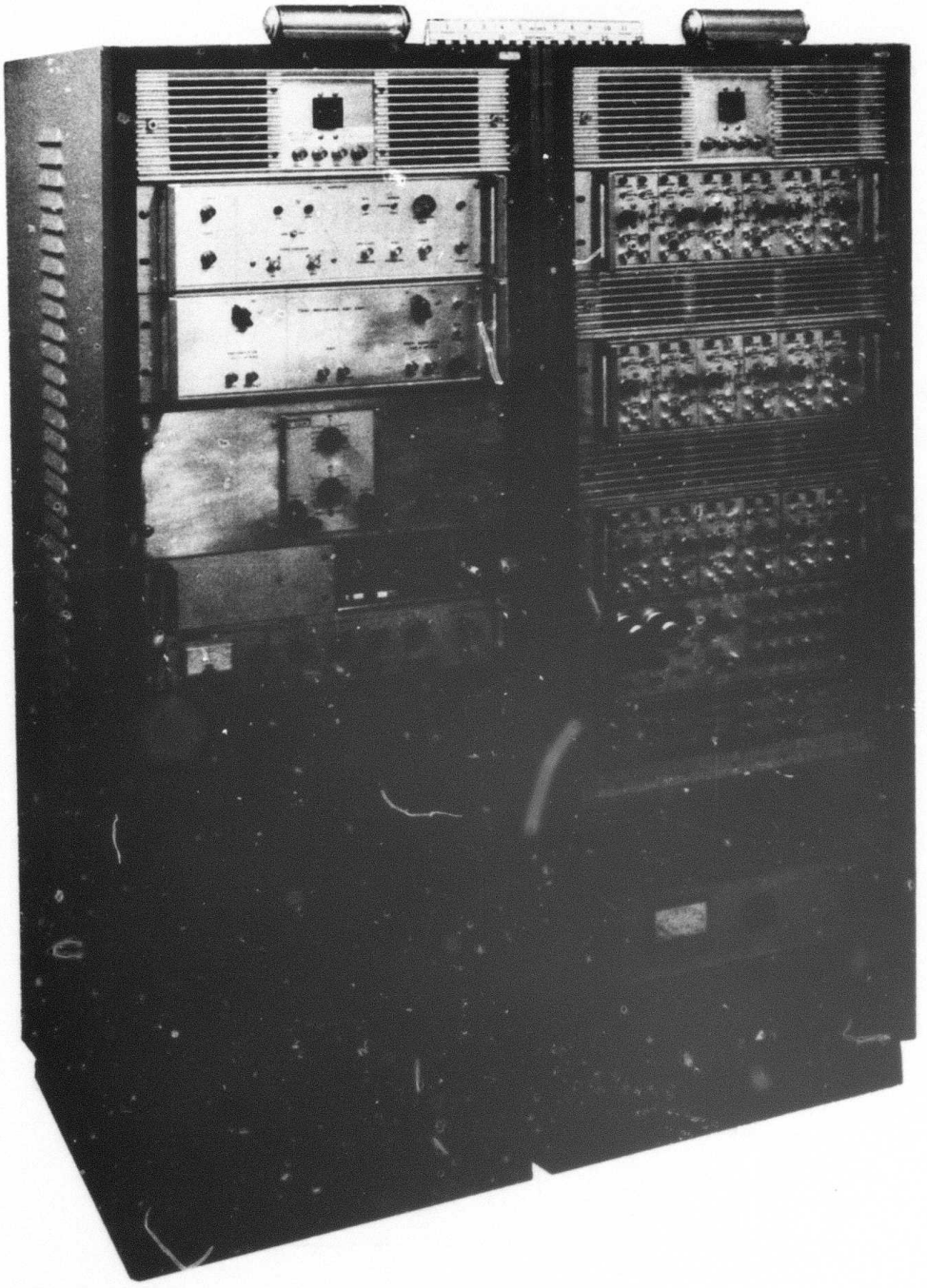

Fig. 14. Photograph of complete RADC/COAT control electronics

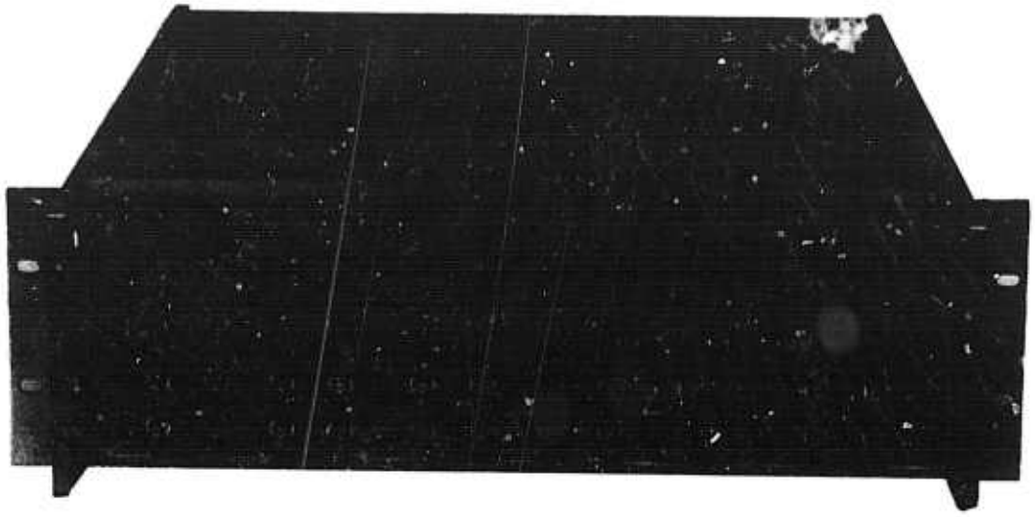

Fig. 15. Photograph of a 6-channel COAT electronics panel. The 18-channel system uses three such panels.

temperature compensation in all of the synchronous detector and low-pass filter stages and video level operation wherever possible.

Since the RADC/COAT system was built as a research tool and not as an operational prototype for a practical COAT system, we designed a great deal of flexibility and versatility into the electronics as well as the optics. Figures 13 and 15 show the numerous test points and controls in the system. The system also has two types of AGC which give comparable performance.[4] We have the capability of selecting three operating modes for the dither frequencies[2]: one frequency per channel, 2 channels for each frequency (sine/cosine), and three channels per frequency (triphase). The phase of each dither frequency can also be independently adjusted. Only the first mode of operation has been experimentally studied in detail using the frequencies shown in Table IV although we have demonstrated sine/cosine operation with the 18-element system. Time has not allowed a test of triphase performance except by computer simulation.

TABLE IV

Tagger Frequencies for 18-Channel COAT System

f_1 =	8.2 kHz	f_{10} =	20.8 kHz
f_2 =	9.6 kHz	f_{11} =	22.2 kHz
f_3 =	11.0 kHz	f_{12} =	23.6 kHz
f_4 =	12.4 kHz	f_{13} =	25.0 kHz
f_5 =	13.8 kHz	f_{14} =	26.4 kHz
f_6 =	15.2 kHz	f_{15} =	27.8 kHz
f_7 =	16.6 kHz	f_{16} =	29.2 kHz
f_8 =	18.0 kHz	f_{17} =	30.6 kHz
f_9 =	19.4 kHz	f_{18} =	32.0 kHz

T1117

The design of the servo electronics was optimized using a computer simulation.[2,3] The parameters studied included the number and corner frequency locations of high-pass and low-pass filters, dither frequencies and spacings, minimum signal-to-noise ratio, open loop gain, and dither amplitude. The final values used include a five-stage low pass filter as listed in Tables IV and V.

The simulation also provided other information about the COAT servo, some of which was surprising. In studying the dither frequencies and relative phases, we found that many channels could be driven with one frequency if the relative phases were chosen correctly. At first, this result seemed to indicate that many channels could be accommodated in a small dither band. Further investigation revealed, however, that for comparable system performance no real saving in dither bandw du results from using more than 2 channels per dither frequency (sine/cosine); sine/cosine operation gives optimum performance for a fixed total dither bandwidth. We did find, however, that the two channels on one frequency do not have to be exactly 90% out of phase, but could have relative phases from 70° to 110° with no detriment to the system performance. The implication is that the servo channels can be coupled rather strongly without affecting the performance of the COAT system. This conclusion may take on greater significance in systems which have actuator nonlinearities (such as hysteresis[4]) or mechanical element couplings (deformable mirrors).

TABLE V

COAT Servo Design Values

1.	Minimum dither frequency spacing, $\Delta f = 1.4$ kHz. Smaller Δf requires lower loop gain for stability; lower gain gives slower response.
2.	Low-pass filter: 1 stage at f = 10 Hz, 4 stages at f = 5 kHz.
3.	High-pass filter: 1 stage at f = 1 kHz, 1 stage at f = 170 Hz.
4.	Dither amplitude = $\pm 20^{\circ}$.
5.	Maximum open loop gain = 38 dB.

F. Conclusions

The outstanding feature of the RADC/COAT system is that it works beautifully. Not only does it perform the adaptive phase corrections extremely well as shown in earlier reports[3,4] and discussed later in this report, but it does the job reliably and reproducibly. To date, the electronics have been 100% reliable, requiring no servicing or adjustments since the first installation in the system (this record includes a shipment from HRL at Malibu to the Hughes GSG propagation range at Fullerton). The optics, including the laser, have a similar record although the laser output window requires cleaning about once a month and the phasor matrix requires a minor daily alignment to boresight all the elements. The reliability and accuracy of the design and the effectiveness of the system as a research tool has been conclusively proved by our experiments. The conclusions resulting from the experiments performed on this contract and from additional planned experiments with the system should lead to valid design guidelines and data for future practical COAT systems.

III. RANGE MEASUREMENTS

Measurement of the performance of the RADC COAT system in compensating for real atmospheric turbulence is the second of the three major tasks on this contract. The first task was the design, construction, and laboratory test of the system and the third task is a high power design study to assess key component status and to derive design guidelines for turbulence compensation in high energy laser systems. The first four technical reports[1-4] on this contract have covered the first task requirements and Task 3 will be discussed in a separate proprietary addendum to this report. This chapter presents the results of our 3-1/2 month measurements program using the RADC/COAT system on the 100 m outdoor propagation range at the Hughes Ground Systems Group (GSG) facility in Fullerton, California.

A. Atmospheric Data — Range Characterization

1. Instrumentation

Three instruments have been used to characterize the atmosphere in terms of C_N, the atmospheric structure constant. These instruments are a scintillometer and two differential microthermometers (ΔT) units which are placed at two locations along the propagation path. The scintillometer is an integrated path measure of C_N while a ΔT measurement samples the turbulence at only one point along the propagation path. The rooftop range is very uniform and flat with no hot air sources such as vents or blowers nearby (see Fig. 6) and the periscope has negligible turbulence.[4] This fact plus the good agreement between ΔT units spaced 50 m apart (see Fig. 7) means the point measurement should be as reliable as the integrated path measurement.

The instruments have performed reliably although each one has its own peculiar problems. The ΔT unit sensors have two probes which use 3 W tungsten light bulbs with their glass envelopes removed.* Each of these probes is connected to one arm of a bridge circuit, the output of which is amplified before the rms value is taken.[2] Since dR/dT of tungsten is known

*We are grateful to G. R. Ochs of NOAA for suggesting this technique.

the units are calibrated daily by switching into one arm of the bridge a resistance equivalent to a 1.0°C difference in temperature at the probes. A 100 s averaging time is normally used during data collection and a 0.1 Hz low frequency cutoff is built into the instrument.

The light bulbs are inexpensive and convenient to use, but they become noisy after being used for 2 to 5 days and must be replaced. The noise is apparently caused by oxidation at the contacts. We have used silver paint and conductive epoxy to improve the probe lifetime, but usually new bulbs are required after one week of use. The light bulb filaments are also fairly large (40 to 60 μm) and thus have long response times which limit their frequency response to 30 to 50 Hz. After discussions with G.R. Ochs of NOAA, we initially felt this response would be sufficient for measuring C_T to get C_N. As discussed in the next section, however, the spectrum of the turbulence on the rooftop range may exceed 150 Hz. Any future work with these instruments on this kind of range should thus use 2 to 4 μm diameter, fast response filaments.[7]

The scintillometer should be the best measure of turbulence along the propagation path since it samples almost the identical path as the COAT transmitter beam. We have used a single pass down the 100 m range rather than the 200 m double-pass arrangement discussed previously.[4] This short path length is close to the minimum value[8] for the validity of the theory which relates C_N^2 to scintillation.[9,10] The discrepancy between theory and what is measured by the instrument at this range can become quite large if the turbulence inner scale size exceeds 1 mm.[11] The 100 m path was forced on us, however, by vibrations and thermal drift in the retromirror mount and in the periscope mirror mounts.[4] For all our measurements, the 0.6328 μm He-Ne scintillometer beam used the same periscope mirrors as the COAT transmitter. The 3 mW He-Ne laser was mounted on an I-beam bolted to the building sidewall just behind the target enclosure (see Fig. 6). The natural laser divergence of 0.75 mrad was used to produce a beam diameter of about 8 cm incident on the 1 mm receiver aperture.

One other annoying problem with the scintillometer is excessive 60 cycle pickup and noise in the electronics. This noise produces an offset in the rms output of the device which depends on the light level at the detector. The amount of the offset is shown in Fig. 16. An alignment adjustment is required two or three times daily to keep the noise level within the noted region. Note that the offset error in C_N at the center of the operating region is 1×10^{-8} $cm^{-1/3}$ which can be as much as 50% of the minimum value of C_N observed during low turbulence periods. It is also obvious from Fig. 16 why a larger divergence was not added to the scintillometer laser. Even a factor of two increase in the beam divergence would lower the power at the detector by a factor of four and increase the offset error in C_N to 6×10^{-8} $cm^{-1/3}$. For reference purposes, the log-amp output voltage for zero light onto the scintillometer detector is -11.2 V.

2. Measurements

The value of C_N was computed from the rms temperature fluctuations measured with the ΔT units using the following relationship[12]:

$$C_N = \frac{7.76 \times 10^{-5}}{r^{1/3}} \left(\frac{P}{T^2}\right)\left(1 + \frac{0.00752}{\lambda^2}\right)\langle(\Delta T)^2\rangle_{ave}^{1/2} \qquad (3)$$

where r is the spacing of the two probes, P is the atmospheric pressure in millibars, T is the ambient temperature in ^{o}K, λ is the optical wavelength of interest, and $\langle(\Delta T)^2\rangle_{ave}^{1/2}$ is the rms temperature difference between the probes. For our values of $\lambda = 0.6328$ μm and r = 10 cm,

$$C_N = 1.703 \times 10^{-4}\left(\frac{P}{T^2}\right) (\Delta T)_{rms}\ cm^{-1/3} \ . \qquad (4)$$

Both the pressure and temperature were recorded continuously on a drum recorder.

The value of C_N determined from scintillation measurements is calculated using the expression[8]

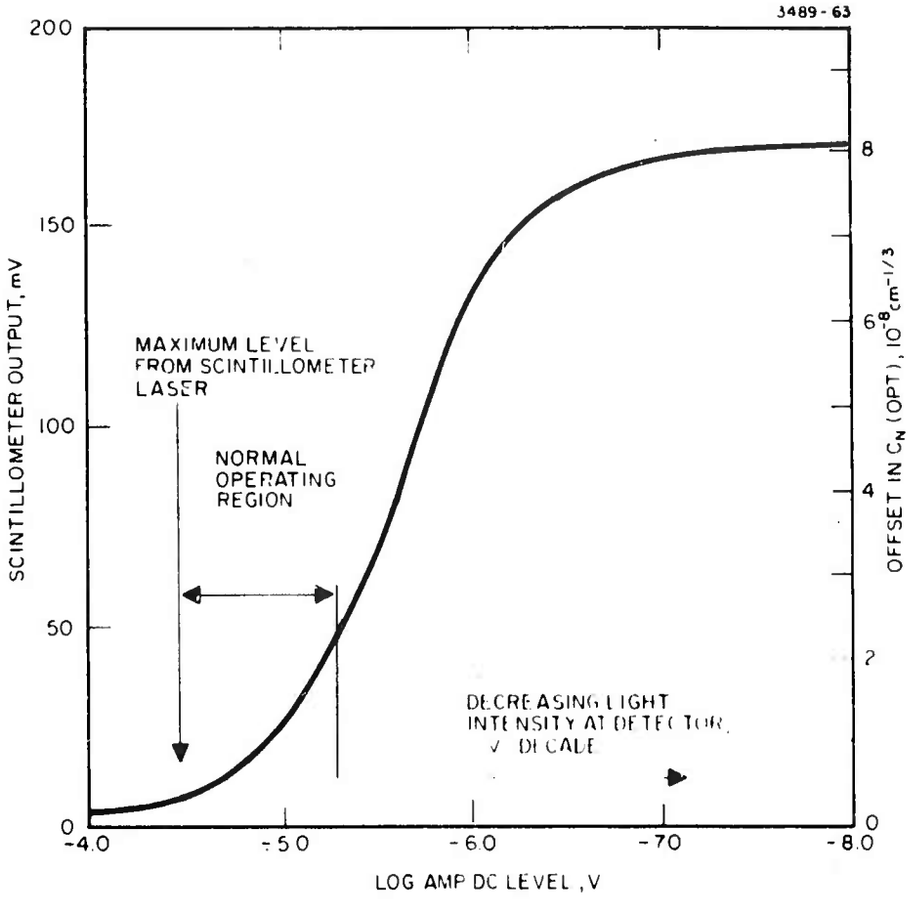

Fig. 16. Effect on measured value of C_N^2 from noise pickup by the scintillometer logarithmic amplifier (logamp).

$$C_N^2 = \frac{C_\ell(0)\left[\frac{C_\ell^s(0)}{C_\ell(0)}\right]}{0.124\, k^{7/6} R^{11/6}} \tag{5}$$

where R is the range from source to receiver and $k = 2\pi/\lambda$. The quantity $C_\ell^s(0)/C_\ell(0)$ is a correction factor for finite apertures calculated by Fried and Seidman.[13]

The quantity $C_\ell(0)$ is known as the log-amplitude variance and is defined as

$$C_\ell(0) = \left\langle \left[\ln(E) - \langle \ln(E) \rangle\right]^2 \right\rangle \tag{6}$$

where E is the time-varying received light amplitude (square root of irradiance, $E = I^{1/2}$) and the brackets, $\langle\ \rangle$, denote a time average. Assuming a log-normal distribution of irradiance, eq. (6) can be written as

$$C_\ell(0) = 1/4 \left\langle \left[\ln I - \langle \ln I \rangle\right]^2 \right\rangle \ . \tag{7}$$

When the circuit shown in Fig. 17 is used, the output of the true rms unit is

$$V_{rms} = \frac{2}{2.303} \left[\left\langle \left[\ln I - \langle \ln I \rangle\right]^2 \right\rangle\right]^{1/2} \ . \tag{8}$$

For our 100 m range and 0.62 mm beam diameter at $\lambda = 0.6328$ μm, $C_\ell^s(0)/C_\ell(0) = 0.95$, so that combining eqs. (5), (7), and (8) gives

$$C_N^2 = 1.97 \times 10^{-13}\, V_{rms}^2 \ \text{cm}^{-2/3} \ . \tag{9}$$

A typical 24 hour data record of all three atmospheric instruments is shown in Fig. 18. All three instruments use a 100 s averaging time and have a 0.1 Hz low frequency cutoff. Also illustrated in Fig. 18 is the air temperature for the same period showing the strong correlation between C_N^2 and temperature. The correlation between the two T units for these data is shown in Fig. 7 and Fig. 19 illustrates the correlation between the ΔT units and the scintillometer. The correlation coefficient ρ_{xy} was defined in Section II, eq. (1). Since there is no a priori reason for choosing one ΔT

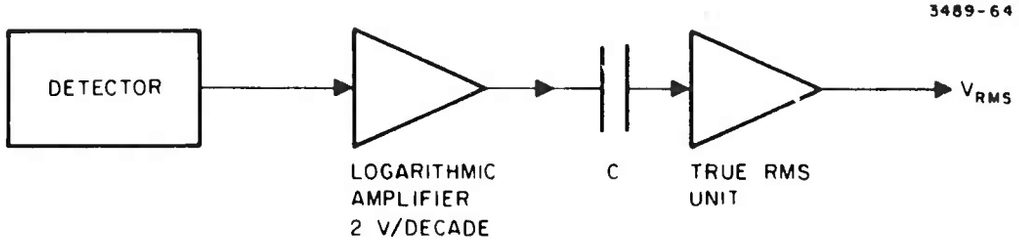

Fig. 17. Basic scintillometer elements.

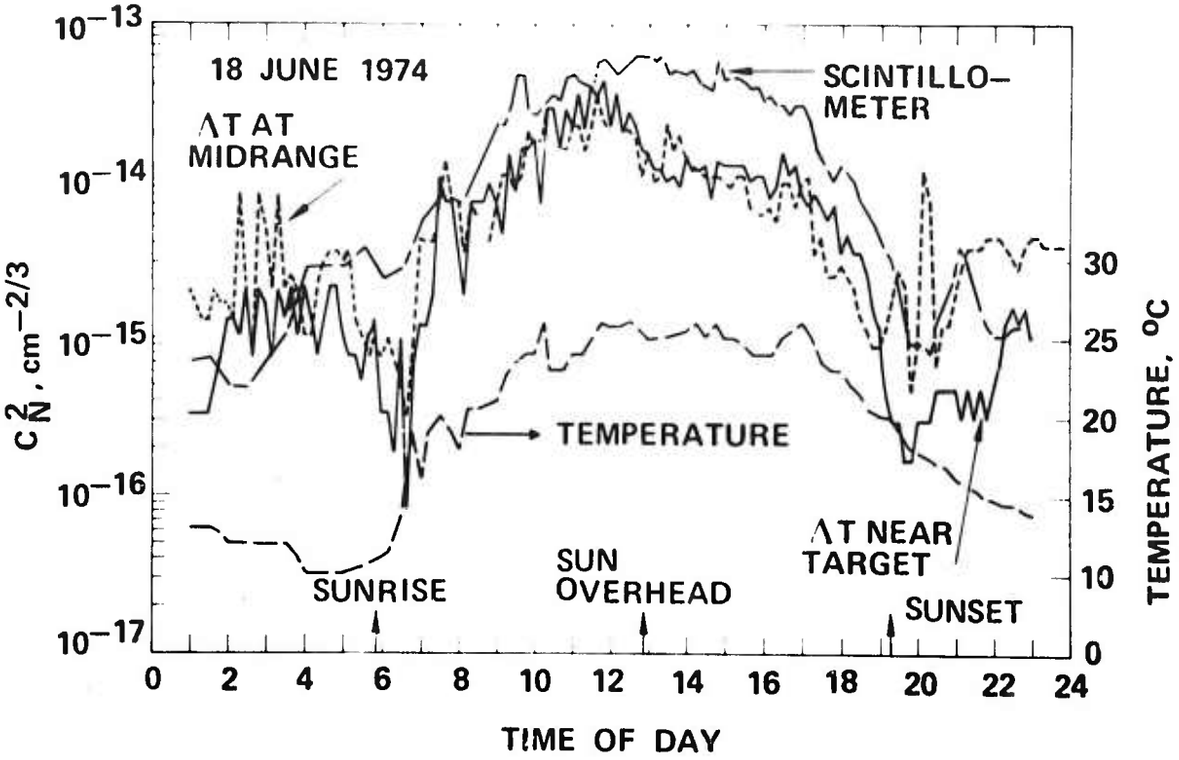

Fig. 18. Typical 24-hour data record of air temperature and 3 atmospheric instruments (C_N^2).

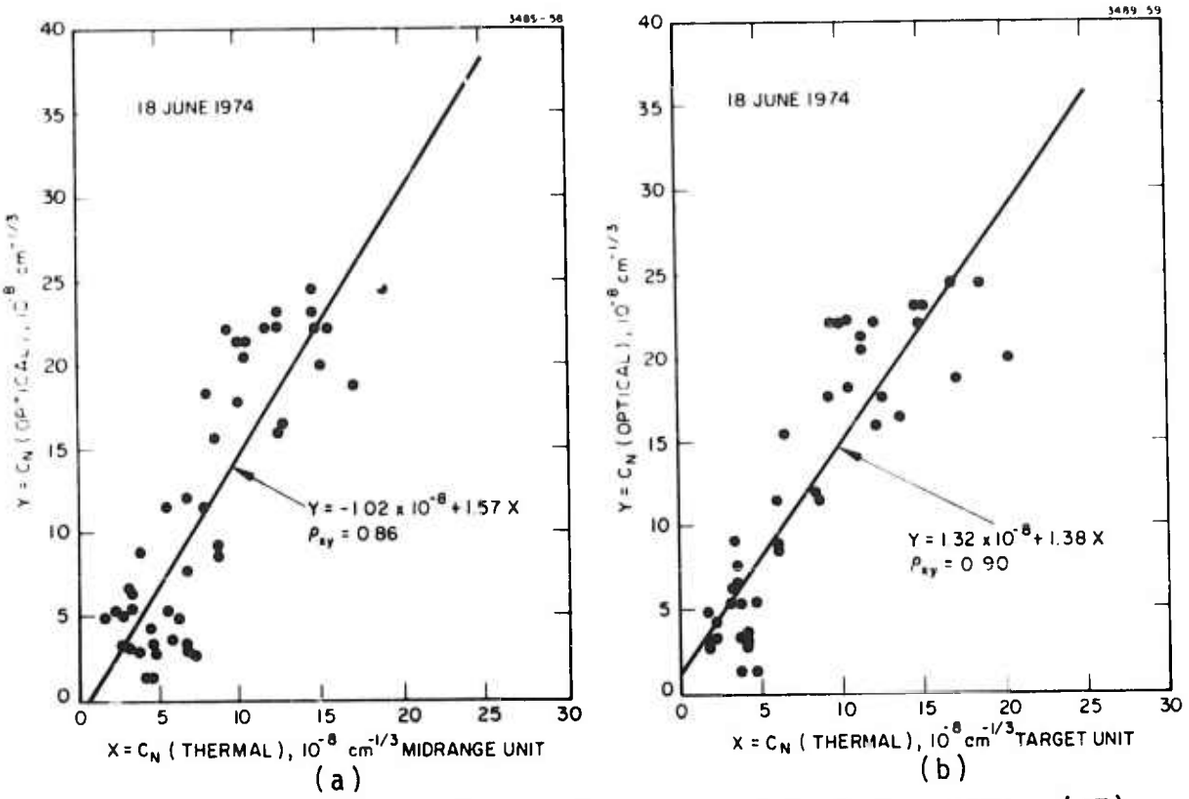

Fig. 19. Correlation between C_N measured by temperature (ΔT) and optical (scintillometer) instruments. (a) ΔT unit at midrange compared with scintillometer. (b) ΔT unit near the target (30 m from (a)) compared with scintillometer. (c) Data of (a) and (b) combined.

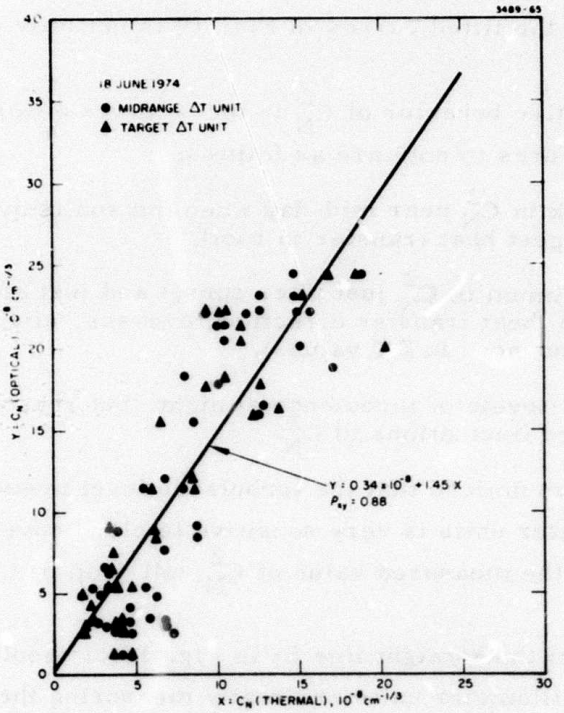

Fig. 19(c). Continued.

unit over the other, the combined data in Fig. 19(c) ar taken as the most representative. The agreement between the instruments is very good although the slope of the fitted curves in Fig. 19 is not fully understood (see discussion below).

The qualitative behavior of C_N^2 is the same as observed by others.[12,14] The particular features to note are as follows:

1. Peak in C_N^2 near mid-day when the sun is overhead (largest heat transfer to roof).

2. Minimum in C_N^2 just after sunset and just after sunrise (heat transfer direction reverses, effect most pronounced in ΔT values).

3. Low levels of turbulence at night, but reasonably large fluctuations in C_N^2.

We have also noticed that the turbulence level measured by both the ΔT and scintillometer units is very sensitive to cloud cover. If a cloud obscures the sun, the measured value of C_N^2 will drop by nearly a factor of 2 in 10 to 15 min.

The slope of the straight line fit in Fig. 19(c) should ideally be unity if the ΔT and scintillometer units are really measuring the same thing. Dowling and Livingston[14] have reported results similar to ours although their fitted line has a slope of only 1.14 compared with the 1.45 slope in Fig. 19. (This slope has been observed by us to vary from 1.02 to 1.70 depending on the day and the location of the ΔT unit.) Dowling and Livingston speculate that the higher optical C_N could be caused by several sources, individually or collectively. These sources are:

1. Integral-path versus point-measurement statistics, i.e., inherent differences in the statistics of what the scintillometer measures and what the ΔT unit senses.

2. Contributions from humidity which affect C_N(opt) but not C_N (thermal).

3. Variations of the turbulence inner scale size, ℓ_o.

To these we would add the following.

4. Path inhomogeneities (temperature, wind, speed, and wind direction).

5. Response time of the instruments causing the scintillometer and ΔT units to measure different power spectra.

Items (1) and (4) are related in that they are both deficiencies in a point measurement versus an integrated path measurement. Item (1), however, is a fundamental limitation while item (4) is a function of the weather condition and the range geometry. Humidity (item (2)) could have affected our readings since on a typical sunny day (18 June, e.g.), the humidity varied from 30% during the day to 70% at night. The nature and magnitude of the effect humidity has on C_N measurements is still unclear, however.

Variations of the turbulence inner scale could have an important effect on the scintillometer readings on our short range. The Fresnel zone size is $d_f = (\lambda R)^{1/2} = 0.7$ cm which is not much larger than the 0.1 cm receiver aperture. The short range will tend to decrease the value of C_N determined from the scintillation. Livingston[11] has shown that for a 100 m range, the inner scale must be less than 1.2 mm if the observed scintillation is to agree within 90% of Tartaski's predictions. The usual choice for ℓ_o in well developed turbulence is 1 mm which will give 92% agreement with Tartaski for a 100 m range. Since we have no measure of ℓ_o, all we can say is that the effect of larger ℓ_o will be to decrease the value of C_N as determined from scintillation measurements. Any correction for this decrease would further increase the slope of the straight line in Fig. 19.

As noted earlier, the response time of the ΔT units is only 30 to 50 Hz. The scintillometer, however, is limited only by the photodetector and log-amp frequency response and can easily measure variations at rates up to 1 to 2 kHz. Our initial supposition of the atmospheric fluctuation spectrum being less than 50 Hz appears to be contradicted by some of our measurements. Figure 20 shows the frequency spectra of both the temperature difference, ΔT, measured by one of the microthermometer units and the high-pass filtered output of the scintillometer log-amp:

$$\text{Logamp voltage (filtered)} = V_S = 2 \log_{10} \left[1 + \frac{I_{ac}}{I_{dc}}\right] \approx 0.868 \frac{I_{ac}}{I_{dc}}$$

for small I_{ac}/I_{dc}. The total output of the scintillometer detector is $I_d = I_{ac} + I_{dc}$. The scintillometer is clearly measuring turbulence frequency

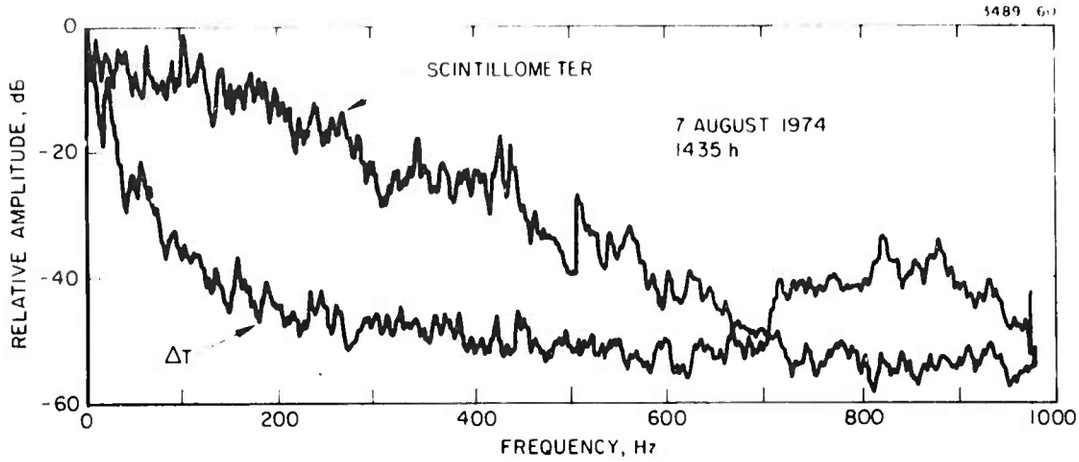

Fig. 20. Turbulence frequency spectra as seen by microthermometer (ΔT) and scintillometer. Note that 20 dB corresponds to a factor of 10 change in amplitude.

components out to much higher frequencies than the ΔT unit. In fact, the roll-off of the ΔT spectrum is very likely just the response of the probes. The larger spectrum of fluctuations present in the scintillometer could account in part for the higher optical C_N values.

It is important to consider saturation effects when using a scintillometer to measure C_N. A measure of the scintillation amplitude variance is the quantity[9]

$$\sigma_\epsilon^2 = C_N^2 \, k^{7/6} R^{11/6} \tag{10}$$

where $k = 2\pi/\lambda$ is the optical wave number and R is the range. It has been observed experimentally[15-17] that for $\sigma_\epsilon^2 \gtrsim 1$, the amplitude fluctuations do not increase with increasing path length, R, or with increasing turbulence strength; i.e., the scintillation saturates. Thus C_N^2 values found from scintillometer measurements corresponding to σ_ϵ^2 on the order of unity may be in error. For our 100 m range and 0.6328 μm scintillometer source, the condition $\sigma_\epsilon^2 \gtrsim 1$ corresponds to $C_N^2 \gtrsim 7 \times 10^{-14}$ cm$^{-2/3}$. Occasionally we have observed values of C_N^2(opt) as large as this for about one hour a day. It is interesting to note, however that we have also observed scintillometer values of C_N^2 as large as 1×10^{-13} cm$^{-2/3}$. A true limiting type of saturation apparently did not occur during our measurements, but the values of C_N^2 will be suspect above about 7×10^{-14} cm$^{-2/3}$.

3. Analysis

It will be useful when interpreting some of the COAT system performance results to know the atmospheric correlation length, ρ_c. This length is defined as the distance perpendicular to the beam path over which index fluctuations are correlated. The reciprocal of ρ_c is also a measure of the highest significant spatial frequency present in the index fluctuations. In order for the COAT system to adequately correct for the fluctuations, the turbulence must not have spatial frequencies which are comparable to the size of an element in the COAT transmitter. In other words, if the atmosphere is worse than a sixth-wave across an element, then there will be some beam degradation that even a perfect COAT system cannot remove (except by reducing the element size). On the other hand, if the atmosphere is a

sixth-wave or better across the entire transmitter aperture, the COAT system has almost nothing to correct for except residual static errors in the optics. These requirements can be stated mathematically as

$$D_T \gtrsim \rho_c > D_e \tag{11}$$

where D_T is the transmitter diameter and D_e is the element diameter.

The correlation length can be calculated from C_N^2 using the following relations[9]:

$$\langle \phi^2 \rangle_{ave} = 2.91\, C_1\, k^2 R C_N^2 \rho_c^{5/3} \tag{12}$$

where k is the optical wave number of interest, R is the propagation distance, and $\langle \phi^2 \rangle$ is the rms phase fluctuation across the aperture. The constant C_1 is equal to 1 for plane waves and to 3/8 for spherical waves.[18,19] Noting that $\langle \phi^2 \rangle_{ave} \approx 1$ for 1/6 wave fluctuations and assuming spherical wave propagation for our 100 m range and $\lambda = 0.488\ \mu$,

$$\rho_c = 0.105\left(\frac{\lambda^2}{R C_N^2}\right)^{3/5} = 2.79 \times 10^{-6}\,(C_N^2)^{-3/5}\ \text{cm} \quad . \tag{13}$$

Equation (13) is plotted in Fig. 1. Also indicated in the figure are the element and transmitter diameters used for most of our measurements. Clearly the 3 mm element diameter is sufficient to meet the requirement $\rho_c > D_e$ for all but the highest turbulence measurement conditions. For $C_N^2 \lesssim 3 \times 10^{-15}\ \text{cm}^{-2/3}$, however, the turbulence distortions will be negligible on a 1.5 cm diameter beam so minimal COAT corrections are required.

Much of the long range interest in COAT is for turbulence compensation at the infrared wavelengths 3.8 μm and 10.6 μm. It is appropriate, therefore, to ask how the range, turbulence, and aperture sizes used in our measurements scale to 3.8 μm and 10.6 μm cases.

The scaling rules for turbulence were discussed in the proposal for this contract.[20] The requirements are that the Fresnel number, a_F, of the propagating beam and the scintillation parameter, a_s, be held constant. These two parameters are defined in the following way:

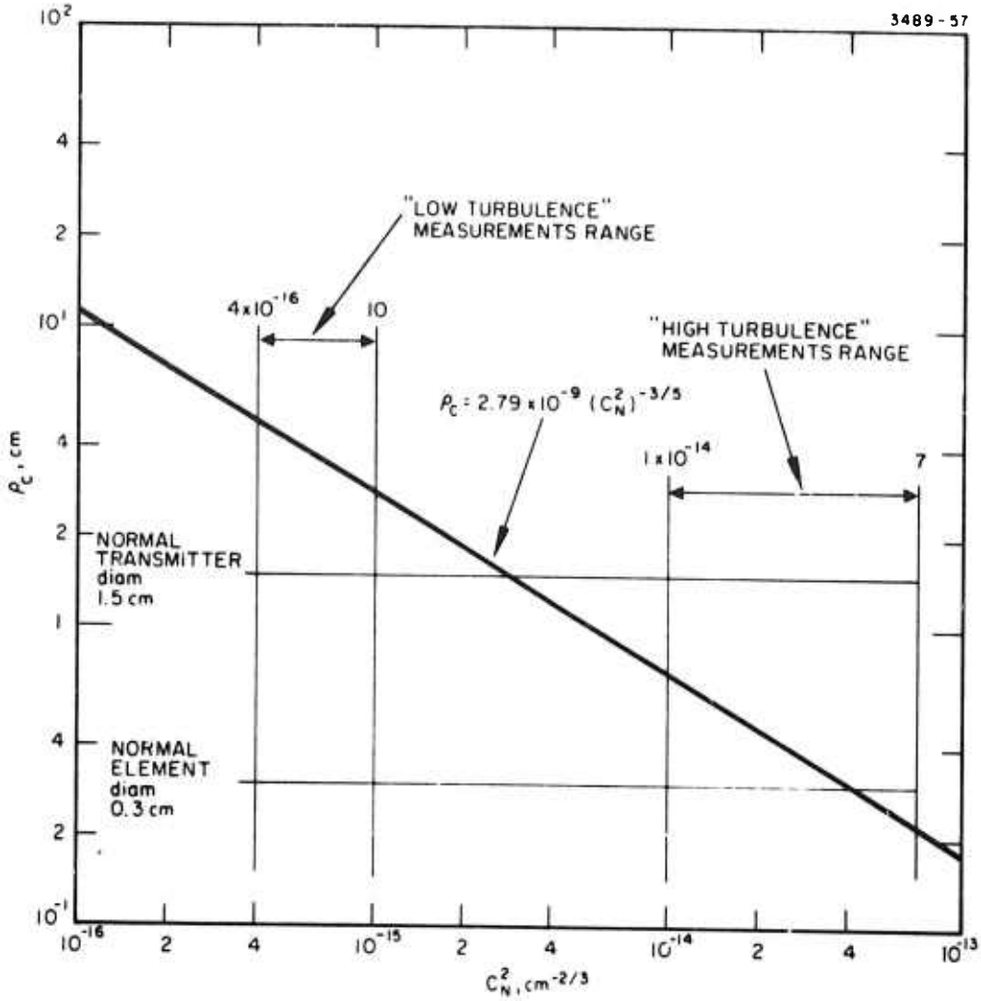

Fig. 21. Atmospheric correlation length, ρ_c, as a function of C_N^2 for conditions appropriate to the RADC/COAT range measurements (eq. (13)).

$$a_F = \frac{kD_T^2}{R} \tag{14}$$

$$a_s = C_N^2 k^{7/6} R^{11/6} \quad . \tag{15}$$

The requirement previously stated in eq. (11) can be written as $\rho_d^2 > D_e^2 = (D_T/N)^2$ where N is the number of element diameters across the transmit aperture. Using eqs. (13) through (15) to state this requirement in terms of a_F and a_s gives

$$\frac{1.1}{N^2} \sigma_F a_s^{6/5} < 1 \quad . \tag{16}$$

This result is identical to the result in Ref. 20 except for the constant. Note that for all other conditions fixed, eq. (16) sets a minimum number of elements across the transmitter diameter for effective COAT operation.

Table VI presents the scaling of our visible wavelength experiment to two different ranges at 10.6 μm and 3.8 μm. The value $C_N^2 = 4 \times 10^{-14}$ is taken as representative for the high turbulence data to be discussed later in this report. Note from Fig. 21 that for this level of turbulence, ρ_c, is nearly equal to the element size used in our experiments. The experimental system will not be able to fully compensate for the distortions present at higher levels of turbulence unless the transmitter diameter is reduced or the number of elements across the transmit aperture is increased.

B. Single Glint Measurements

Except where otherwise noted, all of the range measurements discussed in this report were made using an 18-element, 15 mm diameter transmitted beam. The near-field pattern of this beam has dark lines in it corresponding to element diffraction as shown in Fig. 22. The intensity distribution across this aperture has a gaussian taper which falls to 50% of the center peak value at the outer edge of the transmit aperture.[4]

A limited number of measurements were made using 7.5 mm diameter and 30 mm diameter beams. Before each measurement was made, the alignment of each of the 18 elements was checked to ensure that all elements were centered on a common boresight axis. This alignment was

TABLE VI

Visible Experiment Parameters Scaled to 10.6 μm and 3.8 μm

Parameter	0.488 μm Visible Experiment	Scaled 10.6 μm Infrared Experiment		Scaled 3.8 μm Infrared Experiment	
Path length, km	0.1	2	10	2	10
C_N^2, $cm^{-2/3}$	4×10^{-14}	6.0×10^{-15}(a)	3.1×10^{-16}(a)	1.8×10^{-15}(a)	1.0×10^{-16}(a)
Transmit diameter, cm	1.5	31.3	69.9	18.7	41.9
Minimum number of elements across transmit diameter	5(b)	5	5	5	5
Maximum element size, cm	0.3(b)	6.3	14.0	3.7	8.4
a_s	0.79	0.79	0.79	0.79	0.79
a_F	29	29	29	29	29

[a] Representative of turbulence levels 3 to 10 m above natural ground on a sunny afternoon.

[b] Five used in range tests; 3 mm element size.

T1460

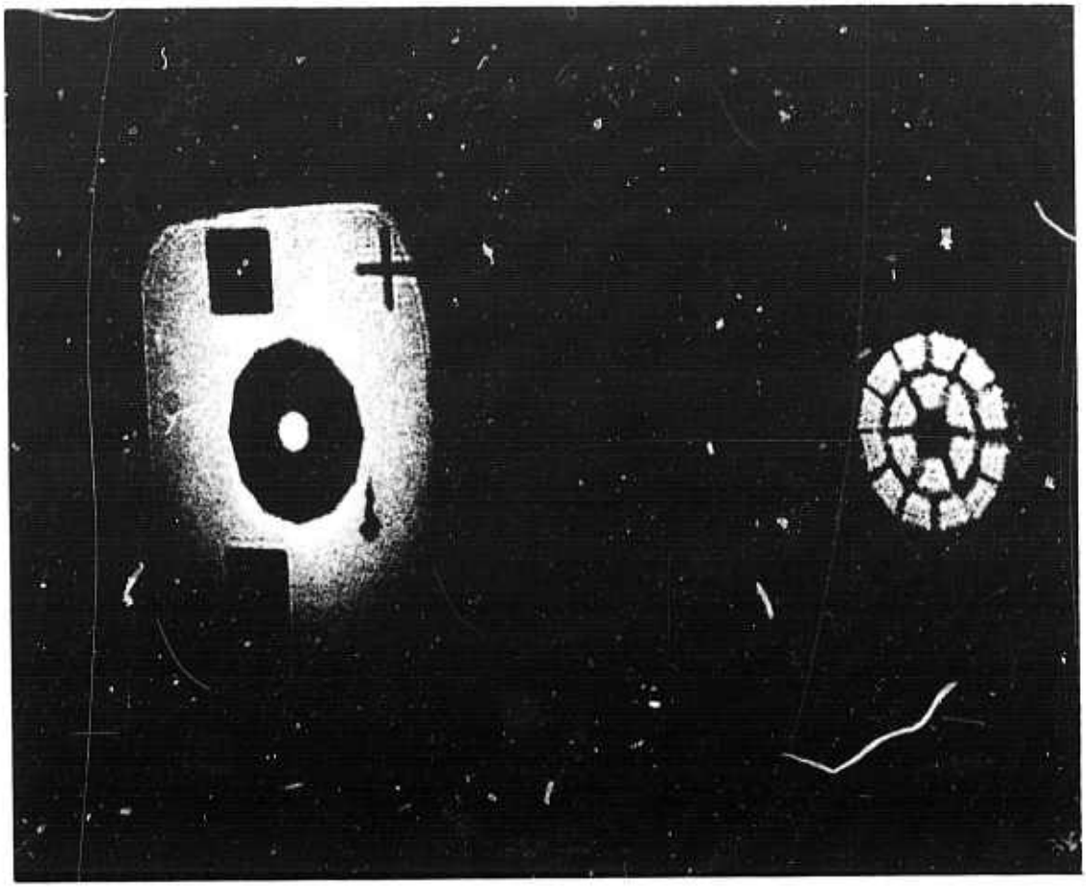

Fig. 22. Near-field phasor matrix outputs showing the 18-element array output (right) and the input beam after the array pattern and alignment marks are removed (left).

accomplished by centering each element pattern on a target glint down range. Except where otherwise noted, the servo loop gain was set approximately 3 dB below the oscillation point.

1. Convergence Performance

Several techniques were used to measure the COAT system's ability to form a diffraction-limited beam. First, a computer simulation[2-4] which models the experimental hardware has shown that the system should converge the beam on a single glint to within 95% of the diffraction limit (1.03 x diffraction-limited); the 5% loss is caused by the $\pm 20^{\circ}$ of dither.[3] Figure 23 compares the computer-generated boresight beam pattern to the experimentally observed beam pattern. The intensity contours are 1.5 dB apart in Fig. 23. A similar comparison is shown in Fig. 24 for the glint displaced from the boresight axis. Qualitatively, the experimental and theoretical patterns are the same. Quantitatively, however, they are not identical.

The simulation predicts nearly diffraction-limited performance. That is, the COAT-formed beam has a peak intensity which is nearly 18 times larger than that which would result from coherent addition of 18 randomly phased elements. Mathematically, this comparison can be expressed as

$$R = \frac{(I)_{\text{COAT-formed beam}}}{\sum_{m=1}^{18} I_m} \qquad (17)$$

where I is the light irradiance (power density) and I_m is the irradiance of the m^{th} element. For a diffraction-limited beam, $R = R_o \equiv 18$; the computer simulation predicts R = 17.1. A convenient measure of convergence is to compare R to R_o:

$$N^2 = \frac{R_o}{R} \equiv \frac{18}{R} \quad . \qquad (18)$$

The quantity N is thus a measure of the factor by which the COAT-formed beam quality exceeds the diffraction limit (N = 1.03 for the computer simulation).

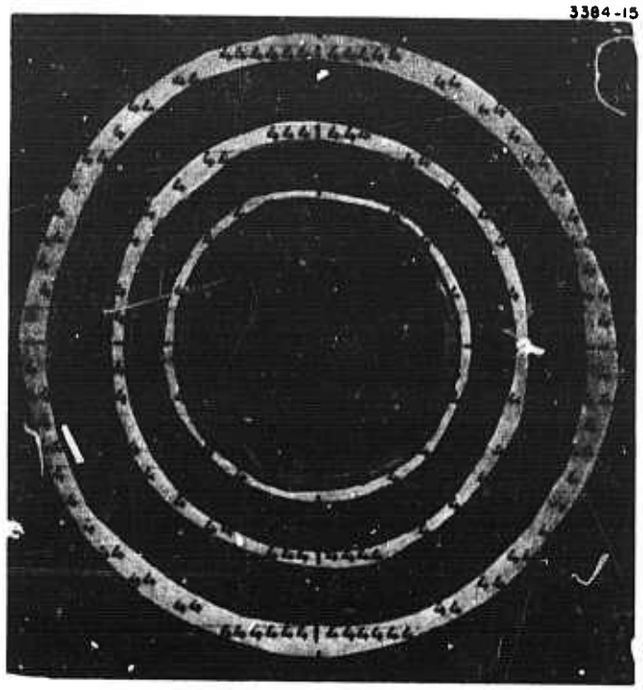

COMPUTER SIMULATION

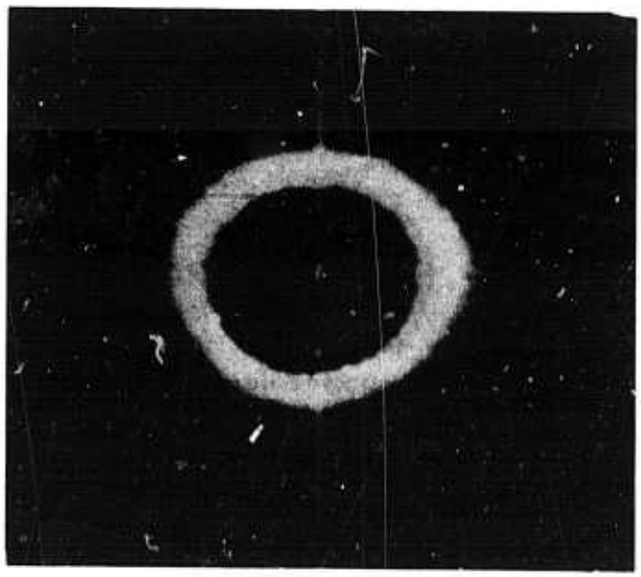

EXPERIMENT

Fig. 23.
Experimental and theoretical COAT-formed beam for a single glint on boresight.

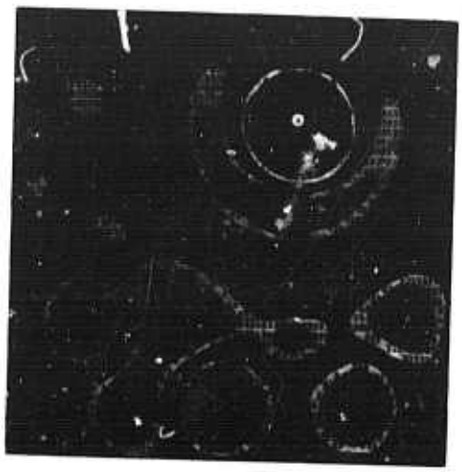

COMPUTER SIMULATION

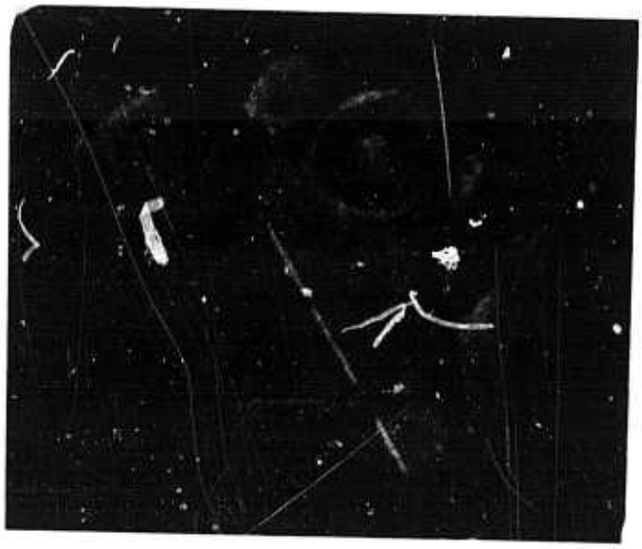

EXPERIMENT

Fig. 24. Experimental and theoretical COAT-formed beam for a single glint off the boresight axis.

The quantity N has been measured for three experimental cases: (1) laboratory convergence, no turbulence, (2) range convergence, low turbulence, (3) range convergence, high turbulence. In each case, the time-averaged power on a boresight glint (20 s averaging time) was measured for each individual element and then for the COAT-converged 18-element beam. The summary presented in Table VII shows that the system works well, but not perfectly.

A second way to measure convergence is to compare the power on the glint for "COAT on" and "COAT off" (open loop) conditions. The "COAT off" condition should represent a randomly phased array. This type of test has produced on/off ratios ranging between 11 and 15 for various levels of turbulence. If we assume "COAT off" corresponds to a randomly phased array and that 18 is the ideal ratio for a diffraction-limited beam compared with a randomly phased array, then the observations are equivalent to values of N ranging from 1.26 to 1.10. These values are consistent with those in Table VII. It is not clear why there should be any disagreement between simulation and experiment on final convergence level, but we feel that the following factors contribute to the larger experimental F values:

1. Unequal channel loop gains resulting in a net system gain below optimum.

2. Elemental beam steering caused by the bimorph phase shifters. The element patterns do not remain boresighted as the dc correction voltage level changes.

3. Elemental beam steering caused by strong turbulence so that all elements do not share a common boresight axis at all times.

Item (1) has the least effect, degrading the system performance to no more than about N = 1.05 from the theoretical simulation maximum of N = 1.03. This conclusion is based on an observed 20% variation in open loop gain between some channels. The second and third causes have quite different origins, but produce the same effect. If the combined effect of (2) and (3) is an rms steering of only 1/6 of an element null-null beamwidth, the result is a reduction in the peak intensity by 0.71 which when combined with the gain and dither reduction of 0.9 gives a total reduction of 0.64. This is equivalent to N = 1.25.

TABLE VII

RADC/COAT Convergence Performance

Date	Measurement Conditions	N(eq. 18)
3/18/74	Laboratory, no turbulence	1.14
8/6/74	Range, low turbulence, $C_N^2 = 4 \times 10^{-16}$ cm$^{-2/3}$	1.30
6/18/74	Range, high turbulence, $C_N^2 = 2 \times 10^{-14}$ cm$^{-2/3}$	1.22

T1451

We have observed element beam steering of up to one-half of an element null-null beamwidth for dc voltage changes of 125 V. Under high turbulence conditions, peak-peak voltage swings of 40 V have been seen which could produce 1/6 of an element width steering. Atmospheric element beam steering of 1/3 of an element width has also been seen for heavy turbulence ($C_N^2 \gtrsim 3 \times 10^{-14}$ cm$^{-2/3}$). Although not conclusive, these numbers give us confidence in attributing at least part of the nonideal performance shown in Table VII to the three causes listed above. More detailed investigation as well as some improvements in the hardware will be necessary before the precise cause of the discrepancy can be found and eliminated.

One other measure of convergence performance is the array beamwidth compared with the element beamwidth. Figure 25 presents this type of comparison for very low turbulence ($C_N^2(\text{opt}) \sim 2.6 \times 10^{-16}$ cm$^{-2/3}$). The observed ratio of element-to-array FWHM is 5.1 ± 0.4 compared with a theoretical maximum of 5.0. The 10% uncertainty in the ratio is caused by the difficulty in accurately determining the element beamwidth from data like that in Fig. 25. This apparently ideal beamwidth is also consistent with earlier measurements using 6 and 18 element arrays.[3,4]

Comparable performance to that shown in Fig. 25 has also been observed under very high turbulence conditions. Figure 26 shows a COAT on/COAT off picture pair of $C_N^2(\text{opt}) \approx 6.1 \times 10^{-14}$ cm$^{-2/3}$ as measured by the scintillometer. The horizontal scale is the same in Figs. 25 and 26, so Fig. 26(b) can be compared with Fig. 25(a) to give a ratio of the FWHM beamwidths of 5.4 ± 0.4. The COAT-formed beamwidth is thus equal to the diffraction-limited beamwidth within our experimental error.

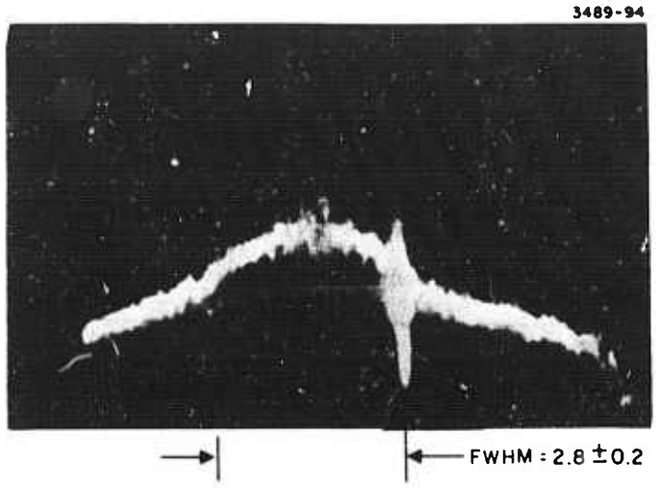

Fig. 25.
Comparison of (a) element full width at half-maximum (FWHM) to (b) the formed 18-element FWHM. Ratio is 5.1 ± 0.3.

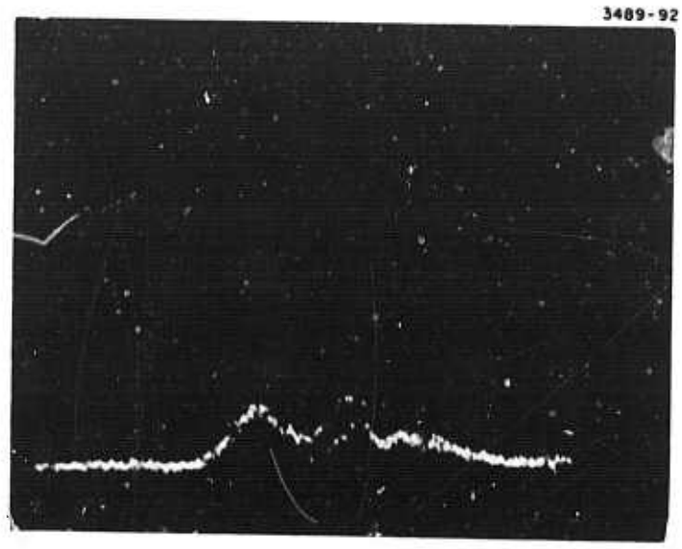

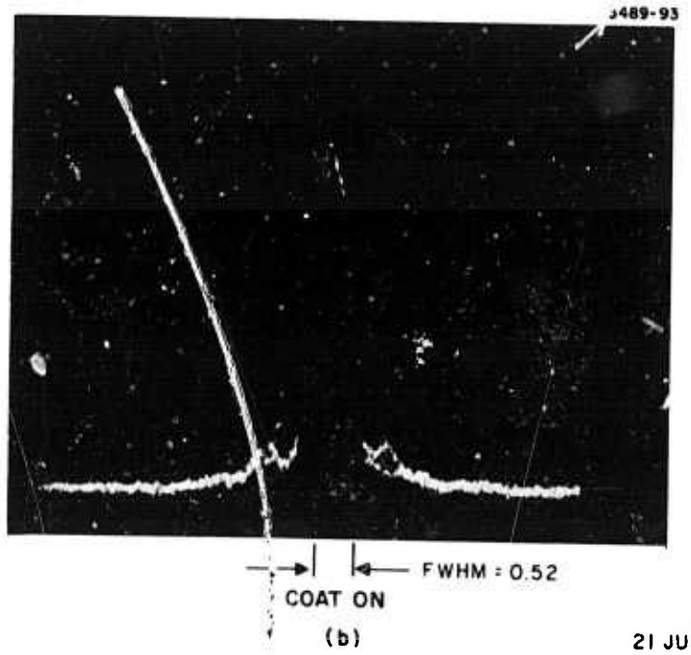

Fig. 26.
COAT convergence in high turbulence. Each figure contains three traces, 30 ms apart. (a) COAT off. (b) COAT on; array beamwidth compared to element width in Fig. 25(a) gives ratio of 5.4 ± 0.4.

The data presented above have answered the question of how well this RADC/COAT system performs compared with a theoretically ideal system. The formed beam has a diffraction-limited width, and roughly 60% of the diffraction limited peak intensity. The 60% number appears to be a hardware rather than a fundamental limitation since our computer simulations show convergence to 95% of the diffraction limit. We have not, however, addressed the question of what the beam quality would be with no COAT system but with high quality optics. Once we answer this question, then the amount of turbulence compensation effected by the COAT system can be determined. The technique for making this type of comparison using the sample-and-hold circuitry was discussed in Section II-D-2.

Figure 27 and Table VIII summarize the results of our measurements of turbulence compensation for very low (C_N^2(opt) = 1 x 10^{-16} $cm^{-2/3}$) and very high (C_N^2(opt) = 5.8 x 10^{-14} $cm^{-2/3}$) turbulence conditions using the sample-and-hold circuitry. The strong atmospheric turbulence degrades the beam by a factor of 6.7 and the COAT system effects a factor of 2.85 improvement. The remaining factor of 2.35 for which this COAT system cannot correct can be explained by two factors. First, Fig. 21 indicates that the turbulence level is so high that the coherence length is not larger than the transmitter element diameter. Thus there are distortions present which require smaller element sizes to correct. Second, there are large fluctuations (± 50% of the average glint power) which are caused by steering of the entire beam as well as by steering of the individual elements. Additional evidence of this steering will be presented later, but the fact that the peaks in Fig. 27(c) are equal to the peaks in Fig. 27(a) is one indication of steering. A COAT system which has servo channels to correct for gross beam steering should significantly reduce the glint power fluctuations while increasing the average power on the glint.

2. Convergence Time, τ_c

The previous contract report[4] quoted single glint convergence times of 3 to 5 ms and speculated on problems with loop gain as the cause of the increase in τ_c over previously reported values[3] of 1 to 2 ms. The resolution of the problem is shown in Fig. 28 where the glint detector output voltage and the photomultiplier (PMT) output voltage are shown for a single

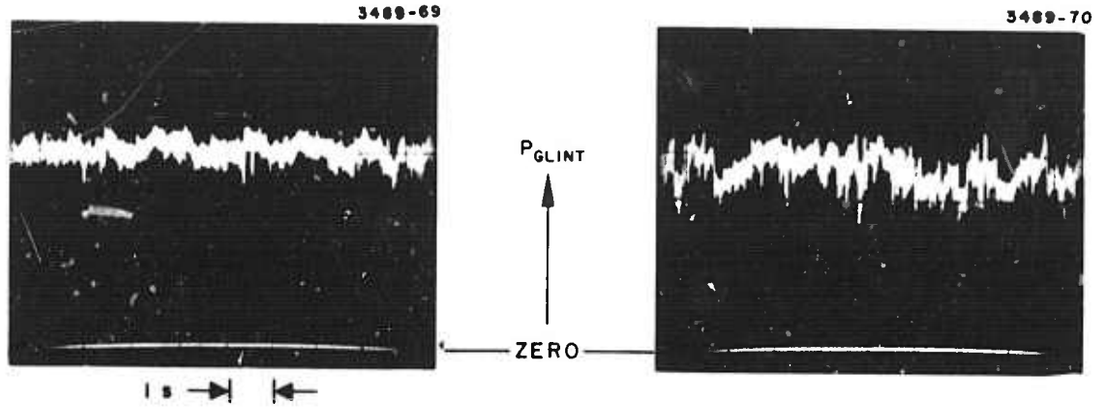

COAT ON
Pg = 3.15

NO COAT CORRECTION
Pg = 2.85

(a) 30 JULY 1974 (b)

0030 h

$C_N^2(OPT) = 1.0 \times 10^{-16} cm^{-2/3}$

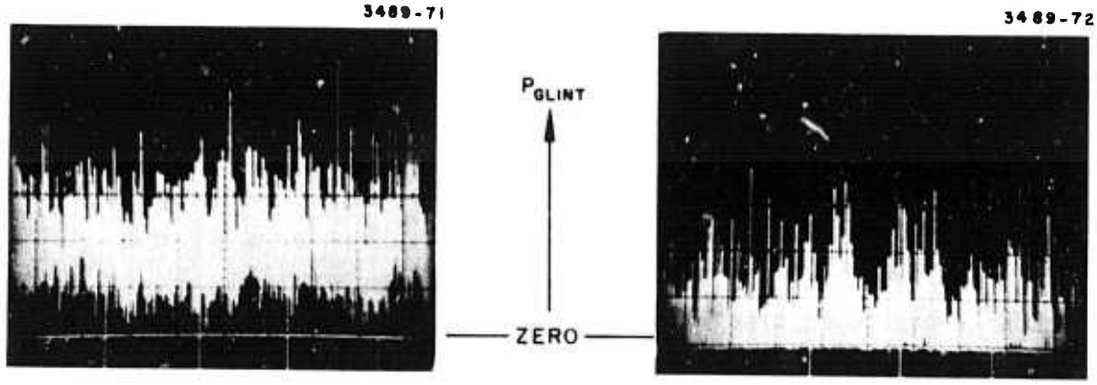

COAT ON
Pg = 1.34

NO COAT CORRECTION
Pg = 0.47

(c) 30 JULY 1974 (d)

1400 h

$C_N^2(OPT) = 5.9 \times 10^{-14} cm^{-2/3}$

Fig. 27. Power on glint with and without COAT correction. The large positive and negative periodic spikes are microwave radar interference. The total transmitted power is the same for all four cases.

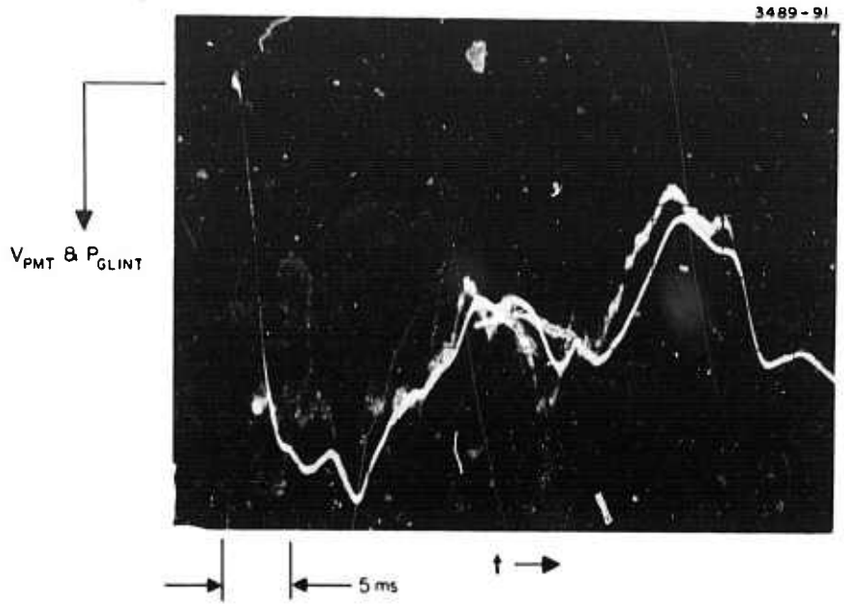

Fig. 28.
COAT convergence time showing PMT voltage and power on the downrange glint. Note the slower response of the glint signal.

loop closing. The scope traces begin when the servo loop is closed. The PMT signal rises to its maximum value in 1.5 to 2.0 ms while the glint signal takes 3.5 to 5.0 ms to reach its maximum. The fluctuations in the glint power after convergence are caused by heavy turbulence and are discussed further in Section II-B-4.

The glint detector/line driver combination used in our measurements does not have sufficient frequency response to follow the rapid increase in glint power during convergence after the servo loop is closed. Recent measurements have shown that the glint detector/amplifier combination has a simple RC rolloff with a -3 dB voltage corner frequency of 160 Hz. The effect of this low frequency response on measured values of τ_c is illustrated in Fig. 29. The simulation-produced convergence runs (servo simulation only) are for optimum loop gain and for two different power-on-glint detector time constants: 100 kHz and 160 Hz. The effect of the 160 Hz corner is obvious, increasing the apparent value of τ_c to 4.8 ms from the actual value of 2.0 ms. The agreement between the 160 Hz theoretical curve and the measured experimental convergence time (low turbulence) is quite good, qualitatively and quantitatively. Figure 30 shows 5 consecutive loop closings under conditions identical to Fig. 29(b) to illustrate the 20 to 40% fluctuations in the observed values of τ_c from run to run.

TABLE VIII

COAT Turbulence Compensation Performance

Experimental Condition	$\overline{P}_g$ (Arbitrary Units)	$[(\overline{P}_g)$, Low Turbulence$]/\overline{P}_g$
Low turbulence, COAT on	3.15	1.00
Low turbulence, no COAT correction	2.85	1.10
High turbulence, COAT on	1.34	2.35 } Ratio = 2.85
High turbulence, no COAT correction	0.47	6.70 } = COAT correction factor

T1462

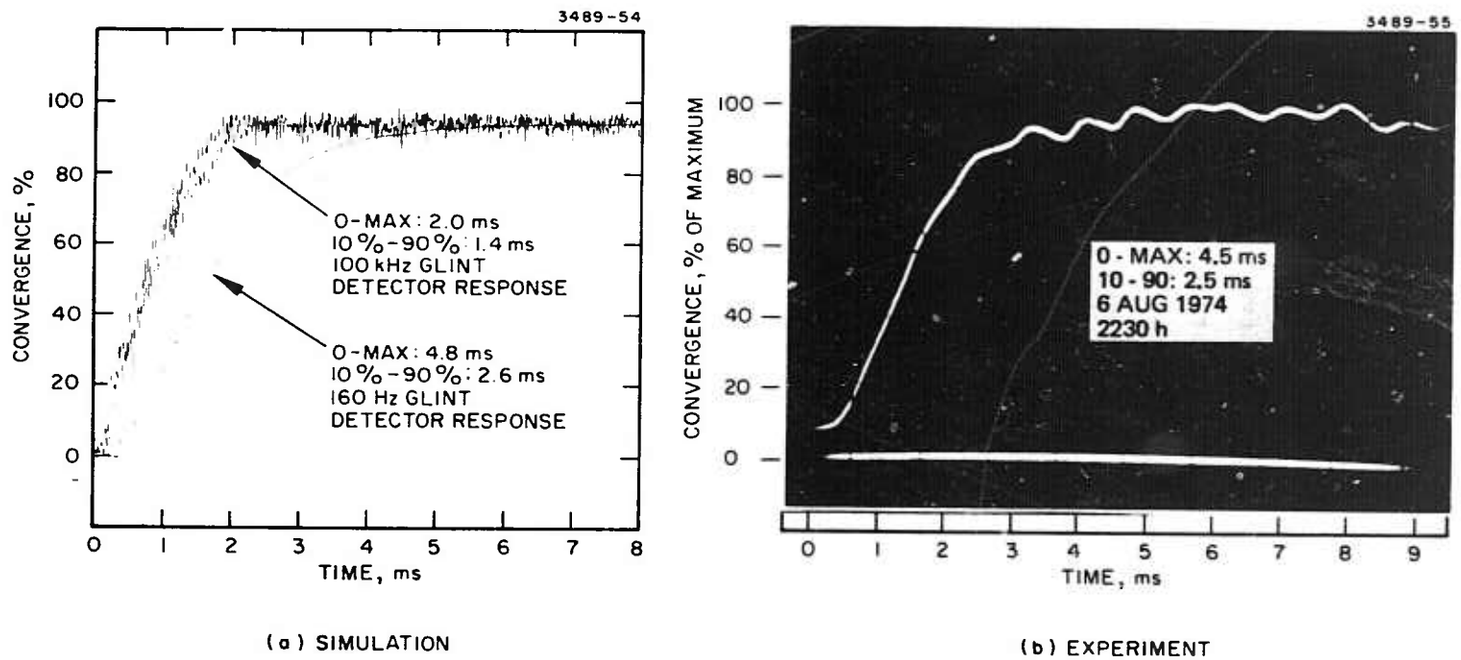

Fig. 29. COAT system convergence runs. (a) Simulation results for two different detector frequency response values. (b) Experimental result using a detector with a 160 Hz response.

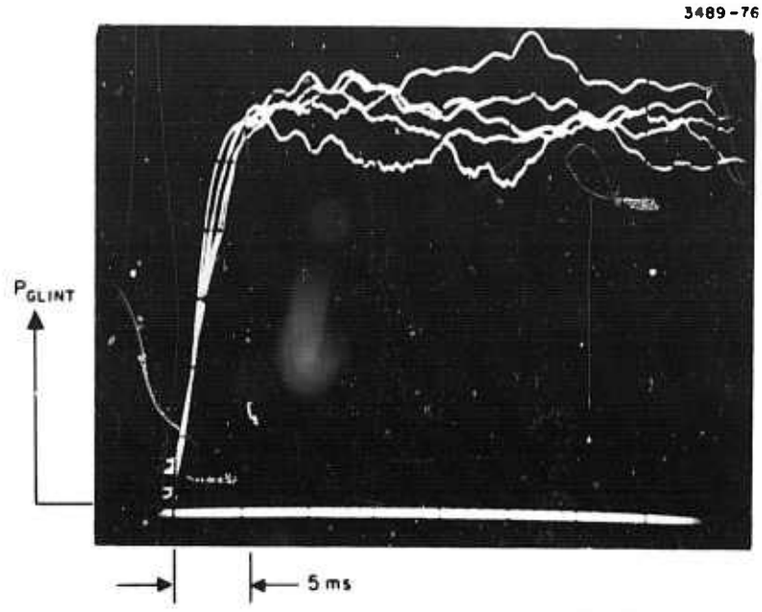

Fig. 30.
Five consecutive loop closings showing the variations in convergence time τ_c. The actual τ_c is less than that indicated (see Figs. 29 and 31).

Unfortunately, all of our convergence time measurements were made with the slow glint detectors. Results similar to Fig. 29, however, can be used to convert the observed values of τ_c to the actual system performance. The solid points in Fig. 31 were found using the COAT servo simulation and a 160 Hz corner on the glint power detector response; the curves are smooth lines drawn through these points. Curves for two different definitions of rise time are shown.

Numerous results similar to those shown in Figs. 29 and 30 indicate that with near optimum gain settings, the system has a convergence plus setting time (initial level to final level) of 1.5 to 3.0 ms for all levels of turbulence. Our data indicate that the strength of turbulence has no significant effect on convergence time. The results also provide a strong verification of the accuracy of the computer simulation and verify the servo design produced by using this simulation.

Two interesting features of the fast detector convergence process shown in Fig. 29 are the sharp rise and nearly constant convergence rate once convergence begins, and the almost-square corner when the maximum convergence level is reached. There is no overshoot and little slowing of the convergence process as the maximum level is approached. This is not too surprising a result since the effective incremental loop gain increases as the convergence process proceeds and is maximum at maximum convergence.

3. Convergence Stability

The computer simulation run shown in Fig. 29 shows excellent stability of the glint power after convergence. This stability was one of the design criteria used in arriving at the final servo parameters. The small residual fluctuations in power are caused by the dithers. The simulation does not have any atmospheric effects, however, and if these effects include beam and element steering, the fluctuations can be increased significantly.

In a previous section we have attributed part of the COAT system's departure from diffraction-limited performance to beam steering effects. Figure 27 shows the great difference in fluctuations observed under high and low turbulence conditions. In Fig. 27(a), the fluctuations are ±10% of the average value or only 20% peak-to-peak. In Fig. 27(c), however, the fluctuations are comparable to the average level: +100%, -75% of the average

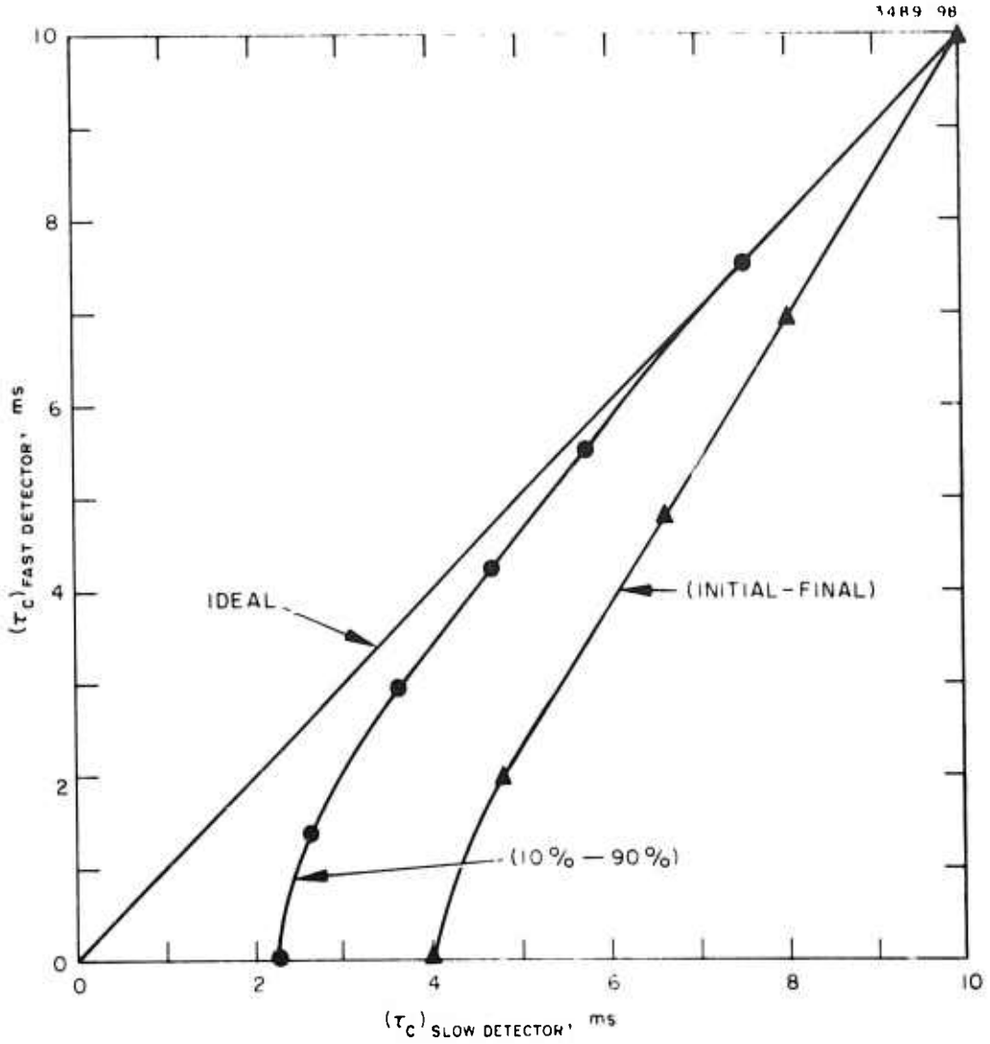

Fig. 31. Relation of actual to measured values for τ_c caused by slow glint detector response (160 Hz -3 dB voltage corner frequency). Two different definitions for τ_c are shown.

value or peak-peak fluctuations 1.75 times the average value. We attribute these fluctuations to atmospheric disturbances which cannot be compensated for by only a stepwise phase correction across the transmitter aperture.

Figure 32 shows another example of the fluctuations observed on a faster time scale under high and low turbulence conditions. The surprising feature in these data is the rapidity of the fluctuations. The factor of 2 fluctuations occur in as little as 10 ms which is comparable to the system convergence time of 2 to 3 ms. If the power fluctuations are indeed caused by overall beam steering, they could be reduced by using xy microslewing mirrors controlled by COAT servo loops. The response time of these loops would need to be on the order of 100 Hz for complete correction, but substantial improvement could be obtained with only 20 to 40 Hz response. This conclusion is consistent with the results of Chase[21] who considered the improvement for a heterodyne system when tracking is employed.

As Chase points out, a first order estimate of the tracking bandwidth can be found by assuming the steering is caused by a wind blowing large scale eddies across the beam. Since overall beam steering will be produced by eddies larger than the transmitter diameter, the required tracking bandwidth in Hertz is

$$\Delta f \gtrsim \frac{V}{\pi D_T} \tag{19}$$

where V is the transverse wind velocity and D_T is the transmitter diameter. There is a maximum useful value of Δf, however, given by

$$(\Delta f)_{max} = \left(\frac{V}{\pi \ell_o}\right) \tag{20}$$

where ℓ_o is the turbulence inner scale. Bandwidths larger than $(\Delta f)_{max}$ will have little effect since there are almost no turbulence-induced index fluctuations with scales smaller than ℓ_o. A typical value for the wind during our tests is 2 m/s. For this wind with a 1.5 cm diameter transmitter, eq. (19) gives $\Delta f \gtrsim$ 40 Hz. This value is in reasonable agreement with our conclusions based on the results in Fig. 32.

It is apparent from eq. (19) that increasing D_T will reduce the bandwidth requirements on the tracking system. If a slewing beam is used,

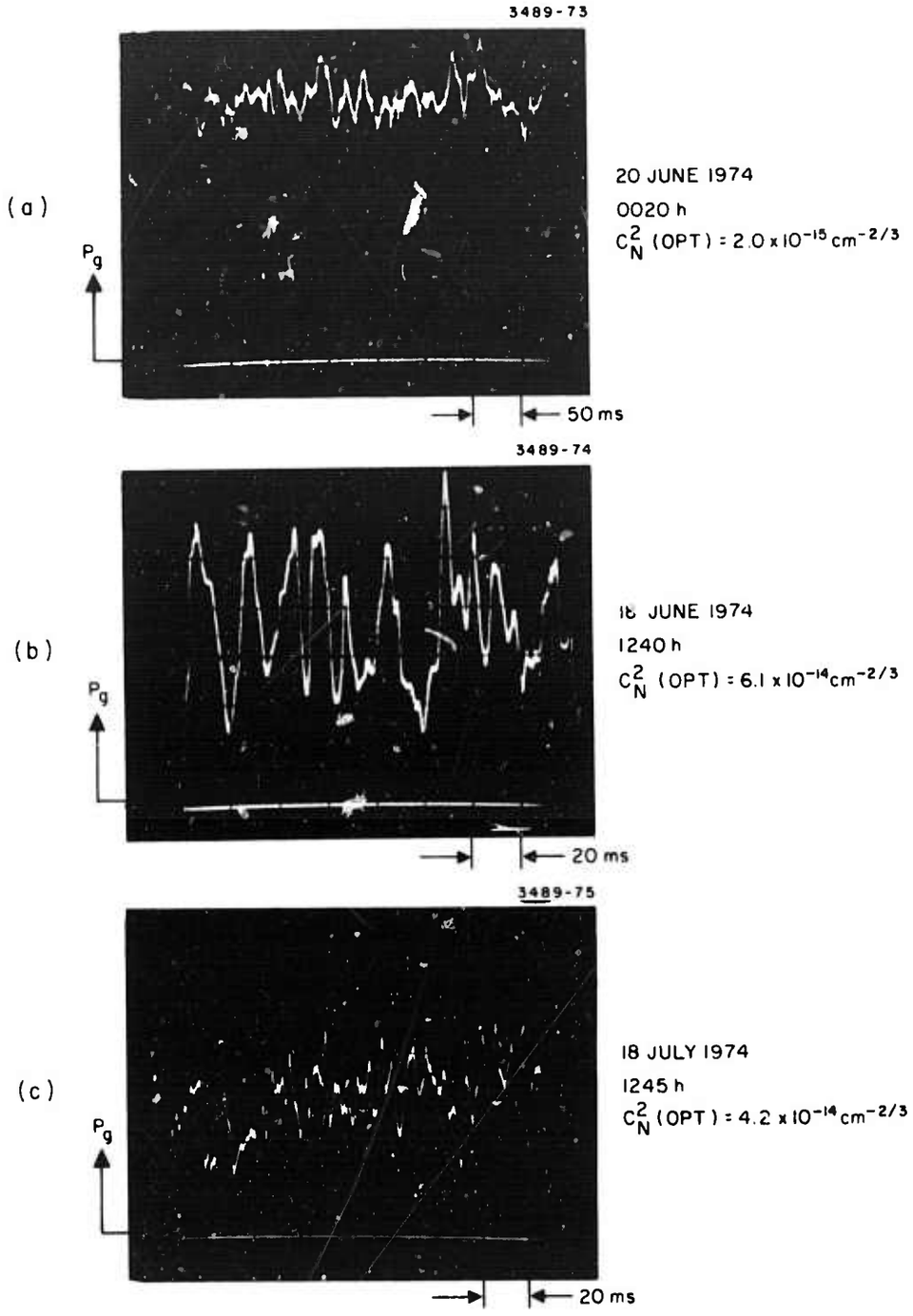

Fig. 32. Fluctuations in the power on a single boresight glint for various turbulence conditions.

however, the effective value of V can be much larger than the wind speed. The net result of all these considerations is that a tracking system to compensate for turbulence beam steering will need a bandwidth on the order of 50 Hz if it is to be effective under all possible conditions.

Two tests were run to try to measure the extent of beam steering. First, the transmit aperture size was halved from 15 to 7.5 mm using a reducing telescope. This change should reduce the effects of atmospheric phase distortions while leaving the steering fluctuations essentially unchanged. The results of this test are illustrated in Fig. 33. For the smaller transmitter, the reduction in the average glint power, $\bar{P}_g$, is less for stronger turbulence. The ratio of the peak-to-peak fluctuations to the average power are comparable for both apertures with slightly smaller fluctuations for the smaller aperture (notice the different vertical scales in the figures). Video observations of the beam intensity confirm this conclusion: for "no COAT correction" with the smaller aperture, the atmosphere affects the beam formation much less, but the steering of the beam is not significantly reduced.

The second test was to look at the steering of two individual element patterns. Two horizontal elements (numbers 7 and 13) on opposite sides of the outer ring of elements were selected and steered apart vertically so they were separated by about 1.5 times the element null-null beamwidth. This arrangement allowed sampling of both horizontal and vertical steering effects. A glint detector was centered on each element pattern to record the power fluctuations and the patterns were observed with the target TV camera. Figure 34 schematically illustrates the test. If the elements move together (correlated motion), then the fluctuations in the difference of the irradiance seen by each detector should be less than the sum of the fluctuations on each detector and the frequency spectrum of the different fluctuations should have a lower amplitude than the spectrum of the individual detector outputs. For completely uncorrelated element steering, the spectrum of the difference should be the same as that of the individual detector outputs and the peak-peak difference fluctuations will equal the sum of the peak-peak fluctuations out of each detector.

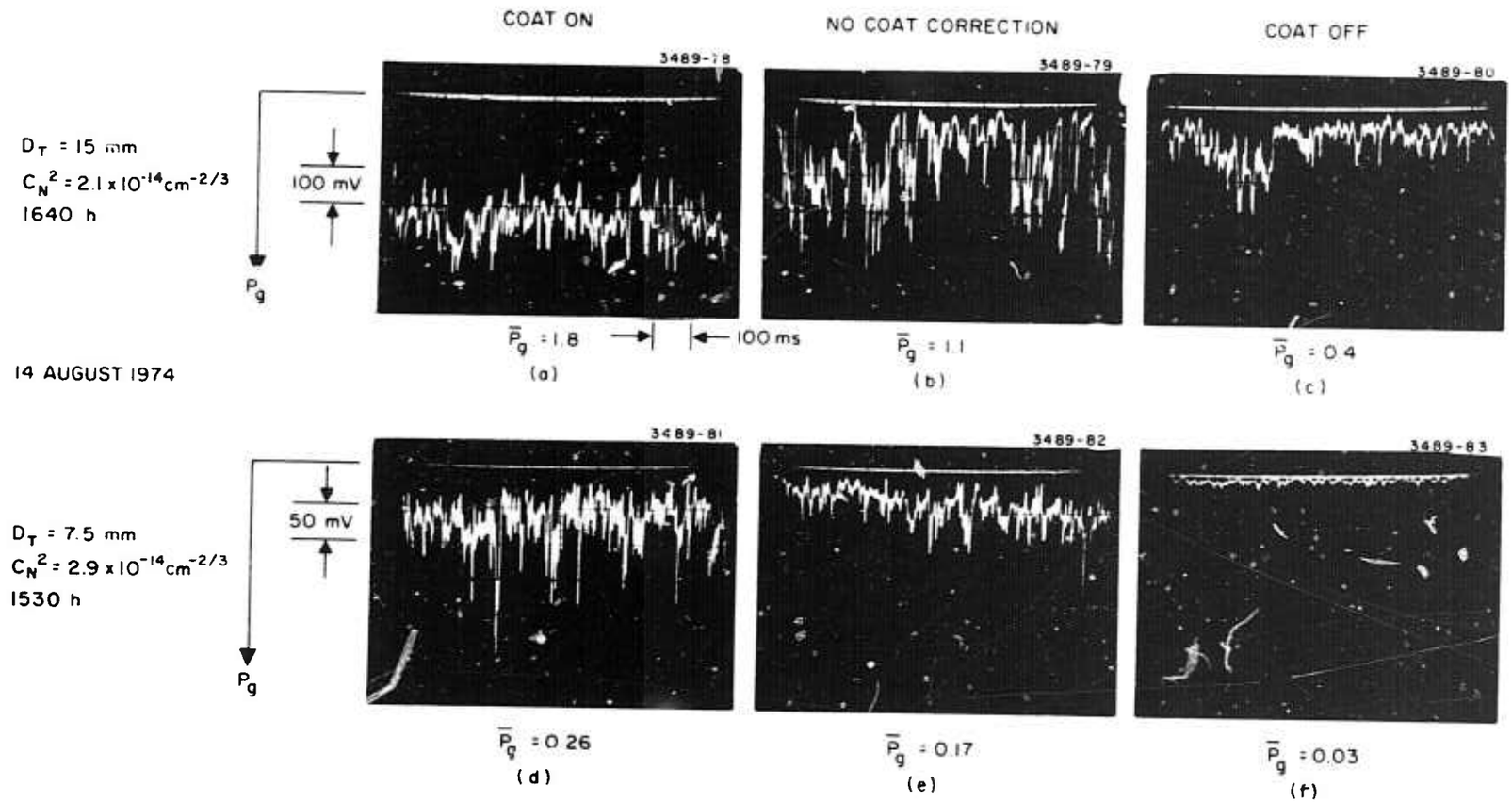

Fig. 33. Fluctuations in glint power for two different transmitter diameters, D_T. The total transmitted power is the same for all figures. (a), (b), and (c) D_T = 15 mm (d), (e), and (f) D_T = 7.5 mm. $\bar{P}_g$ is the time-averaged power on the glint.

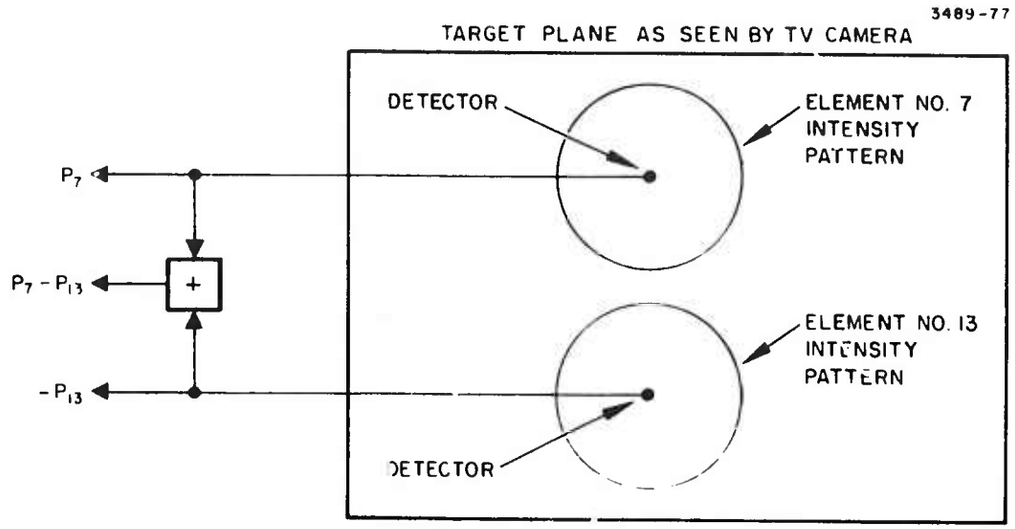

Fig. 34. Schematic of test setup using two element patterms to measure beam steering effects.

The results of this test are shown in Figs. 35 and 36 for low and high turbulence conditions. Illustrated in Fig. 35 is the power on each glint and the difference between these powers. Again, note the different vertical scales in the high and low turbulence cases. The frequency spectrum of one detector output, P_7, and the difference, $(P_7 - P_{13})$, is shown in Fig. 36.

A naive interpretation of the data in Fig. 36 will lead to a conclusion that the element steering is completely uncorrelated for both high and low turbulence since the difference and single element spectra are nearly identical. This would be surprising since only large scale turbulence eddies are expected at low turbulence levels. A straightforward analysis shows, however, that the two detectors must be centered on identical portions of the element patterns if the difference spectrum is to differ from the individual element spectrum. This alignment is very difficult to accomplish and maintain so no firm conclusions can be based on comparing the nature of the element and element-difference spectra. Notice in Fig. 36(a), however, that below 50 Hz the element spectrum is somewhat larger than the difference spectrum as expected. One thing that can be concluded from the data in Fig. 36 is that the steering fluctuations are larger by a factor of 2 to 4 and contain much higher frequencies in high turbulence.

We have also recorded the element pattern motions on video tape. Although the video data is very qualitative, we conclude that for low turbulence the steering of the two elements is almost fully correlated but is only partially correlated in high turbulence. That is, in high turbulence both correlated and uncorrelated motion can be seen. In addition, the element patterns do not appear to break up into "patches" or "blobs" while they are being steered. These observations give us confidence that we have done the wavelength scaling (10.6 μm to visible) properly. That is, for high turbulence there is very little correlation between elements across the transmit aperture, but only small phase fluctuations across each element. This conclusion also agrees well with the atmospheric correlation lengths plotted in Fig. 21.

The data presented above lead us to conclude that for turbulence compensation it is desirable to include xy-pointing control as part of the COAT servo system. It appears that in high turbulence up to a factor of 2

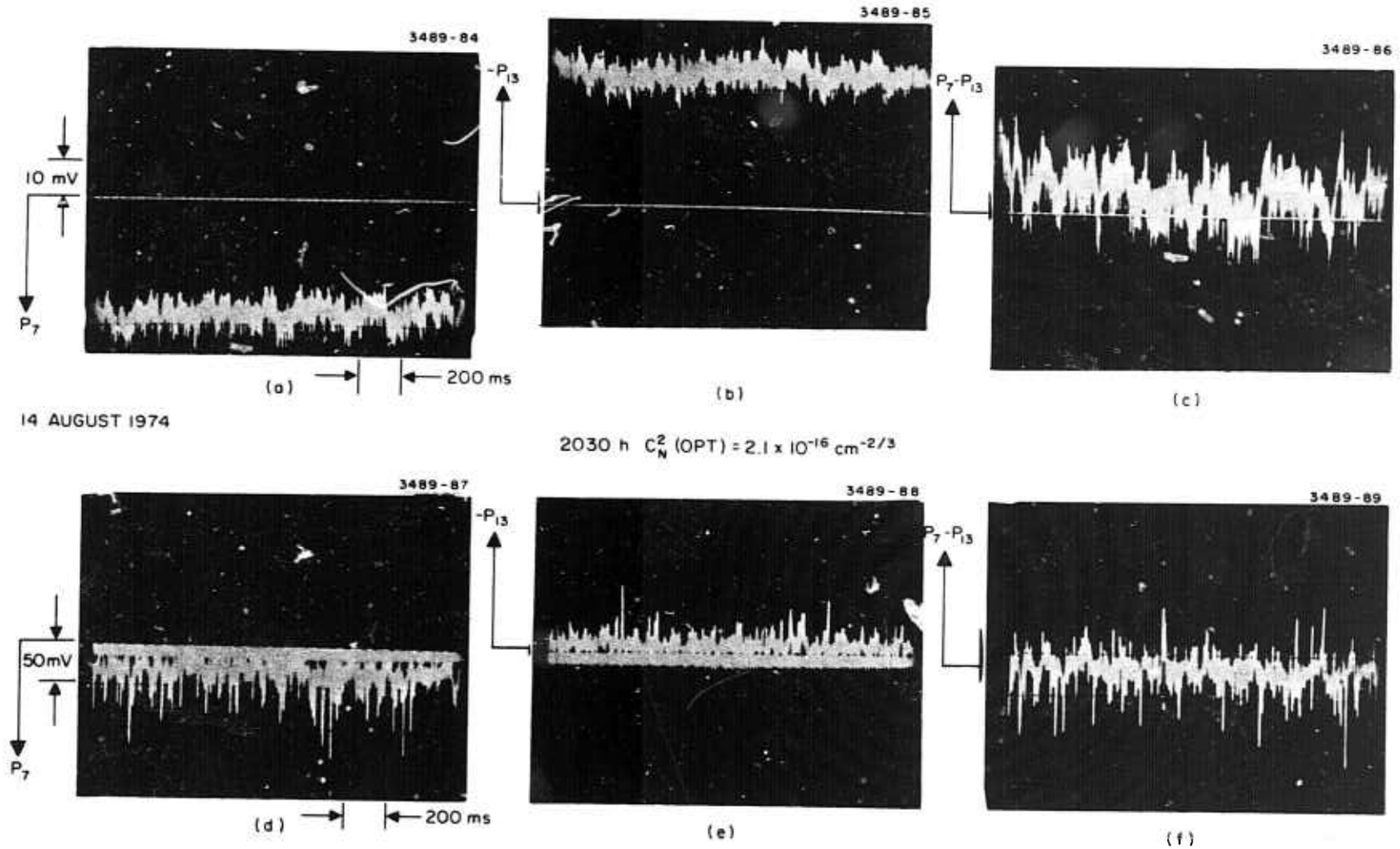

Fig. 35. Irradiance at the target seen by detectors at the center of two spatially separated elements, 7 and 13 of the transmit aperture. (a) P_7. (b) $-P_{13}$. (c) P_7-P_{13}. (a), (b), and (c) are for low turbulence. (d), (e), and (f) are the corresponding pictures for high turbulence. A factor of 10 change in irradiance is 20 dB.

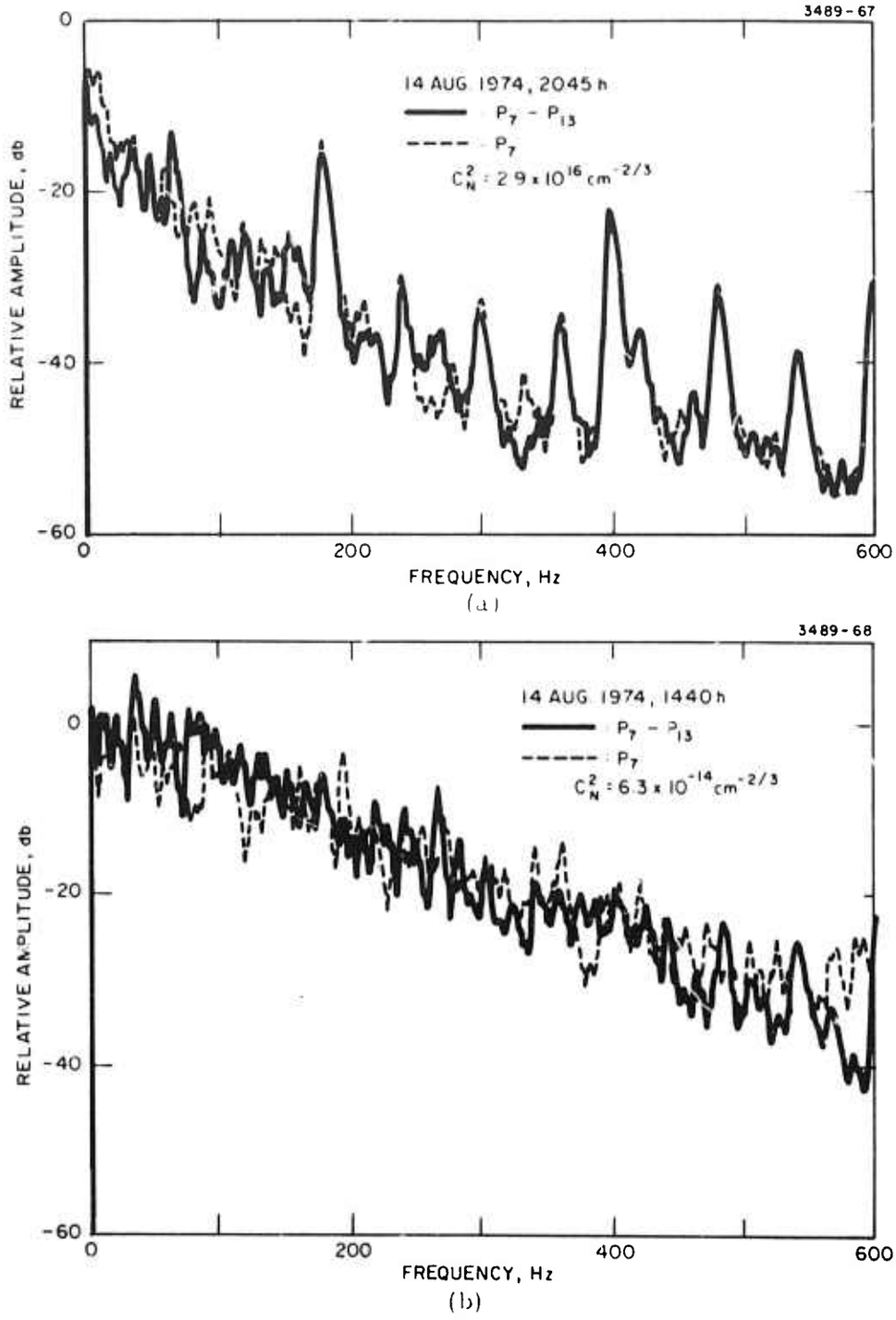

Fig. 36. Frequency spectra of irradiance fluctuations shown in Fig. 35. Spectrum for one element, P_7, and for difference in elements, P_7-P_{13} is shown. (a) Low turbulence. (b) High turbulence.

improvement in power density over pure phase control can be obtained by adding servo-controlled pointing. It is also true that xy-pointing will increase the power densi'y on the strongest glint, whether stationary or moving, by steering the boresight axis onto the glint. This technique has previously been referred to as "autoblazing."[20]

4. Frequency Spectra

In any evaluation of a COAT system's performance, it is important to know the power spectra of such quantities as the applied error signals, the received signal returns from the target, and the power on the glint. All of these parameters have been recorded simultaneously under both high and low turbulence conditions using a multichannel recorder. Table IX lists the parameters recorded during each data run. A typical run lasted 10 min and a total of 11 data runs were made under various conditions. An FM recorder was used so that frequencies near zero could be recorded, but only the glint power and photomultiplier signal were dc coupled. The other signals had large dc offsets and so were coupled through high-pass filters and sometimes through attenuators to prevent overloading the FM recorder input.

One of the first questions asked about COAT systems is "what are the magnitudes of the corrections applied?" Figure 37 shows the correction signal applied to one bimorph phase shifter under very high turbulence conditions. The calibration for all our data is 11.9° of phase shift per volt; that is, a correction voltage of one volt corresponds to an optical phase shift of 11.9°. The peak-to-peak voltage change in Fig. 37 is roughly 40 V corresponding to 476° or 1.32 wavelengths of phase shift at 0.488 μm. This is a large phase shift, but it is typical of the variations observed in heavy turbulence. Note that the largest phase change takes about 100 ms and that the measured correction signal has been dc coupled to the scope. When using ac coupling, such large changes are not observed. Faster phase variations on the order of 10 to 50 ms are a factor of 2 to 10 lower in amplitude. This fact is further illustrated in the spectra presented below.

a. Phase Error Signals — The time-correlated signals listed in items A through D of Table IX are shown in Fig. 38 for low turbulence and in Fig. 39 for high turbulence. The complete 18-element system

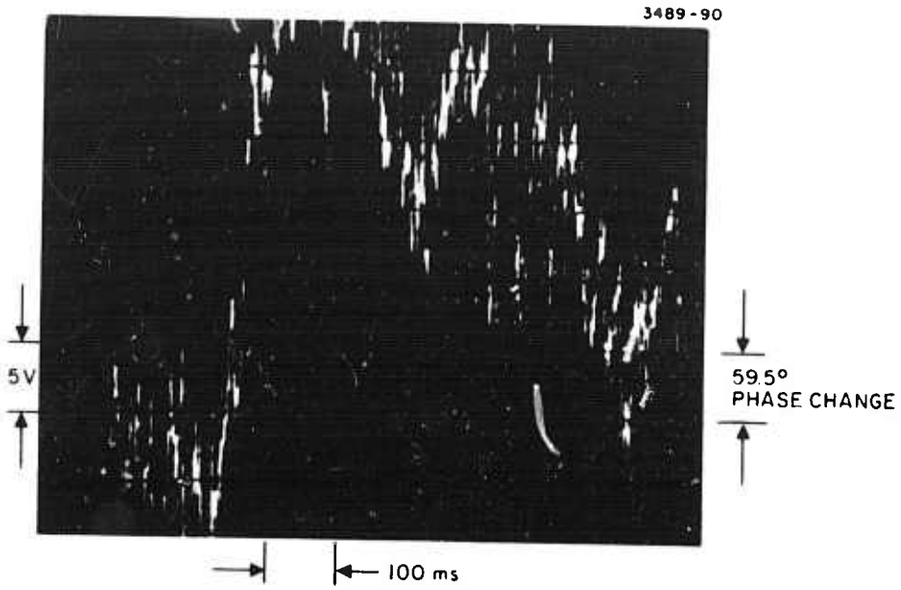

Fig. 37. Control voltage on channel 12 for high turbulence: 18 June 1974, 1200 h. C_N^2(opt) = 5.3 x 10^{-14} $cm^{-2/3}$.

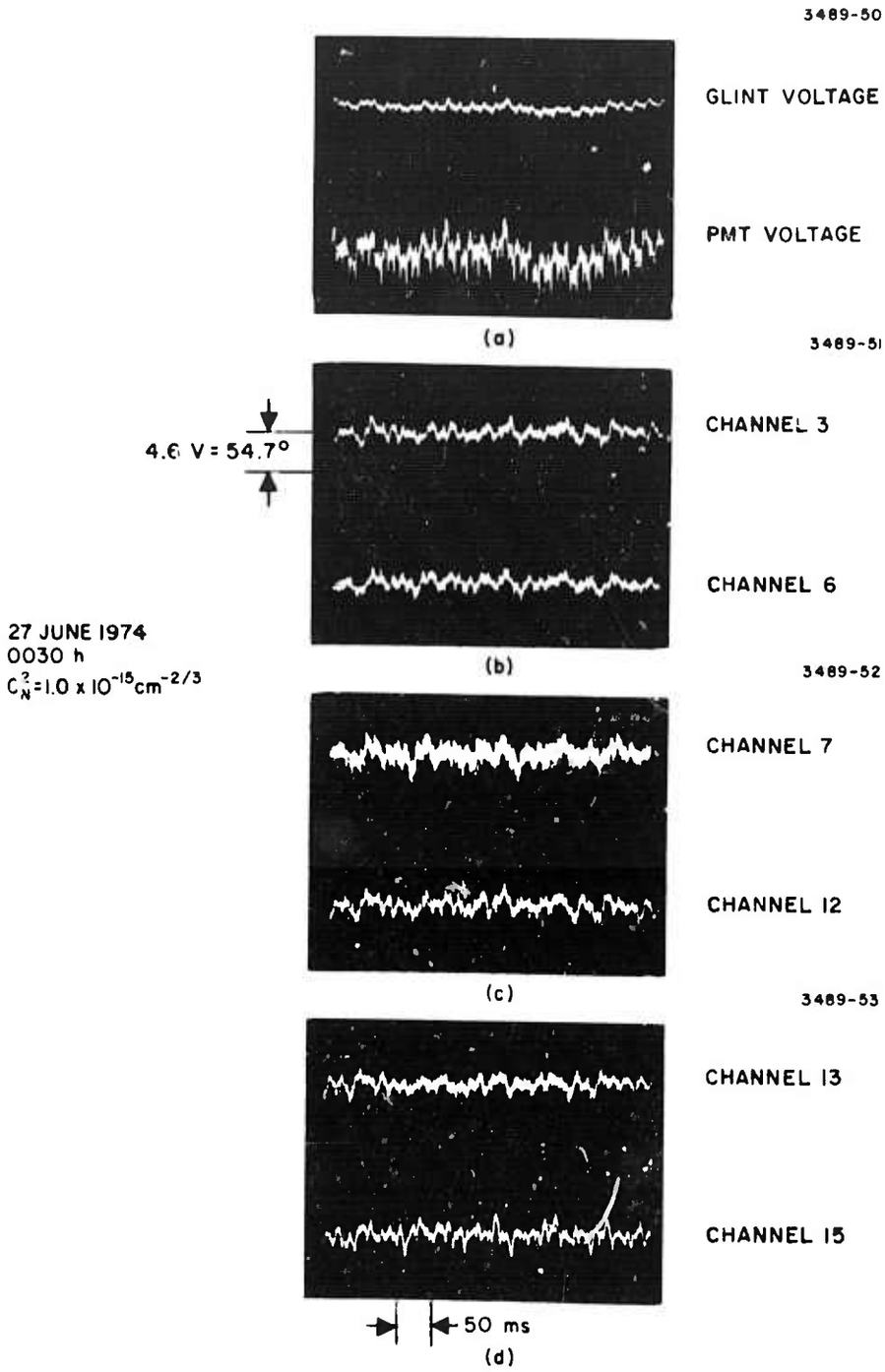

Fig. 38. Simultaneous, time-synchronized data from indicated sources. Low turbulence, 27 June 1974, 0030 h. C_N^2(opt) = 1 x 10^{-15} cm$^{-2/3}$.

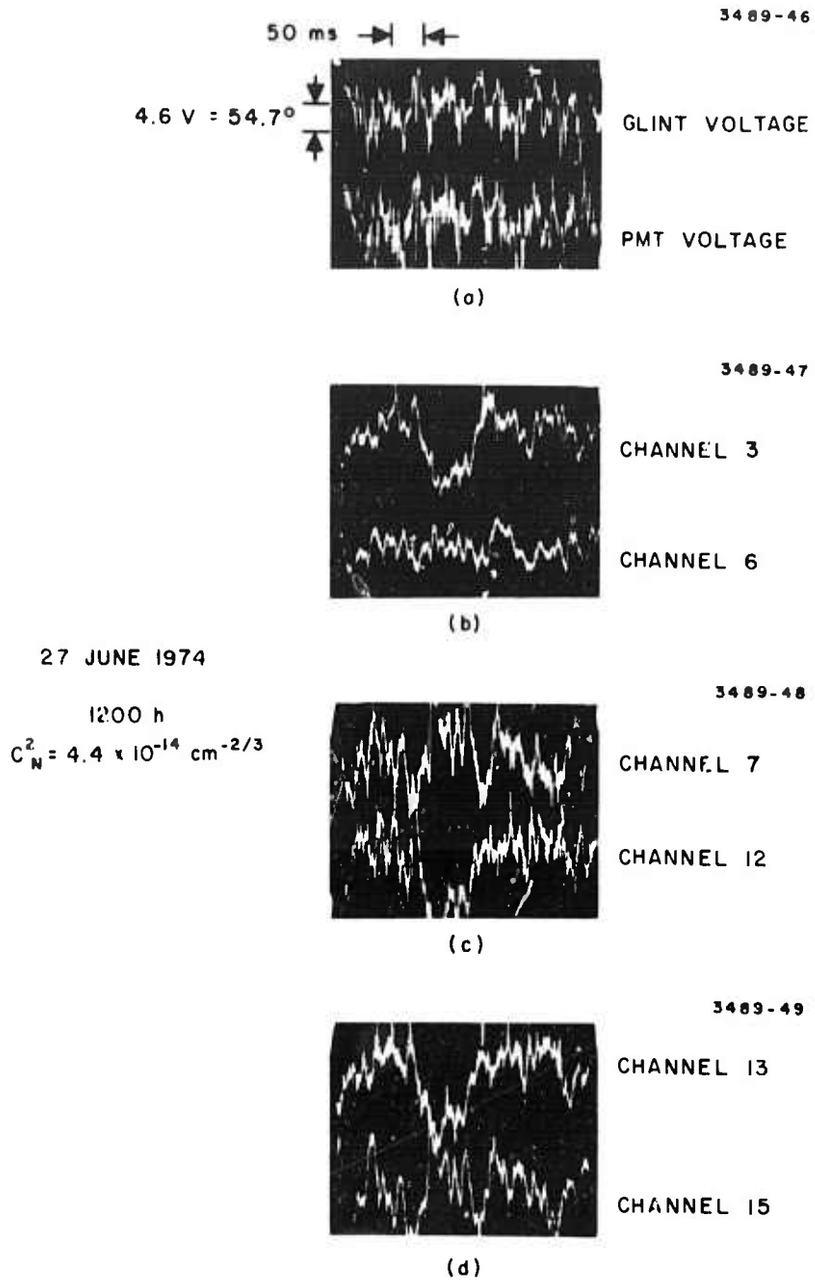

Fig. 39. Simultaneous, time-synchronized data from indicated sources. High turbulence, 27 June 1974 1200 h C_N^2(opt) = 4.4×10^{-14} cm$^{-2/3}$.

is locked on a single boresight glint. The data were taken simultaneously using the multichannel recorder (MCR) described previously. The low turbulence pictures do not convey much information since there are almost no fluctuations. The more interesting data are in Fig. 39.

The correlation between the power on the glint and the PMT voltage is apparent in Fig. 39(a). Figures 39(b), (c), and (d) show the expected general trend of phase error fluctuations, namely, elements on the same side of the transmit aperture (3, 12, and 13 (see Fig. 1)) tend to vary together and 180° out of phase with elements on the opposite side (6, 7, and 15). In particular, notice the large 15 V "square-wave" variation near the center of each trace. One explanation of this variation is that it is caused by atmospheric steering which moved the beam horizontally about 1/8 of an element null-null beamwidth or 5/8 of an array beamwidth. There is no way to verify this statement, of course, but it constitutes one more piece of evidence which points to strong atmospheric steering effects.

Spectral data corresponding to Figs. 38 and 39 are shown in Fig. 40. The low turbulence spectrum is taken from a different data run than Fig. 38, but for the same low turbulence level. Only the spectra for channel 3 error signals are presented because all channels exhibited the same time-averaged spectra. Unless otherwise noted, all of our spectral data were taken using a Quan-Tech 304DTL wave analyzer with a 10 Hz averaging bandwidth. Scan times of 50 and 500 s for the 0 to 1000 Hz scans produced identical spectra so 50 s scans were normaliy used.

TABLE IX

Simultaneous Data Recorded on Multichannel FM Recorder

A.	Six control channel output voltages applied to phase shifters (channels 3, 6, 7, 12, 13, and 15 across the transmit aperture horizontal diameter)
B.	Scintillometer log-amp output
C.	Power on the largest glint
D.	Photomultiplier output
E.	Timing marks, 30 s apart
F.	Voice channel for data identification

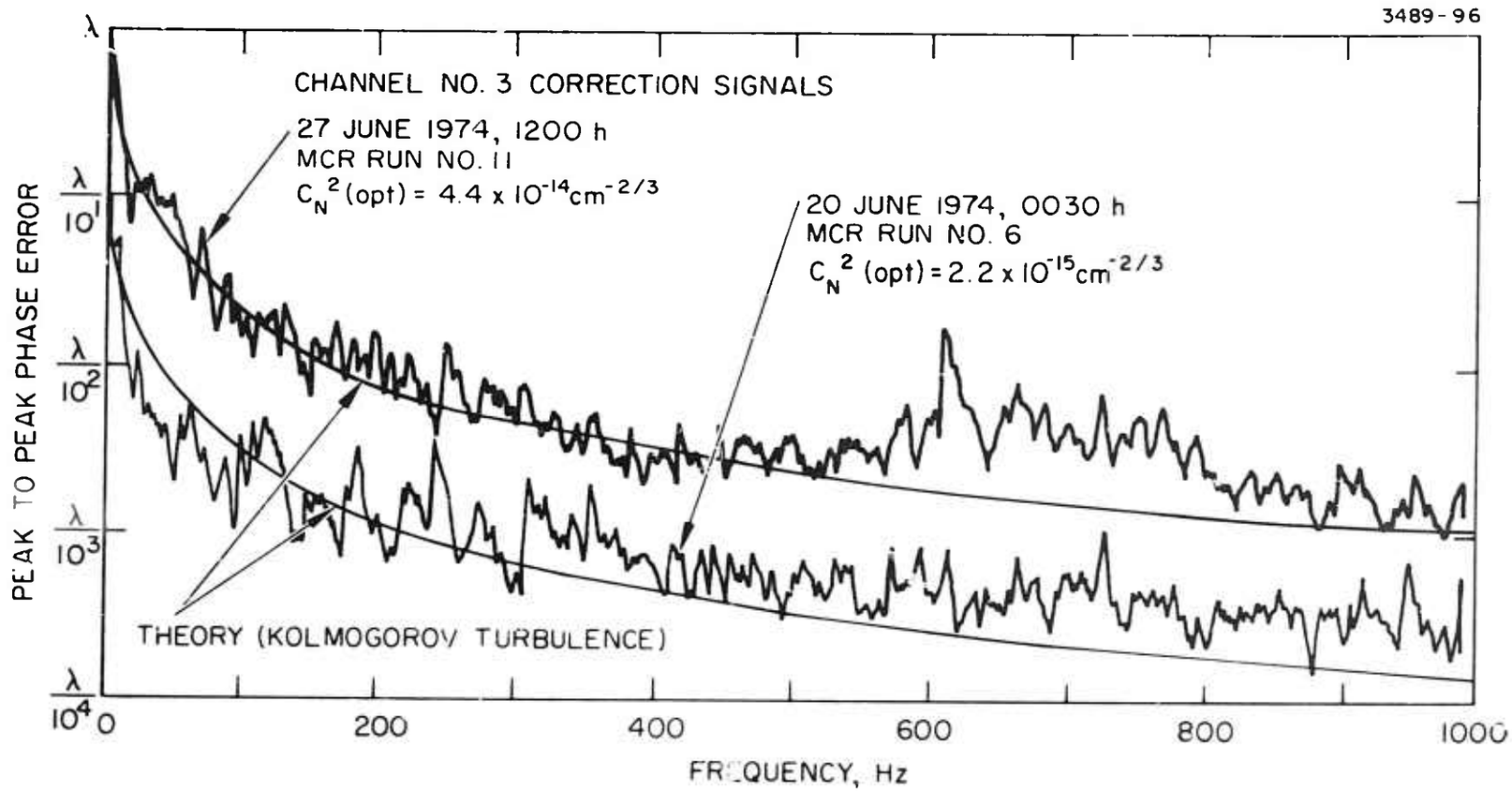

Fig. 40. Frequency spectra of control channel 3 error voltage for low and high turbulence corresponding to data in Figs. 38 and 39. Also shown is the theoretical frequency spectrum (eq. (21)).

The theoretical curve shown in Fig. 40 is found from the power spectrum, S_ϕ, of the mean square phase fluctuations along the propagation path. A Von Karman spectrum is assumed for the index variations of the form

$$\phi_n(K) = (\text{constant}) \times \left[1 + (K/K_o)^2\right]^{-11/6} \tag{19}$$

where K is the wave number of the index fluctuations, $K_o = 2\pi/L_o$, and L_o is the outer scale of the turbulence. The result for S_ϕ is[22]

$$S_\phi = (\text{constant}) \times \left[1 + \left(\frac{f}{V/L_o}\right)^2\right]^{-4/3} \tag{20}$$

where f is the frequency in Hertz and V is the transverse wind velocity. Since the experiment measures actual phase error rather than its square, the theoretical curve in Fig. 40 is

$$S_\phi^{1/2} = (\text{constant}) \times \left[1 + \left(\frac{f}{V/L_o}\right)^2\right]^{-2/3} . \tag{21}$$

The constant in eq. (20) is related[23] to the path length, the turbulence strength L_o and V. Since we have no measure of V or L_o and hence of the parameters in the constant factor, these two quantities were adjusted to give the best fit to one experimental data set and then held fixed. A value of $V/L_o = 6$ was chosen which for $L_o = 50$ cm (one-half the beam height off the roof) corresponds to V = 3 m/s = 6.7 mph. This wind speed is consistent with what was normally observed during the day on the rooftop range. The constant was set for each data run by matching the experiment and theory at an arbitrary point, f = 200 Hz. As can be seen, the agreement between theory and experiment is very good for the data in Fig. 40 and the same theoretical curve with an amplitude change fits for both high and low turbulence experimental spectra as predicted by eq. (21). The rise in the spectrum amplitude around 700 Hz is observed only in heavy turbulence and is not understood at this time.

Another example of this type of data is shown in Fig. 41 for a different day but nearly the same turbulence level. The agreement between theory and experiment is even better than in Fig. 40. To our knowledge,

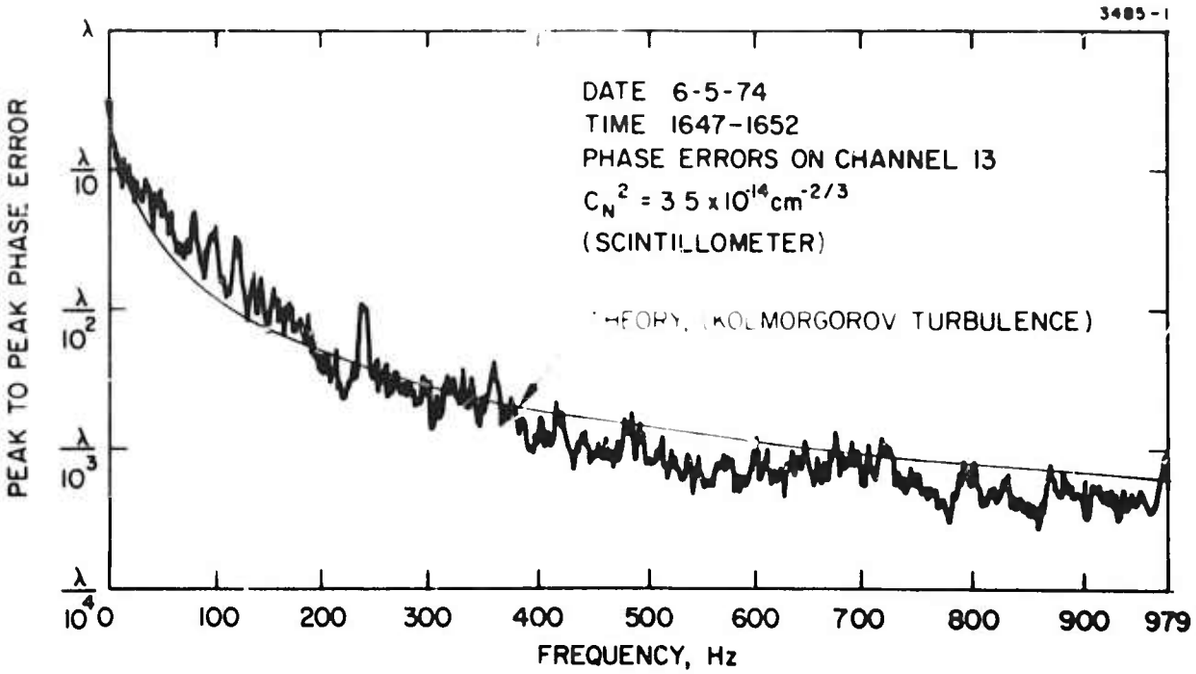

Fig. 41. Frequency spectra of control channel #13 voltage for high turbulence condition showing excellent agreement between theory and experiment.

this is the first direct measurement of atmospheric turbulence phase errors and verification of the power spectrum in Eq. (21). Other workers[24] have shown good agreement between theory and phase-difference spectra measured using optical heterodyning and fast Fourier transform techniques.

It is also interesting to compare the spectrum of a single element phase shift with the spectrum of the difference between two element phases. The individual element signals and the difference signals should have the same frequency spectrum except for an amplitude factor, the difference spectrum having a factor of $\sqrt{2}$ or 1.5 dB larger amplitude.[23]

Figure 42 shows the spectrum of channel 15 control voltage (same as channel 3 in Fig. 40) compared with the difference spectrum of channels 12 to 15. Channels 12 and 15 are along a horizontal diameter and on the outer edge of the transmit aperture (see Fig. 1). The difference spectrum does indeed have the same shape as the single element spectrum, and about 2.5 dB larger amplitude. As before, the agreement with theory is good.

The effect of transmitter diameter on the phase correction signal is shown in Figs. 43 to 46. As expected, the magnitude of the signals increases with increasing transmitter size.

Figure 47 shows one final spectral comparison for a single glint and high turbulence conditions. The increase in amplitude below 150 Hz for the "COAT on" case is indicative of the turbulence spectrum to which the system is responding.

The data shown in Figs. 40, 41, and 47 lead us to conclude that the atmospheric phase errors are insignificant above 30 to 50 Hz even in heavy turbulence. That is, a COAT system which can respond only at a 50 Hz rate will correct for all phase errors larger than one-tenth of a wave when working with a stationary, single glint target. The high speed capabilities of the RADC/COAT system are necessary, however, for tracking rapidly moving glints and for providing a rapid convergence time. In addition, when COAT servo slewing controls are added the system will be able to track moving targets over a much greater angular range than with pure phase control. The resultant slewing beam is equivalent to a transverse wind which can produce significant phase errors at rates up to a several hundred Hertz.

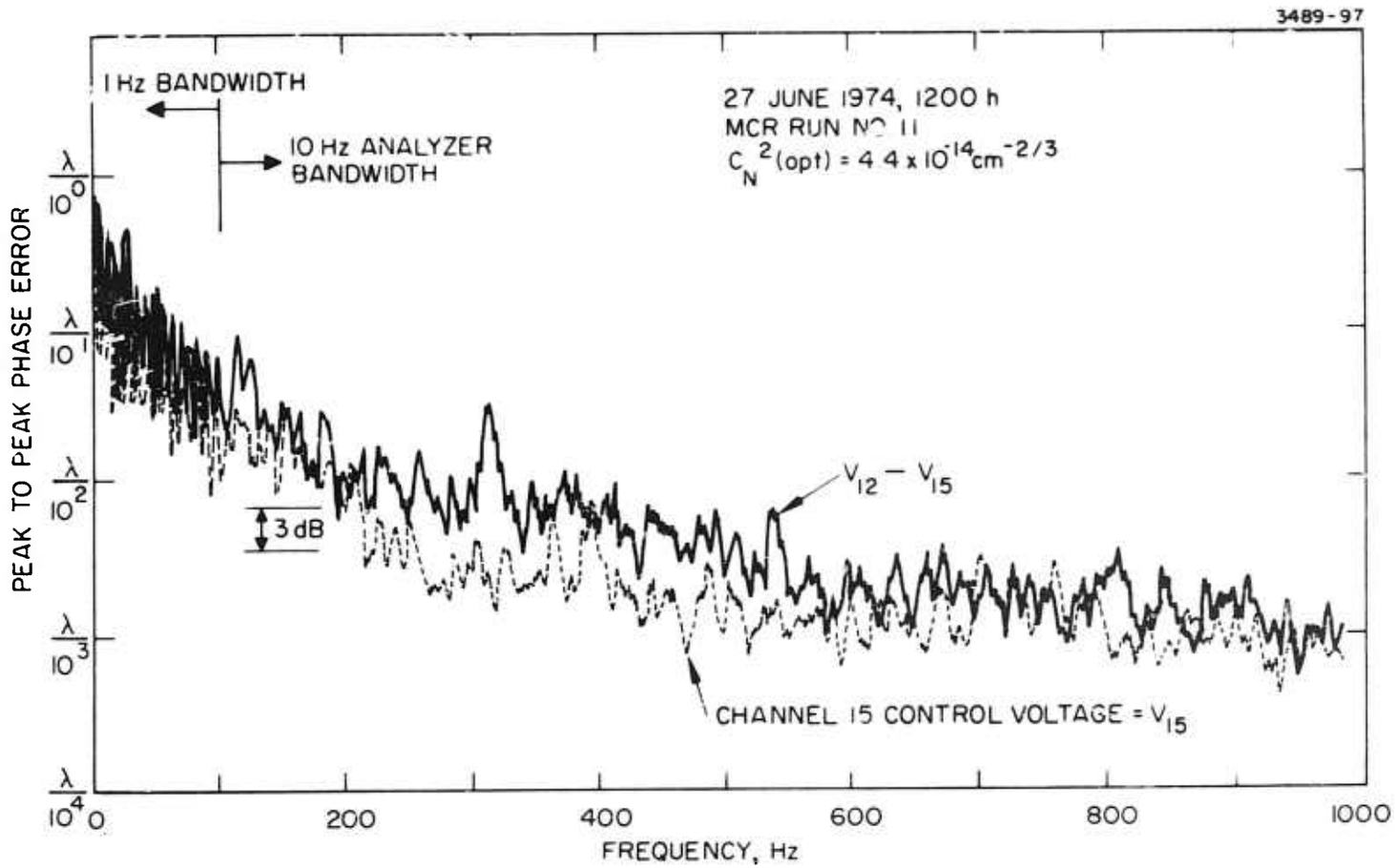

Fig. 42. Frequency spectrum of a single control channel voltage (15) compared to the spectrum of the difference in two channel voltages (12 through 15). High turbulence conditions.

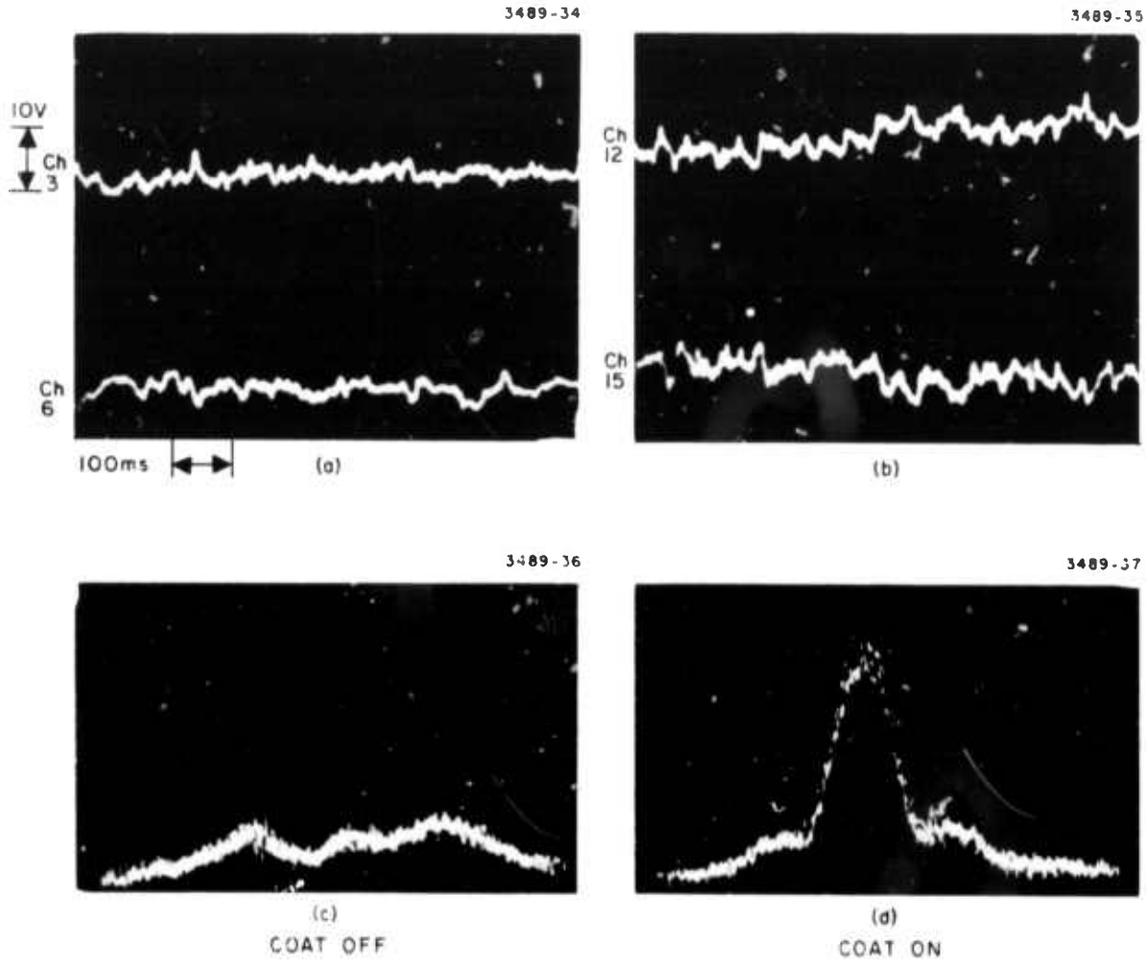

Fig. 43. Effect of transmitter diameter D_T on the magnitude of the error signals for D_T = 7.5 mm. (a) and (b) Control channel voltages. (c) Beam profile, COAT off. (d) Beam profile, COAT on.

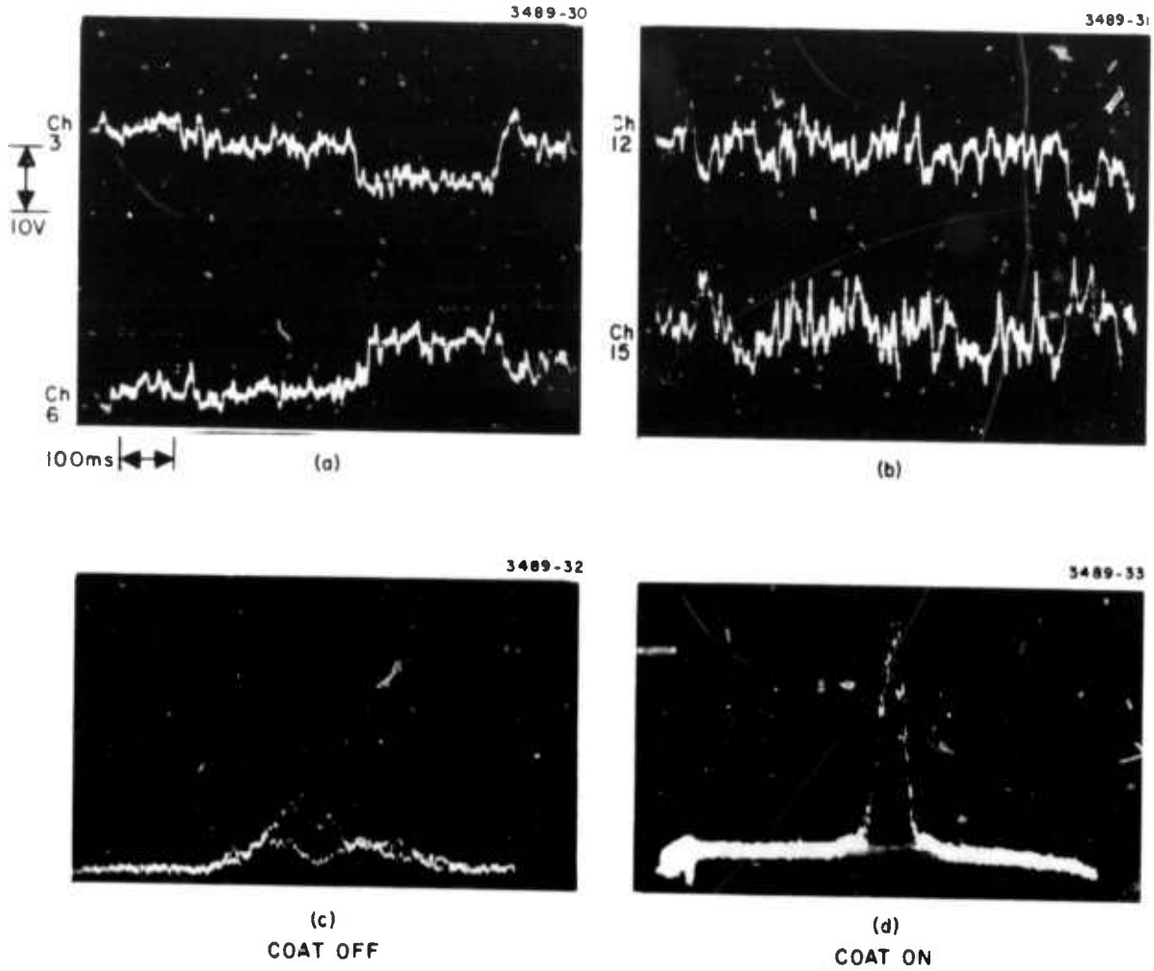

Fig. 44. Effect of transmitter diameter on the magnitude of the error signals for D_T = 15 mm. (a) and (b) Control channel voltages. (c) Beam profile, COAT off. (d) Beam profile, COAT on.

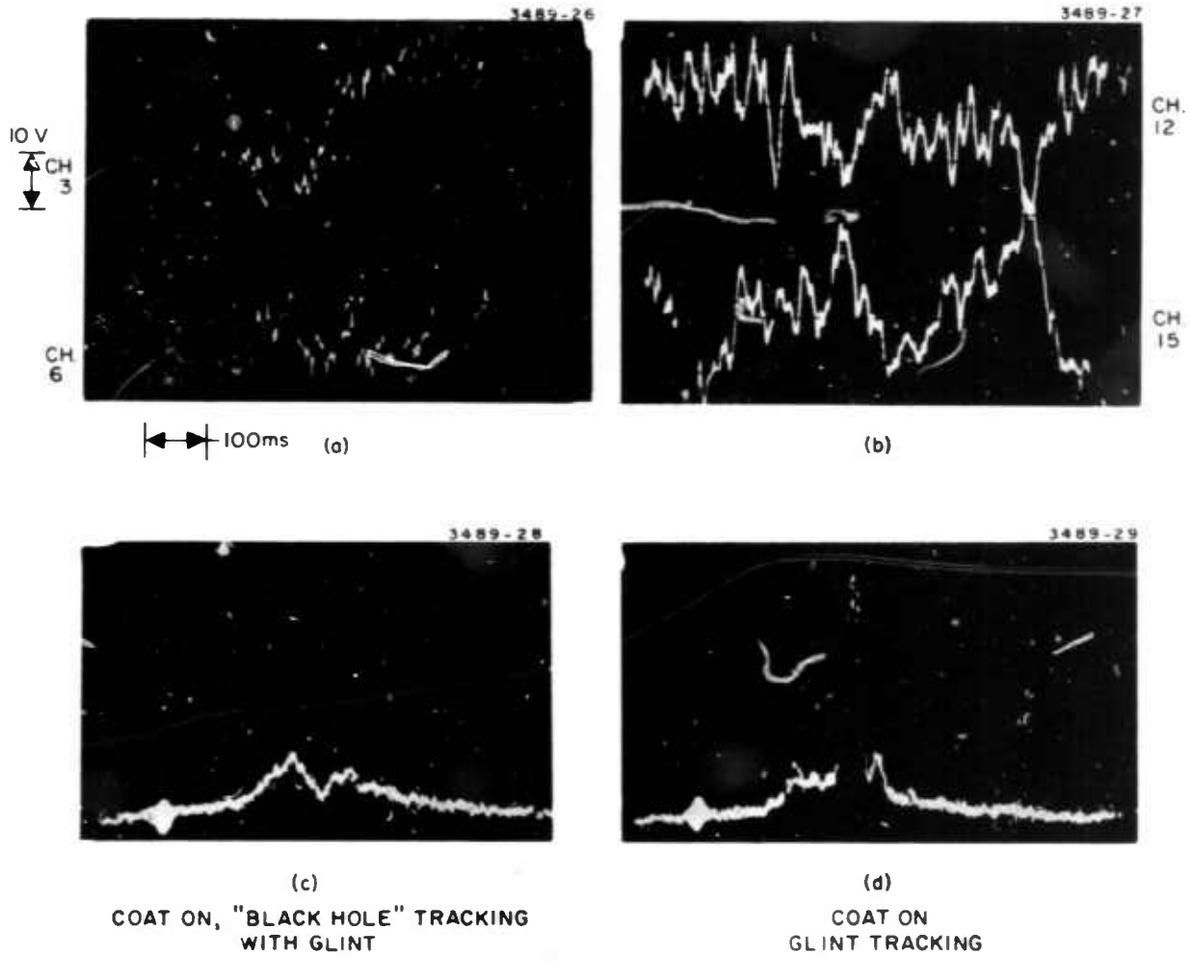

Fig. 45. Effect of transmitter diameter on the magnitude of the error signals for D_T = 30 mm. (a), (b) control channel voltages. (c) Beam profile; note the use of "black hole" tracking (loop phase reversal) instead of "COAT OFF: in (c). (d) beam profile, COAT on.

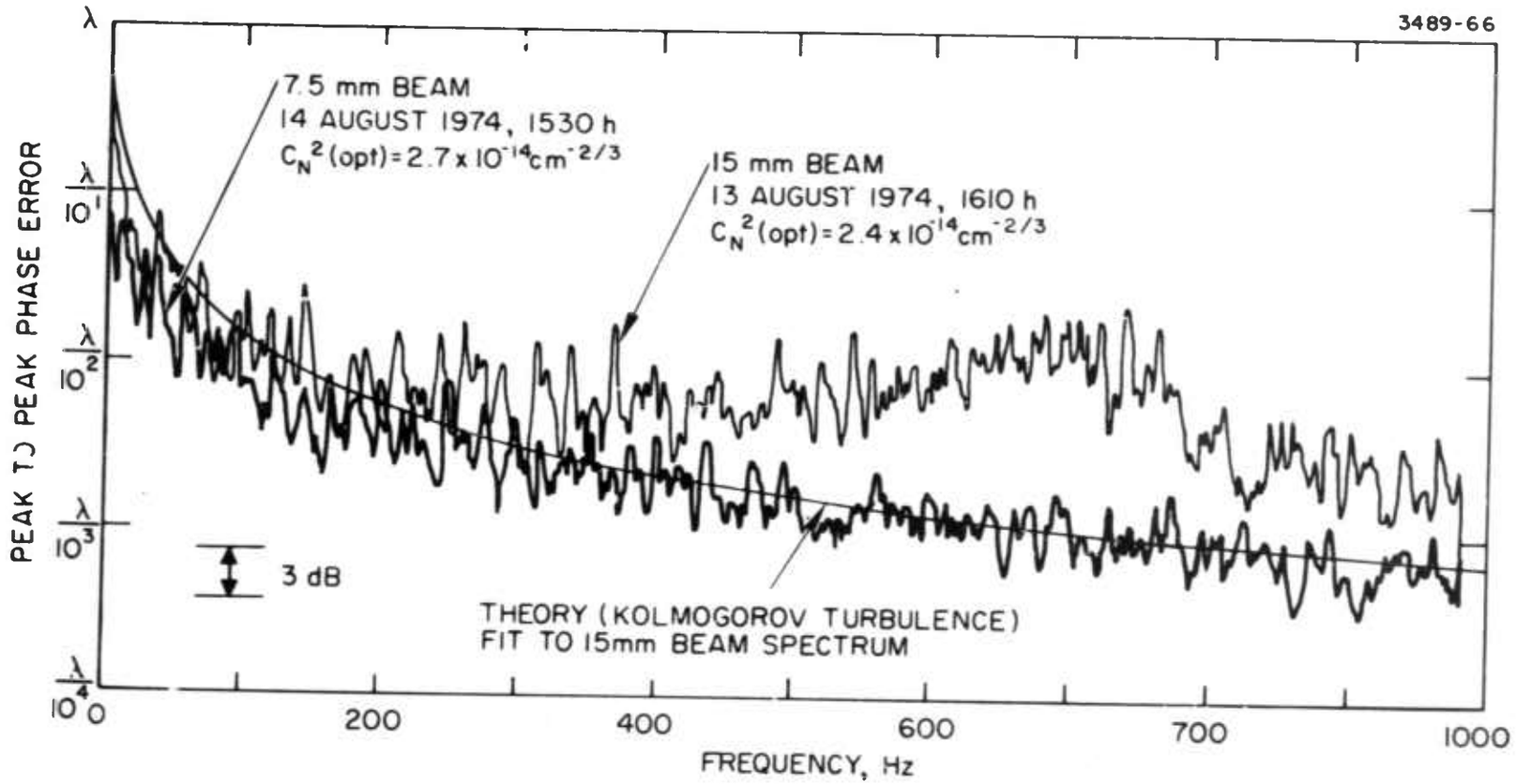

Fig. 46. Effect of a smaller beam size on error signal spectrum.

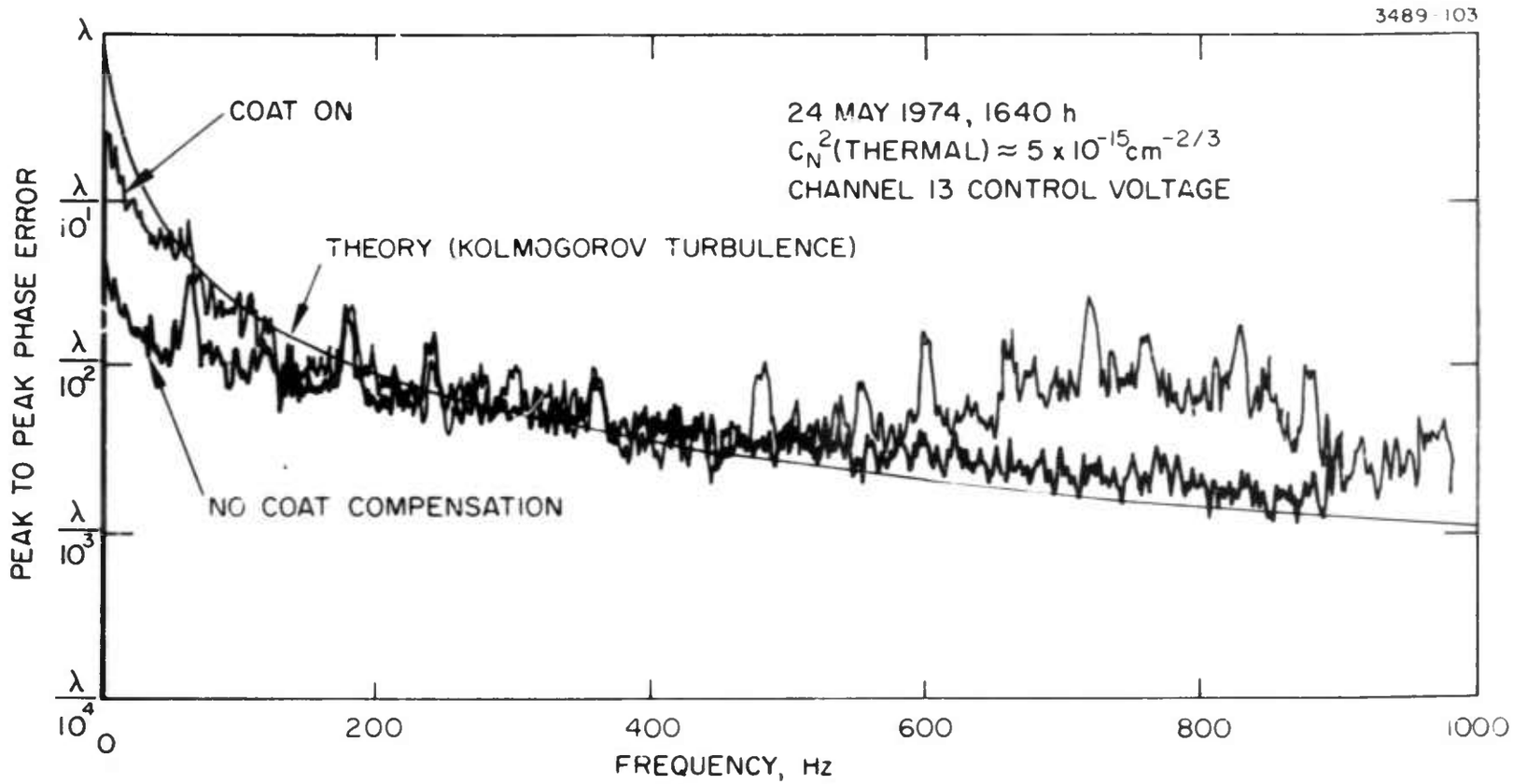

Fig. 47. Comparison of error signal spectrum for COAT on and COAT off conditions in high turbulence.

A recent calculation by Fante[25] has provided an estimate of the turbulence spectral width when there is a constant velocity wind transverse to the propagation direction. His result for the turbulence 1/e spectral width can be cast in terms of the atmospheric correlation length defined in eq. (12). Again taking $\langle\phi^2\rangle_{ave} = 1$ in eq. (12), the spectral width of the phase fluctuations in Hertz is given by

$$\Delta f = 0.69 \frac{V_T}{\rho_c} \tag{22}$$

where V_T is the transverse wind velocity in centimeters per second and the values of ρ_c for our experimental conditions are found from eq. (13) and Fig. 21. According to Fante,[25] eq. (22) is strictly valid only for $C_N^2 \gtrsim 2 \times 10^{-14}$ cm$^{-2/3}$ for our wavelength and propagation range.

For typical values of $V_T = 200$ cm/s and $\rho_c = 0.5$ cm ($C_N^2 \approx 2 \times 10^{-14}$ cm$^{-2/3}$), $\Delta f = 276$ Hz. This bandwidth is about a factor of five larger than the bandwidth of our observed error signals which may indicate much lower transverse wind velocities than 2 m/s for the data in Figs. 40, 41, and 47. Wind speeds of 5 to 10 m/s (10 to 20 mph) are commonly encountered near ground level in the atmosphere, however, and eq. (22) indicates large phase fluctuation bandwidths will be encountered. The high speed capabilities of this COAT system thus appear not only desirable, but essential for effective turbulence compensation with moving targets in normal atmospheric wind conditions.

b. Spectra of Other COAT System Quantities — Other spectra of interest are those obtained from the scintillometer, the receiver photomultiplier (PMT), and the glint power detector. The PMT spectrum in Fig. 48 and glint power spectrum in Fig. 49 correspond to the data in Figs. 38 to 40. The spectra are identical out to 200 Hz for high turbulence and have similar shapes but different relative amplitudes in low turbulence. The glint spectrum falls off faster above 200 Hz because of the slow detector response. This result is not unexpected since the low frequency PMT fluctuations are caused by the glint power fluctuations; scintillation effects on the return path are negligible because of spatial integration provided by the 8 in. diameter receiver aperture. The theoretical curve used in previous

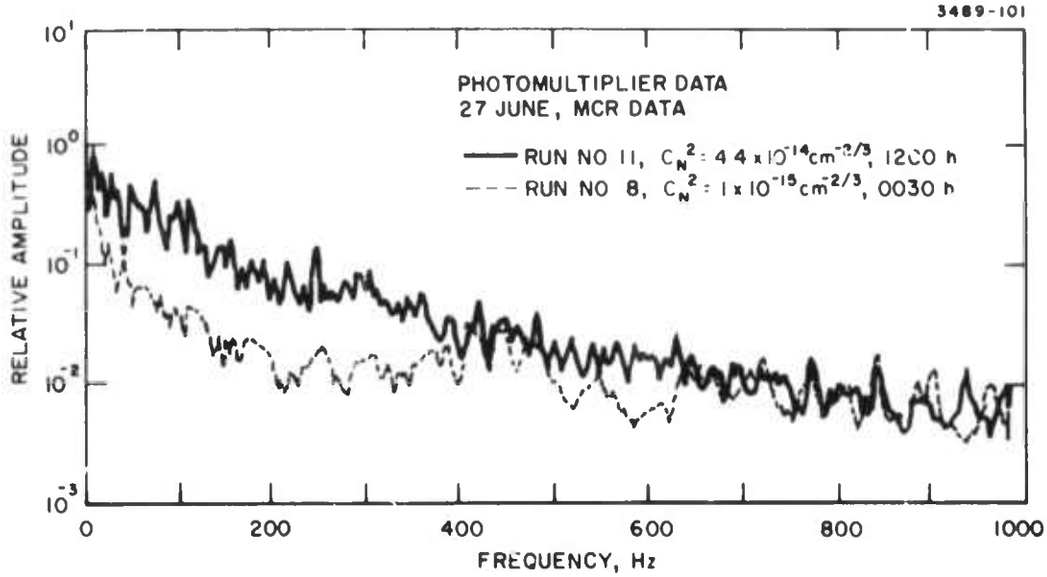

Fig. 48.
Frequency spectrum of photomultiplier output voltage for high and low turbulence conditions.

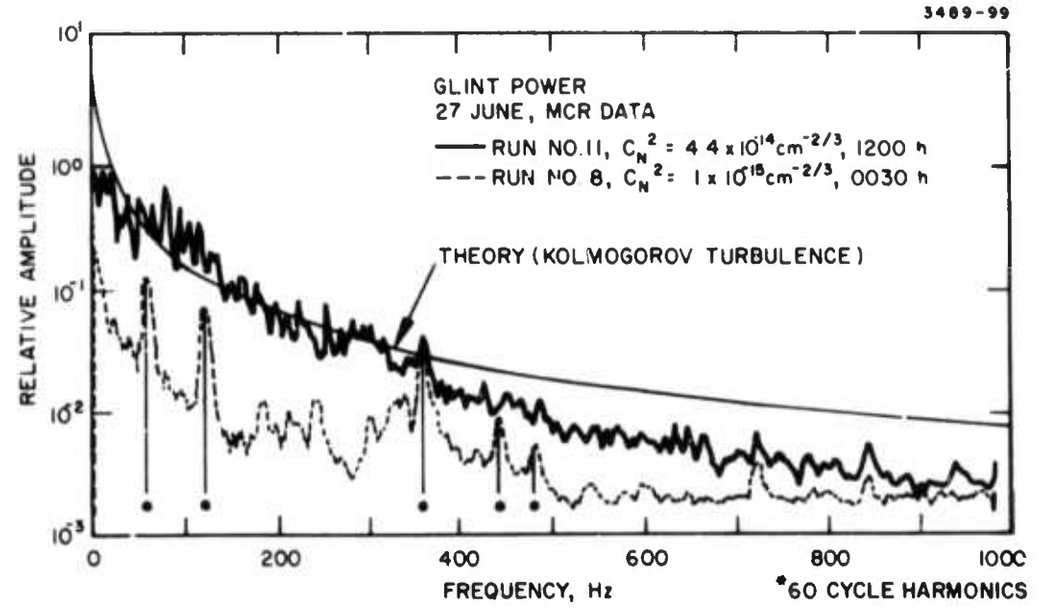

Fig. 49.
Frequency spectrum of the power on a boresight target glint for high and low turbulence conditions. The Kolmogorov turbulence spectrum shown is identical to that in Figs. 40 and 41.

spectra is shown in Fig. 49 for reference and to emphasize the difference between the spectra in Figs. 48 and 49 and those of the control voltages (Figs. 40 and 41, e.g.).

What is puzzling at first sight is the comparison of "COAT on" and "COAT off" glint and PMT spectra in high turbulence as shown in Fig. 50 for the PMT (the glint spectra are the same). The shapes of the curves for "COAT on" and "COAT off" are the same and the amplitudes differ by about a factor of 10 reflecting the lower average power on the target with the COAT loop open. We initially expected the low frequency glint spectrum to be significantly reduced by the action of the COAT system. Since such a reduction does not occur, since the control voltages have a Komolgorov turbulence phase spectrum which is not observed on the glint power spectrum, and since the COAT-formed beam peak power and beamwidth are close to the diffraction-limited values, we are led to conclude that the spectra in Figs. 48 to 50 contain significant contributions from atmospheric beam-steering effects. This conclusion will explain the data in Fig. 50 and is supported by other data presented earlier in this report (see Fig. 36(b), e.g.).

One further bit of evidence for strong beam steering effects is shown in the scintillometer spectra of Fig. 51. Only the low turbulence spectrum agrees with the theory. Since the theory treats only average phase fluctuations, we attribute the larger low-frequency content of the high turbulence spectrum to steering of the scintillometer beam. The drop in the experimental scintillometer spectrum below 20 Hz is caused by a high pass filter used in recording the data on the multichannel recorder.

5. Single Moving Glint

In order to measure the COAT system's ability to track a single moving glint, the following test was conducted in high turbulence. A single glint was positioned so that it moved through the boresight axis and out of the element pattern along an elliptical arc (see Fig. 3). The power on the glint was then recorded as a function of time for different glint angular velocities relative to the transmitter. The test results shown in Fig 52 indicate that the system is doing a reasonable job of tracking at rates up to 14 mrad/s. The quality V_p/V_m in each figure is a measure of the peak glint power (V_p) relative to that observed at very low glint velocities (V_m).

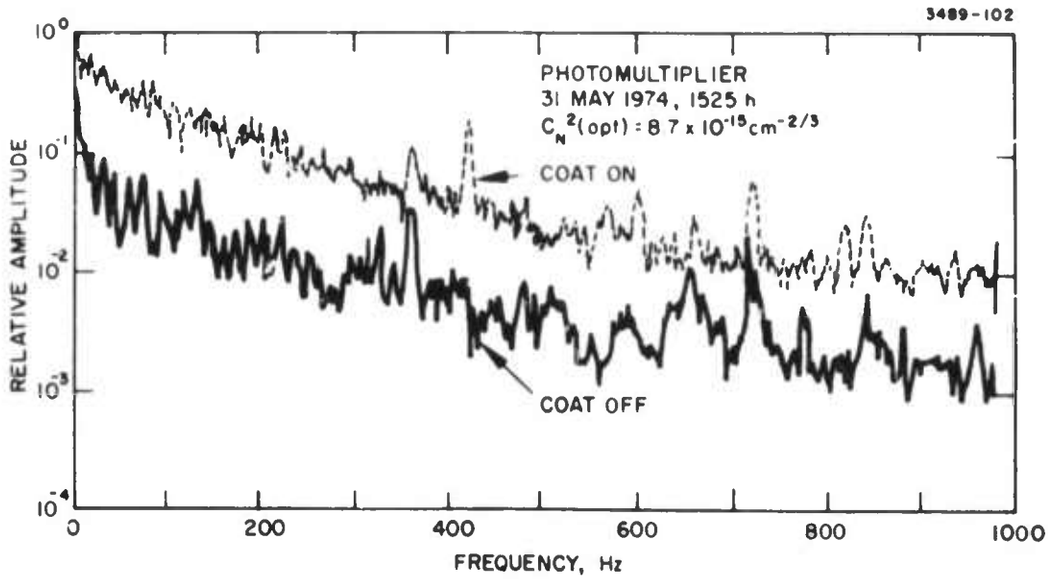

Fig. 50.
Comparison of photomultiplier spectrum for "COAT ON" and "COAT OFF" (open loop). High turbulence.

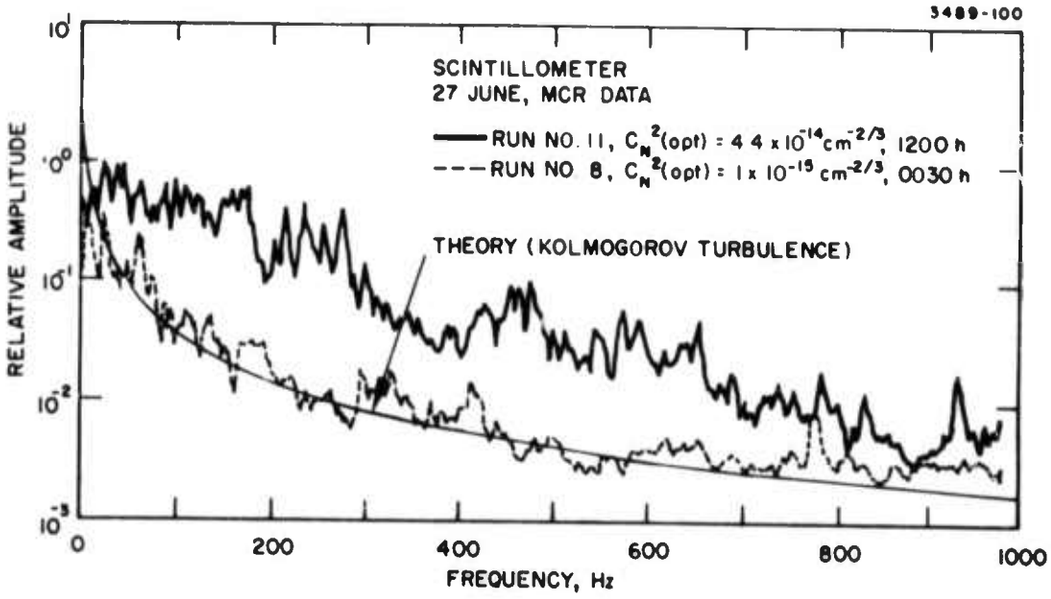

Fig. 51.
Scintillometer spectra for high and low turbulence showing a Komogorov turbulence spectrum only for low turbulence.

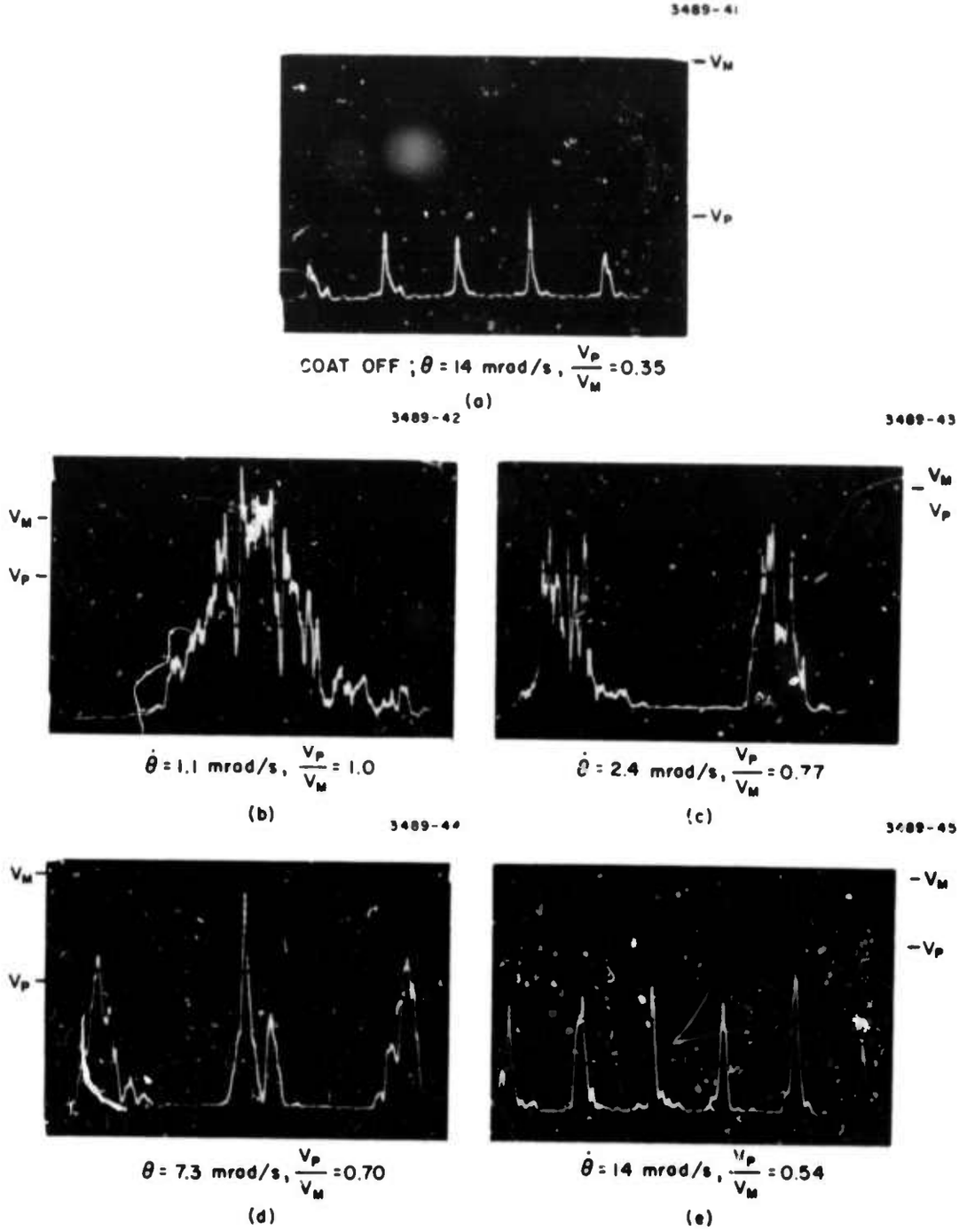

Fig. 5. Power on a single moving glint for different glint angular velocities, $\dot{\theta}$. The quantities V_p and V_m on each figure are discussed in the text. (a) $\dot{\theta}$ = 14 mrad/s, COAT loop open. (b) COAT on, $\dot{\theta}$ = 1.1 mrad/s. (c) COAT on $\dot{\theta}$ = 2.4 mrad/s. (d) COAT on $\dot{\theta}$ = 7.3 mrad/s. (e) COAT on $\dot{\theta}$ = 14 mrad/s.

At 14 mrad/s, the peak glint power has fallen to 54% of the maximum power on a stationary or slowly moving glint.

C. Multiple Glint Measurements

An essential requirement for any practical COAT system is that it must be able to converge the transmitted beam on the strongest glint present in a complex, multiglint target. We have run several tests to demonstrate the glint discrimination ability of the RADC/COAT system. Most of the tests used two cats-eye glints, but some involved multiple glints and Scotchlite sheet as discussed below.

1. Glint Discrimination

The previous report[4] indicated that for no turbulence, two glints must differ by 1 to 2 dB in order for the COAT system to completely ignore the weaker one. The experimental data also showed, however, that for exactly equal glints the system could converge in such a way that equal power appeared on each glint. This type of behavior has also been observed on the range if the glints are nearly equal in reflectivity (within 1 dB in low turbulence, 2.[illegible] dB in high turbulence).

This power sharing is very disturbing since it was expected to occur only when using very small receiver apertures (smaller than the transmitter). The effect of using a small receiver aperture is shown in Fig. 53 for low turbulence and in Fig. 54 for high turbulence. In Fig. 53 the target beam intensity profiles and contours are indicated in (a) through (f). The power on each glint shown in Fig. 53(g) illustrates how well the power is divided between the two glints. It should be noted, however, that the relative strength of the two glints had to be adjusted very carefully to produce the data in Fig. 53; a relative change of roughly 1 dB would cause the beam to form up as shown in Figs. 53(a) and (b) or (c) and (d). Similar data for high turbulence in Fig. 54 also show power sharing although the power on each glint is not nearly as stable as it is for low turbulence. Notice in Figs. 53(d) and (e) that the beam forms completely on the stronger glint when the glints have a 2:1 reflectivity ratio. This is true even though the receiver diameter is less than one-half that of the transmitter.

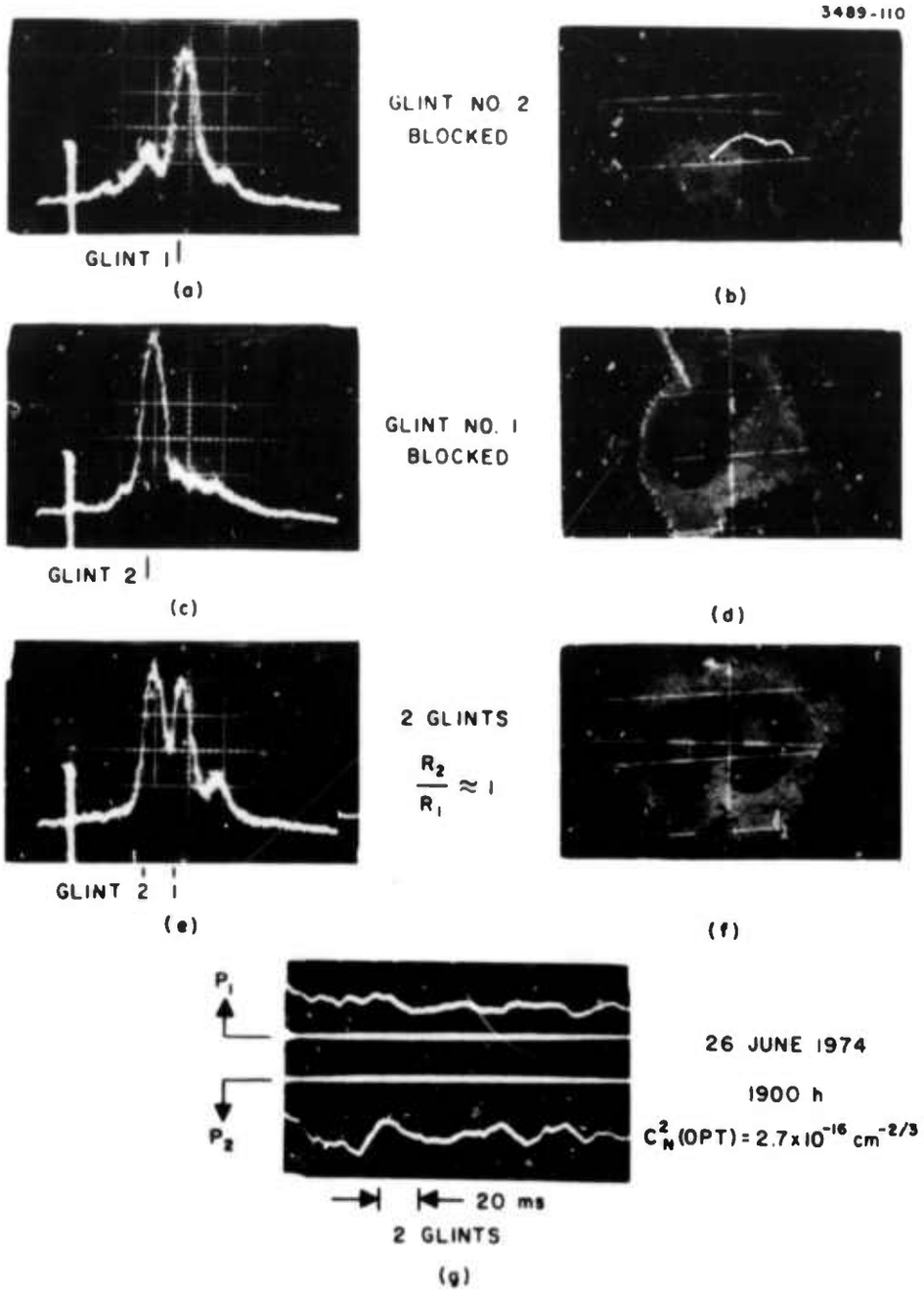

Fig. 53. Beam formation on two equal resolved glints, low turbulence and small receiver aperture (2.5 mm). Figures 53(a), (c), and (e) show scans through the center of the intensity contours pictured in (b), (d), and (f). Figure (g) shows the power on each glint as a function of time.

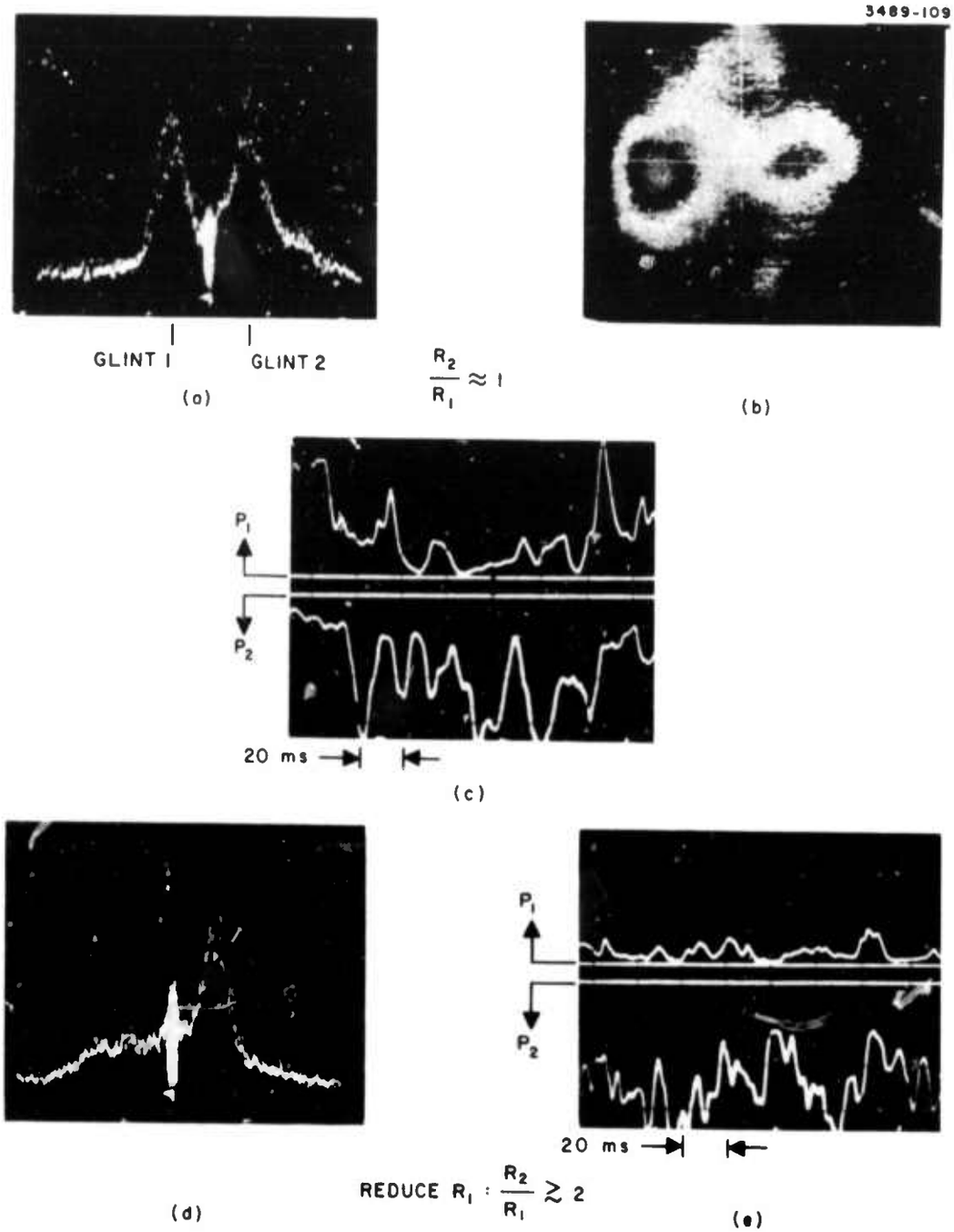

Fig. 54. Beam formation on two resolved glints, high turbulence and small receiver aperture (6.5 mm). (a), 9b), and (c) are for R_2/R_1 1. (d) and (e) For R_2/R_1 2. (a) Beam profile. (b) Beam intensity contours. (c) Power on each glint. (d) Beam profile. (e) Power on each glint.

Since the receiver apertures used for the data in Figs. 53 and 54 are much less than the transmitter, it is not too surprising that power sharing occurs. We note in passing that the smaller receiver apertures used (2.5 mm in low turbulence, 6.5 mm in high turbulence) produced too small a signal-to-noise ratio for stable operation. That such small receivers could be used at all, however, indicates an ample signal-to-noise ratio when using the full 8 in. diameter aperture.

What is surprising is the power sharing shown in Figs. 55 and 56. These data were obtained using one-fourth (one quadrant) of the full annular receiver aperture (8 in. o.d., 2.5 in. i.d.). Figure 55 shows data taken in low turbulence and Fig. 56 presents similar data for high turbulence. The relative strength of the two glints was very critical in these tests, particularly in high turbulence. The size and position of the receiver aperture mask was also very critical; small changes would cause the beam to lock stably onto one of the two glints. Figure 56(a) shows, in fact, that the power sharing in high turbulence is not very stable; the system tends to lock onto one glint, but switches from one to the other.

At this time we do not understand why the system should try to divide power between two glints when a large receiver aperture is used. A curious feature of the power sharing is that the peak power on a glint does not change much when the system tries to form the beam on both glints (compare (a), (c), and (e) in Figs. 53 and 55). This is the same type of behavior observed with an 8-element linear array in the laboratory.[4] The computer has never shown this type of behavior although a lesser degree of power sharing has been observed[4] depending on the spacing of the two equal glints. Further study and analysis will be required to determine if this behavior is a fundamental property of this type of COAT system or, as indicated by our computer simulation results, it is related to the particular hardware configuration.

The usual behavior of the system with the full receiver aperture in high turbulence is shown in Fig. 57. The two glints are nearly equal in reflectivity. Figure 57(a) shows that the beam is always formed on one glint or the other, but not on both simultaneously. Figures 57(b) and 55(c) compare the power on one glint when both glints are present to the photomultiplier signal. Notice that the total PMT signal does not follow the changes in the power on one glint. Evidently the beam is being formed in

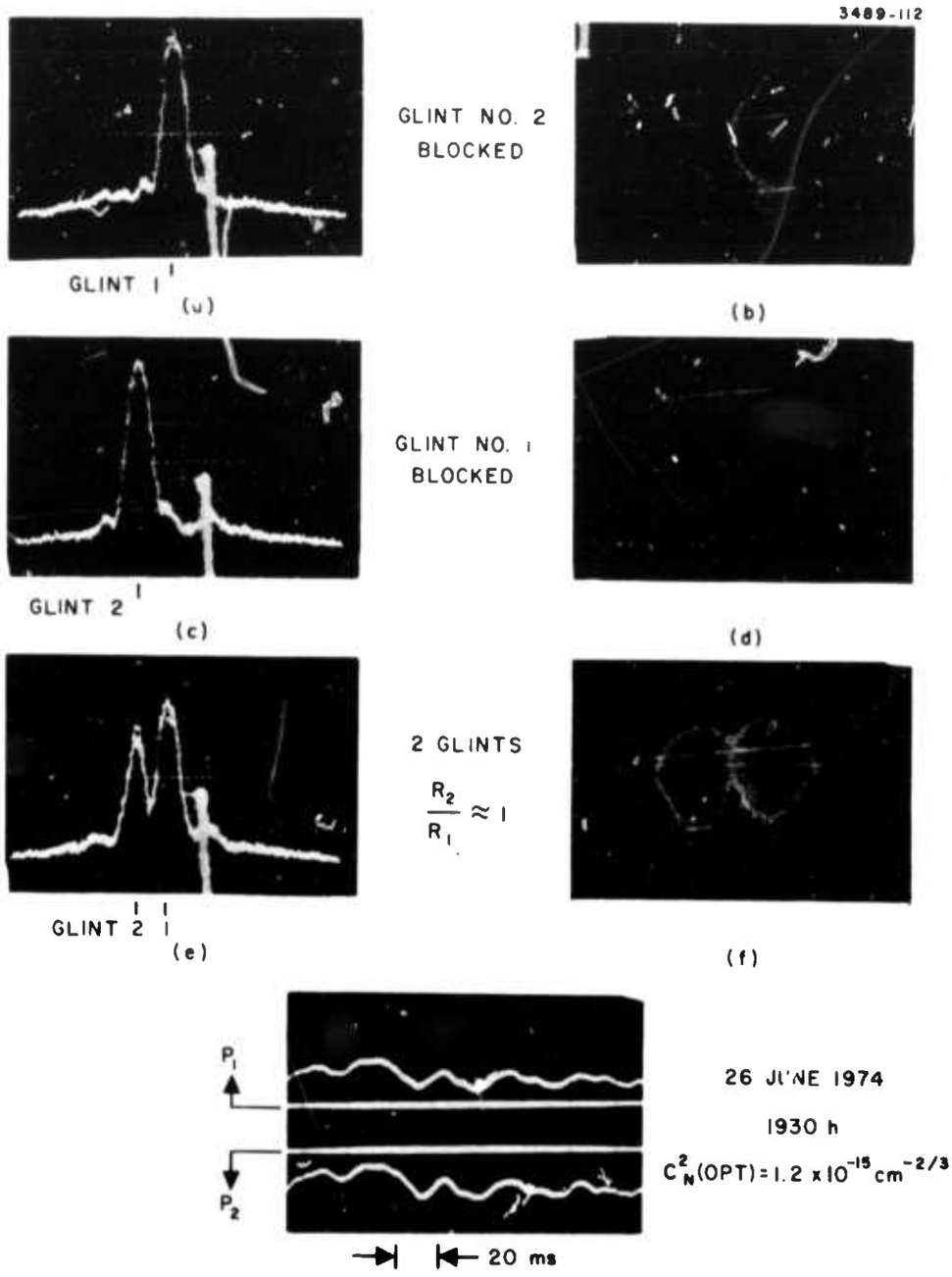

Fig. 55. Beam formation on two equal resolved glints, low turbulence and large receiver aperture (1/4 full aperture). Figures (a), (c), and (e) show scans through the center of the intensity contours pictured in (b), (d), and (f). Figure (g) shows the power on each glint as a function of time.

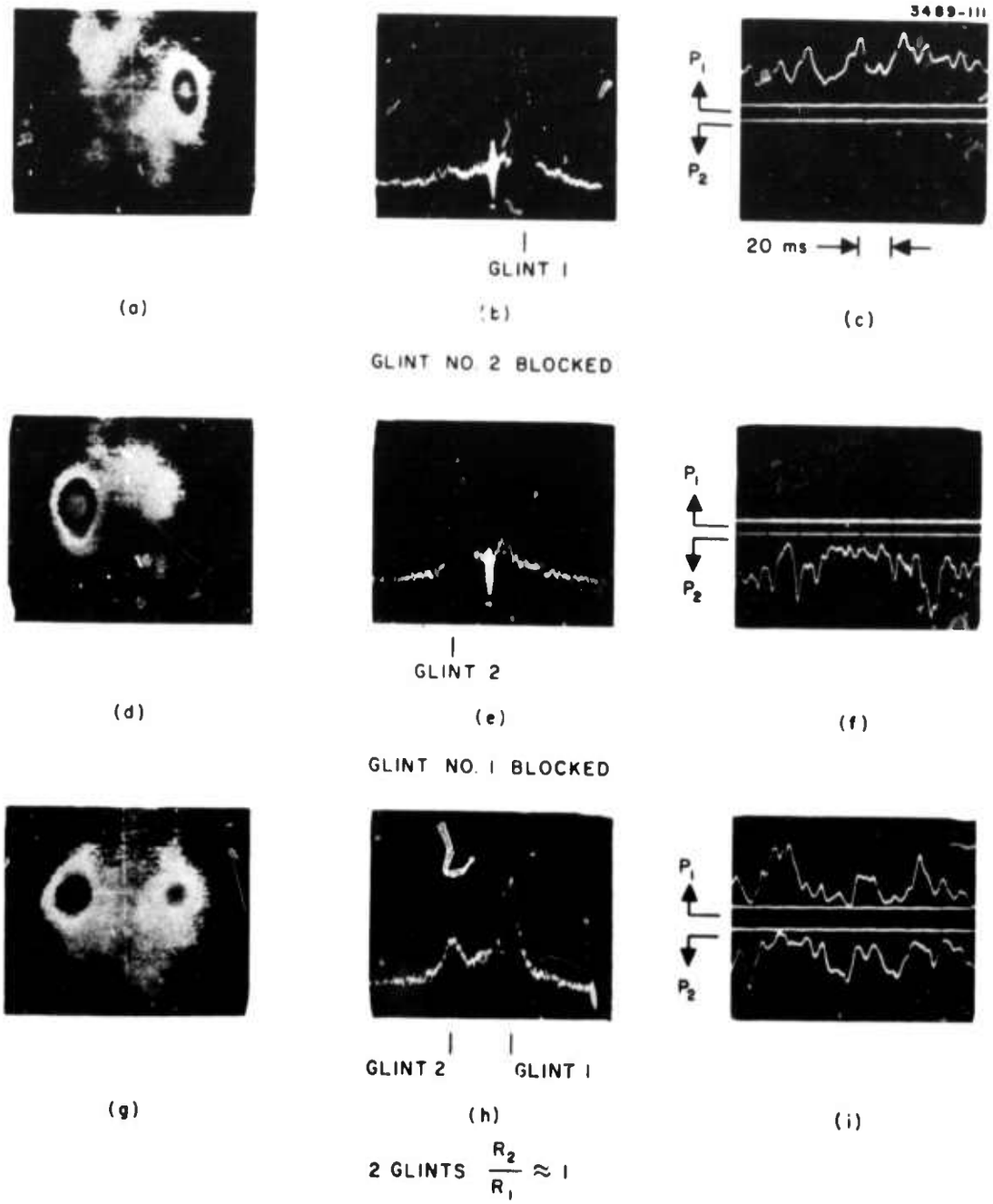

Fig. 56. Beam formation on two equal resolved glints, high turbulence and large receiver aperture (1/4 full aperture). The left column shows the intensity contours for each glint and for the pair of glints. The center column shows the corresponding beam profiles and the right column illustrates the power on each glint for the three cases.

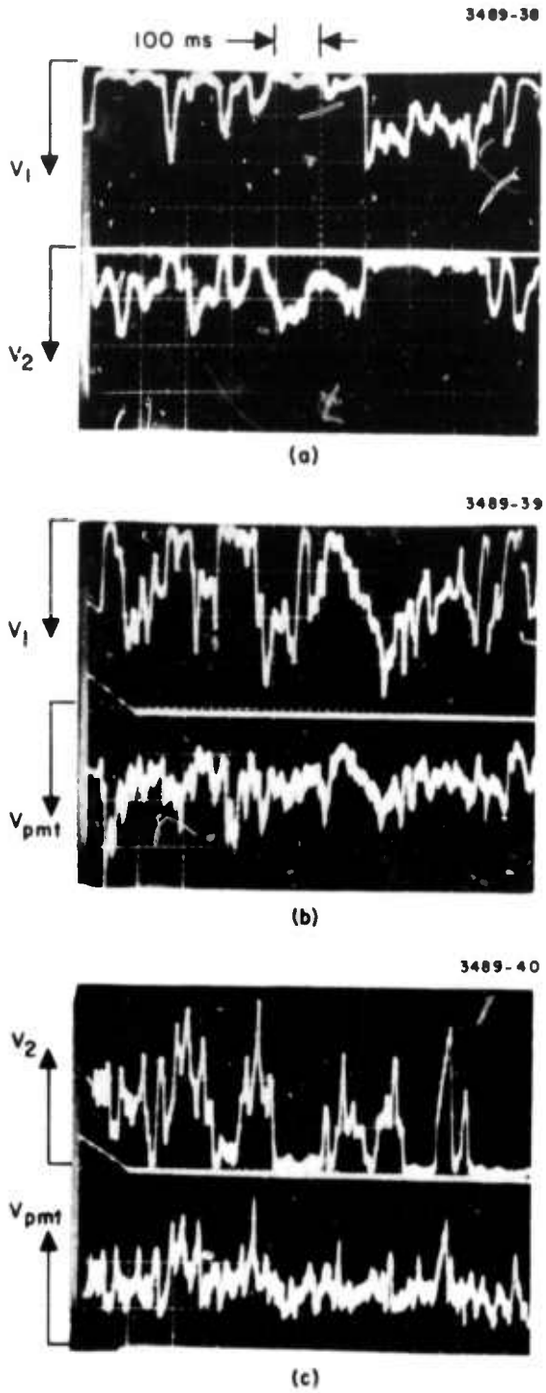

Fig. 57.
Beam formation on two equal resolved glints using the full receiver aperture. 13 June 1974, 1130 h, C_N^2(opt) = 3.8×10^{-14} $cm^{-2/3}$.
(a) Power on each glint.
(b) Power on glint 1 compared to the photomultiplier (PMT) signal. (c) Power on glint 2 compared to PMT signal. Little power sharing between the glints is observed.

such a way that the total received signal is held nearly constant. The switching between glints is very likely caused by atmospheric beam steering.

2. One Moving and One Stationary Glint

The previous section discussed the system behavior with two resolved stationary glints. An interesting question is what happens if one glint moves while the other remains fixed, both glints at all times resolved by the transmit aperture. When the glints differ in reflectivity by at least 3 dB ($R_2/R_1 \geq 2$), the system will lock onto the glint with the strongest net return (reflectivity multiplied by the element amplitude envelope). This type of behavior is shown in Fig. 58 for high turbulence for two different glint velocities; the moving glint has the larger reflectivity by a factor of 2. The power is always on one glint or the other. The high turbulence level does produce some switching from one glint to the other which is more pronounced at higher angular velocities (Fig. 58(b)). It is probable that this switching is caused by beam steering in the strong turbulence.

Since we have a computer code which models the complete RADC/COAT system, we can study these multiple glint scenarios in some detail. We have recently found some instabilities in the computer code, however, which occur with multiple glints when at least one is moving. The problem does appear to be a numerical one; the instabilities are not indicative of probable behavior of a real COAT system. We have not found the cause of the computational instability yet, but until it is corrected, we must be very cautious about drawing general conclusions based on computer simulations of moving glint scenarios.

The simulation results are interesting, however, so with the above warning in mind we have made several studies. The first series of runs have the moving glint passing within one-half an array beamwidth* of a 5 dB smaller glint on the boresight axis. The arrangement is shown in the inset to Fig. 59. At its closest approach, the moving glint (2) is 4 dB stronger in net reflectance. The data in Fig. 59 indicate a good tracking performance at angular velocities up to 10 mrad/s, the design goal of this system. At higher velocities, however, the power rapidly drops toward the side lobe

*"Beamwidth" is defined here as the null-null beamwidth of the array formed on boresight.

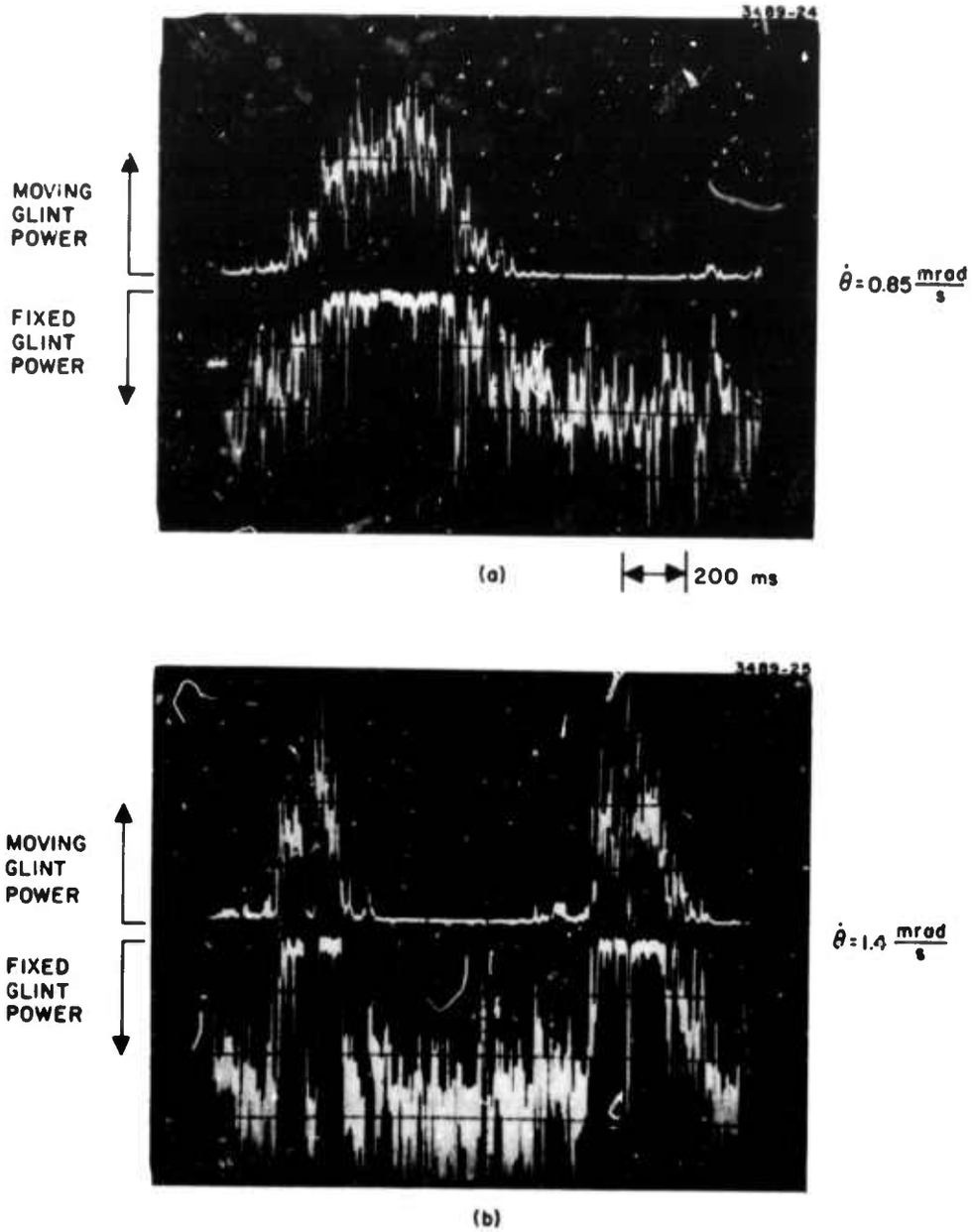

Fig. 58.
Power on each of two glints when one is stationary and one is moving. (a) Moving glint angular velocity is $\dot{\theta}$ = 0.85 mrad/s. (b) $\dot{\theta}$ = 1.4 mrad/s 18 June 1974. 1430 h, C_N^2(opt) = 4.4 x 10^{-14} $cm^{-2/3}$. The moving glint is 3 dB larger in reflectivity.

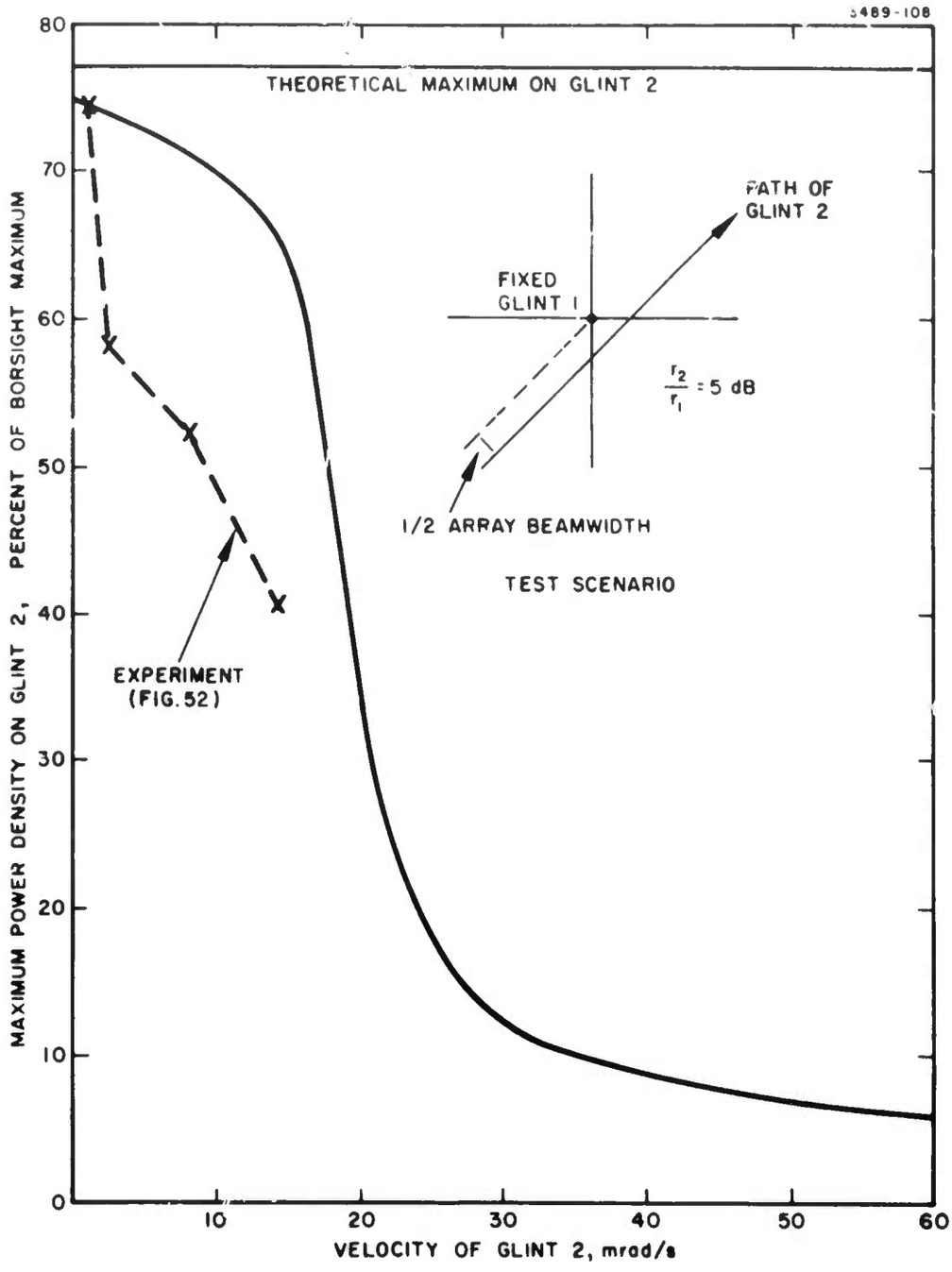

Fig. 59. Computer simulation results showing maximum power density on a glint moving near a stationary weaker glint. The moving glint (2) has a 5 dB larger reflectivity than the stationary boresight glint. The experimental points are plotted from the data shown in Fig. 52.

level of the array formed on the boresight glint. A random initial phasing was used for all these tests so the COAT system will initially begin converging the beam on the boresight glint, changing to the moving glint as it moves into the element pattern.

Figure 60 shows the same type of test as in Fig. 59, but for a different glint arrangement. The stationary glint No. 1 is now off the boresight axis and at closest approach moving glint 2 is 8.4 dB stronger. Compared with the test in Fig. 59, tracking of the moving glint is not quite as good at 10 mrad/s, but is substantially better at velocities above 30 mrad/s.

The time required for the moving glint to go from the element pattern null to its closest approach to boresight is approximately $75/\dot{\theta}$ where $\dot{\theta}$ is the angular velocity in milliradians per second. Since the system has a 1.5 ms convergence time, at velocities above 50 mrad/s the glint will have moved halfway across the element pattern in one convergence time. It is thus not surprising that the system has a poorer tracking performance at the higher glint velocities; the system barely has time to converge on the moving glint.

Because of the selected target design, we cannot produce linear glint motion. With one glint fixed in position, we can cause a second glint to move close to it along an elliptical path as shown in Fig. 3. Figure 61 shows the time-resolved power on the two glints for just such a scenario in strong turbulence. In Fig. 61(a), the moving glint has twice the reflectivity of the stationary glint. The tracking is very good with the beam remaining formed on the moving glint once the system acquires and converges on it. Only once, during the last acquisition shown in Fig. 61(a), does the system switch momentarily to the stationary glint after converging the beam on the moving glint. This performance is similar to that shown in Fig. 58.

In Figs. 61(b) and (c) the glints are nearly equal in reflectivity. The "moving" glint has been positioned at its point of closest approach to the stationary glint in Fig. 61(b). The system switches the beam convergence in a rapid and irregular manner between the two glints. Notice, however, that the power is entirely on one glint or the other, never shared equally between the two. This is the more easily observed system behavior (see Fig. 57 also) rather than the sharing indicated in Fig. 56.

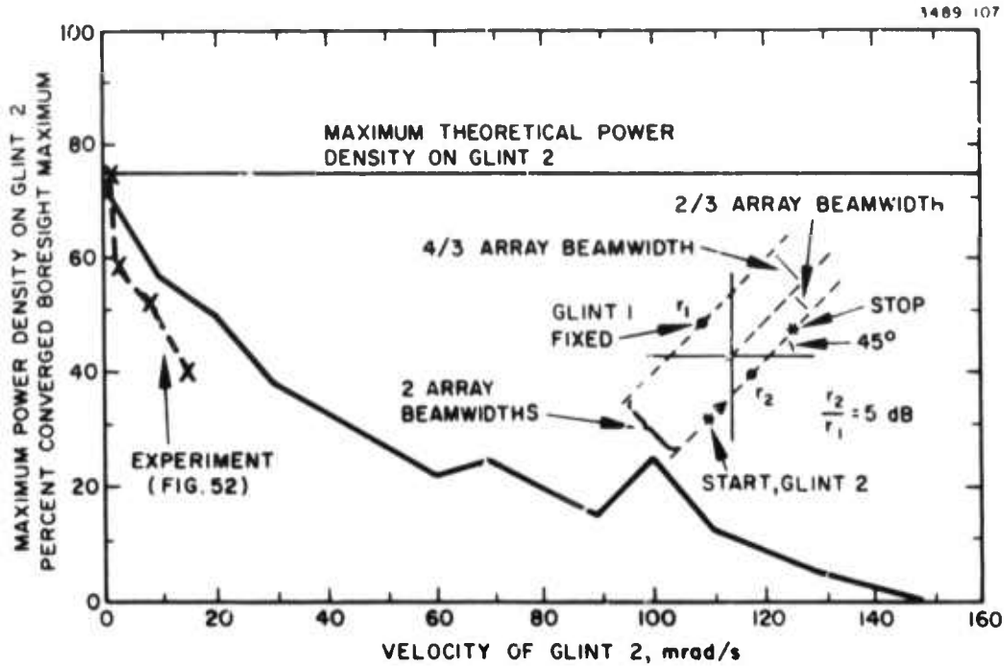

Fig. 60. Computer simulation results showing maximum power density on a moving glint for a different glint arragnement than in Fig. 59. The experimental points are plotted from the data shown in Fig. 52.

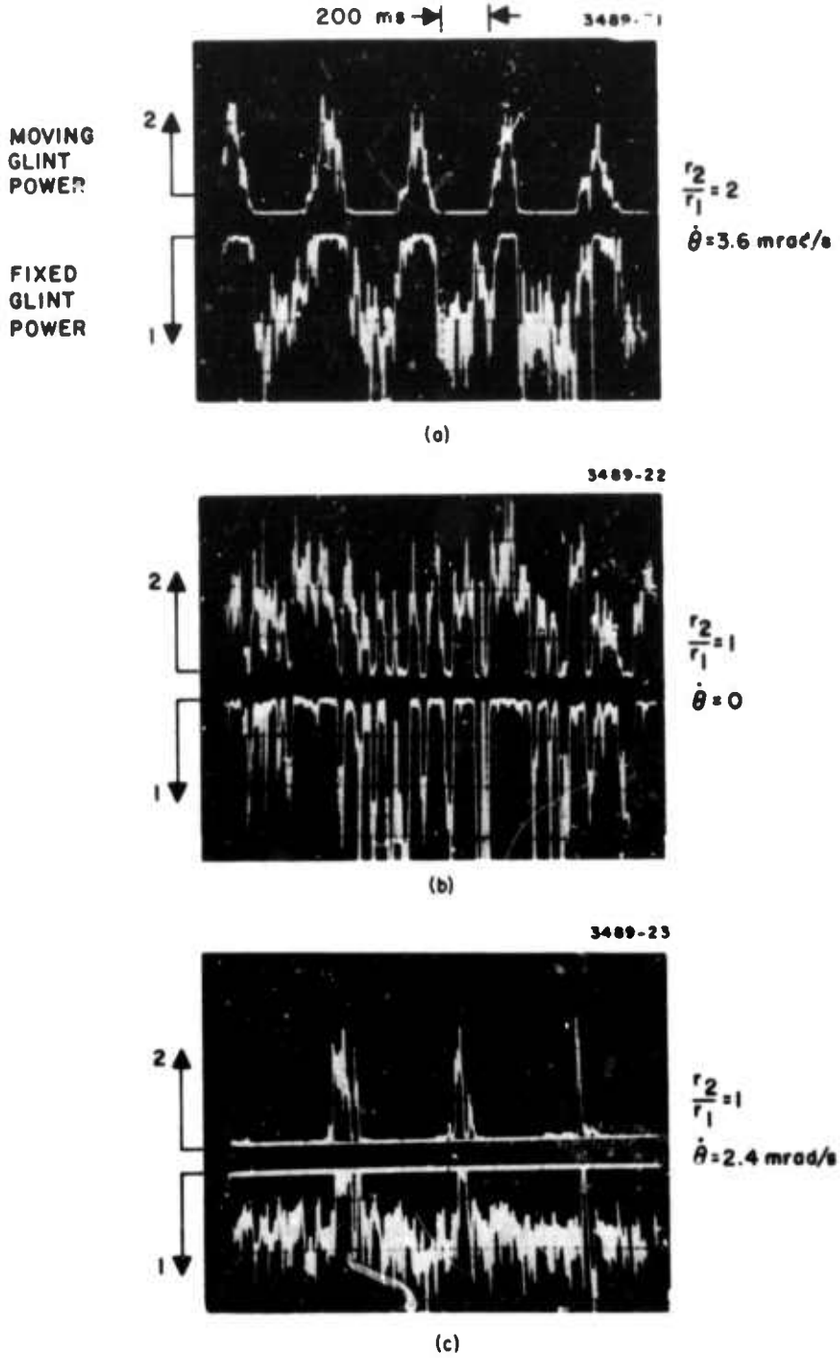

Fig. 61.
Power on each of two glints when one is stationary (1) and one is moving (2) at angular velocity $\dot{\theta}$. (a) Glint 2 is 3 dB stronger and moving at $\dot{\theta}$ = 3.6 mrad/s. (b) Equal glint reflectivities, $\dot{\theta}$ = 0. Glints at their closest approach. No power sharing is observed. (c) Equal glint reflectivities, $\dot{\theta}$ = 2.4 mrad/s. High turbulence. 27 June 1974. 1530 h. C_N^2(opt) = 3.0 x 10^{-14} $cm^{-2/3}$.

With the same conditions as used to produce Fig. 61(b), one glint is moved at 2.4 mrad/s to produce the data in Fig. 61(c). The preference for the moving glint is not as regular or as complete as in Fig. 61(a), but the power is always on only one glint as expected from the data in Fig. 61(b).

Cases with similar conditions to those in Fig. 61 have been run on the computer simulation using linear rather than elliptical glint motion. Figure 62 shows the observed result when the moving glint is twice as strong as the stationary glint. The beam initially converges on the stationary glint. As the stronger glint moves toward the center of the element pattern, there is actually some power sharing (t = 2 to t = 4 ms) and the power is not fully converged on the moving glint until t = 7 ms. Once the system converges on glint 2, it tracks it very well with the intensity variation following the element pattern intensity contour across the target plane.

As the moving glint 2 approaches the fixed glint 1 (t = 19 ms), the buildup of power on glint 1 is just the sidelobe power of the beam formed on glint 2. At t = 20.5 ms, the two glints are in the same position. As glint 2 moves further out, the beam remains locked on glint 1; the system has switched convergence from 2 to 1. We had initially expected the convergence and switching process to be more symmetric in time. That is, the buildup of power on glint 2 near t = 2 ms would be rapid and resemble a normal single glint convergence cycle as the system switched from glint 1 to glint 2. This is roughly the behavior seen near the end of the run from t = 19 ms to t = 21 ms. We have no adequate explanation for the much slower switching process in the early parts of the run, but once again we must be careful about trusting the details of the computer runs until the previously mentioned instability is corrected.

For comparison purposes, we have run the same test as in Fig. 62, but with the stationary glint having a 10 dB higher reflectivity. The power on the moving glint 2 in Fig. 63 thus traces out the sidelobe intensity contour when the beam is formed on glint 2. Comparing Figs. 62 and 63 near t = 4 ms illustrates the amount of power sharing. If the beam is fully formed on either glint, the other one would have only 5% of the boresight peak power density on it. At t = 4 ms in Fig. 62, both glints have 25% of the boresight peak, which is very close to the diffraction-limited value of 33% for an ideal array converged on glint 1.

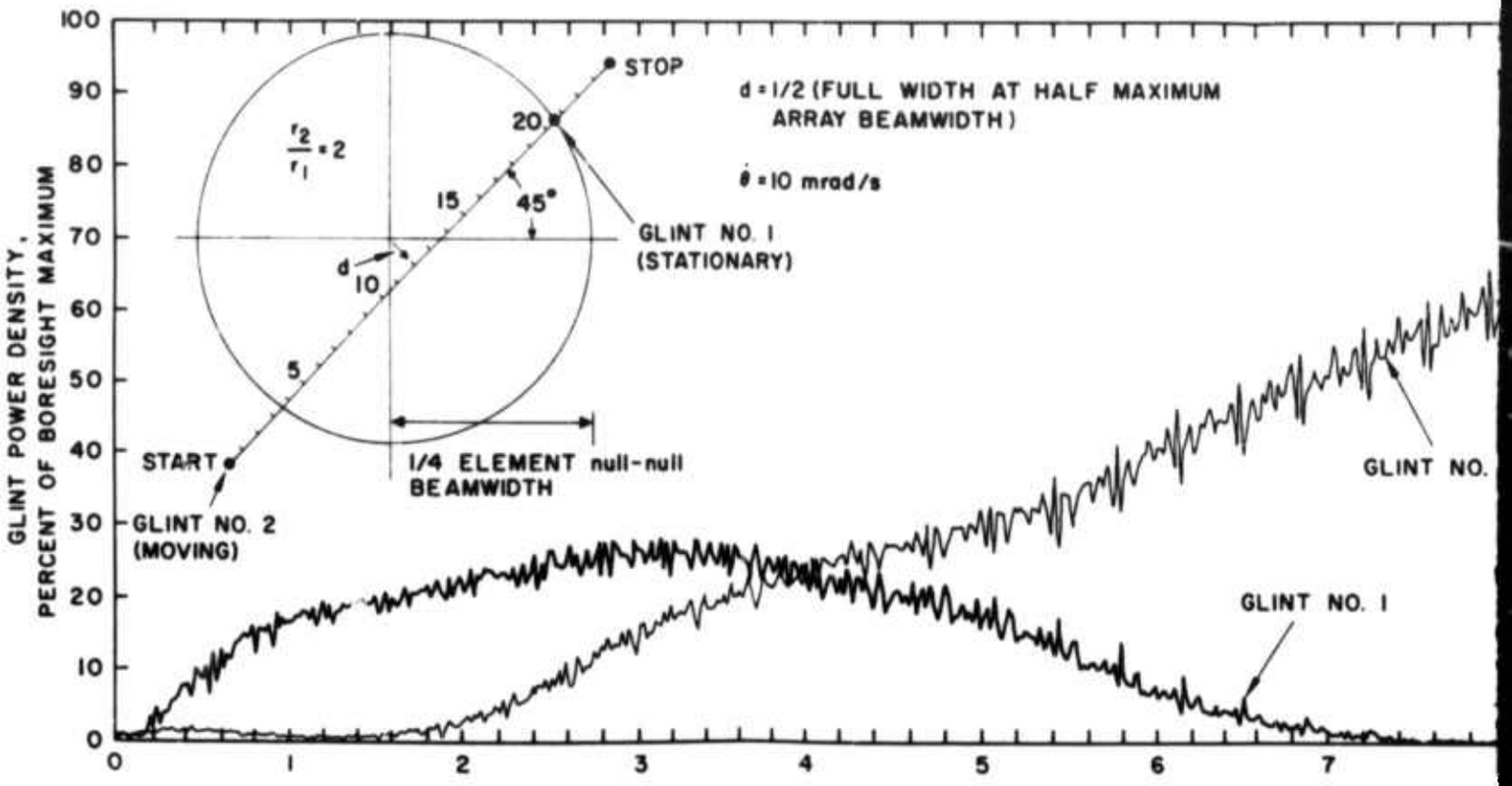

Fig. 62. Computer simulation of a stronger (3 dB) glint which
Notice the time scale change at 5 = 14.5 ms. The in
positions at different times.

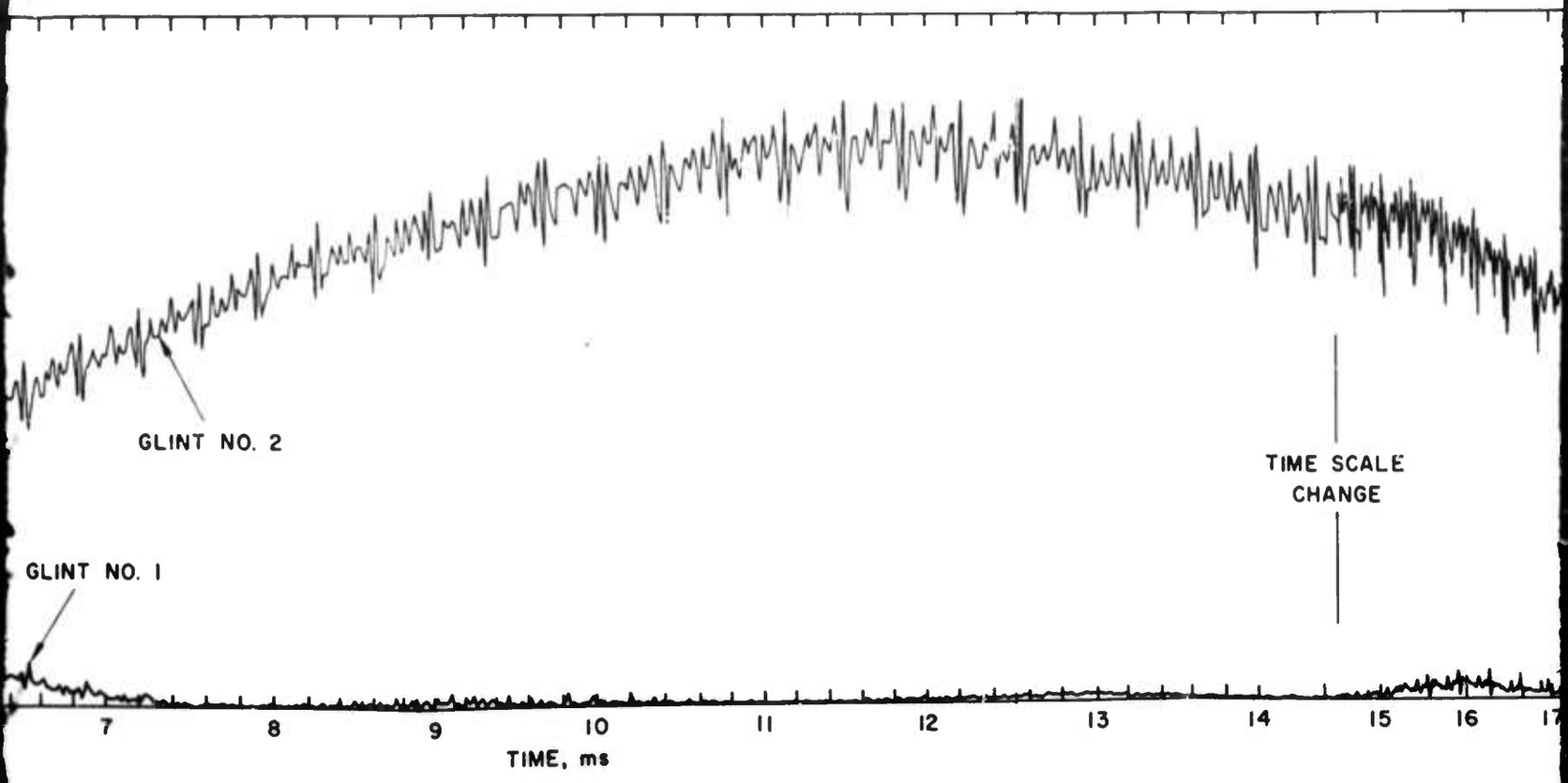

dB) glint which moves across a stationary glint.
14.5 ms. The inset shows the relative glint

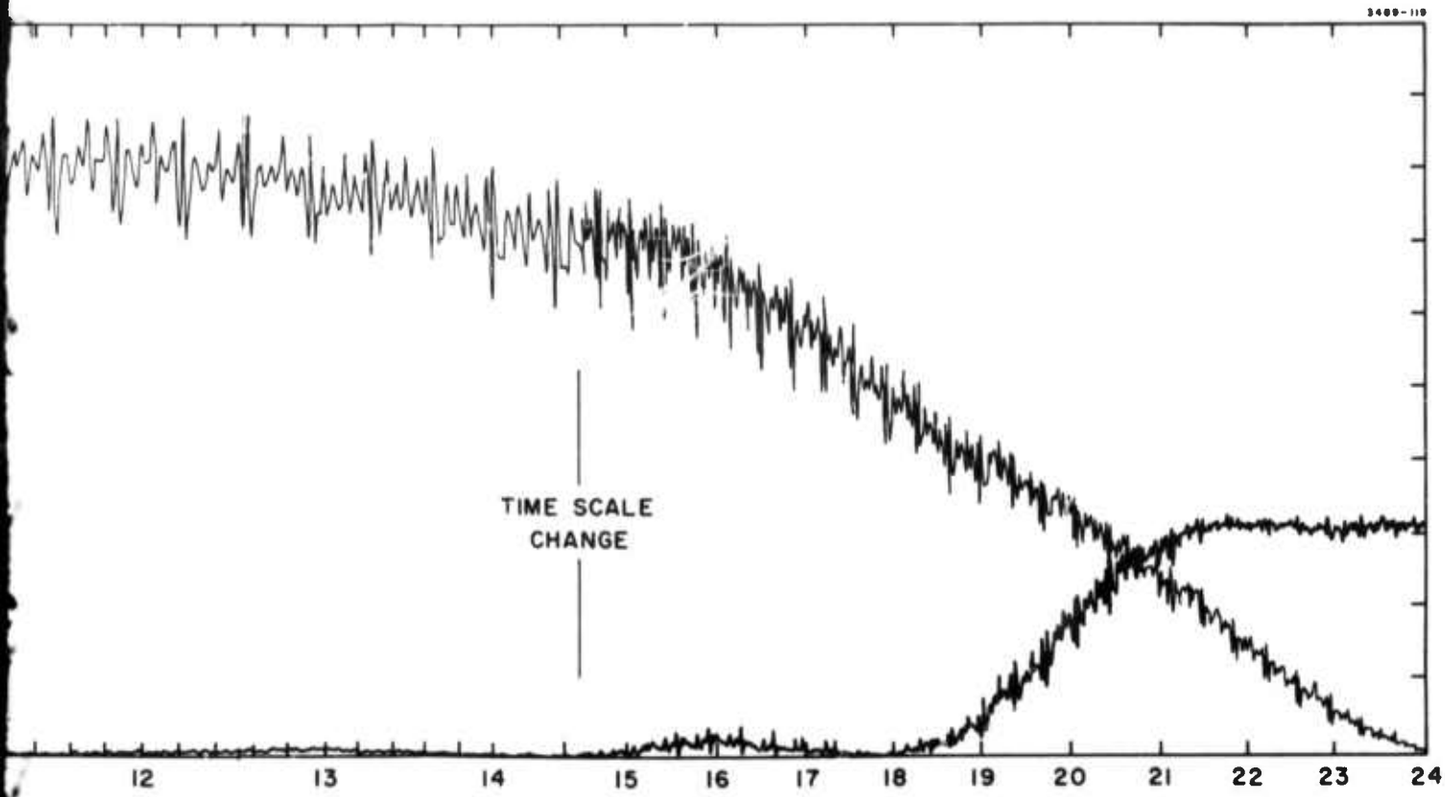
3469-119
TIME SCALE
CHANGE
12
13
14
15
16
17
18
19
20
21
22
23
24

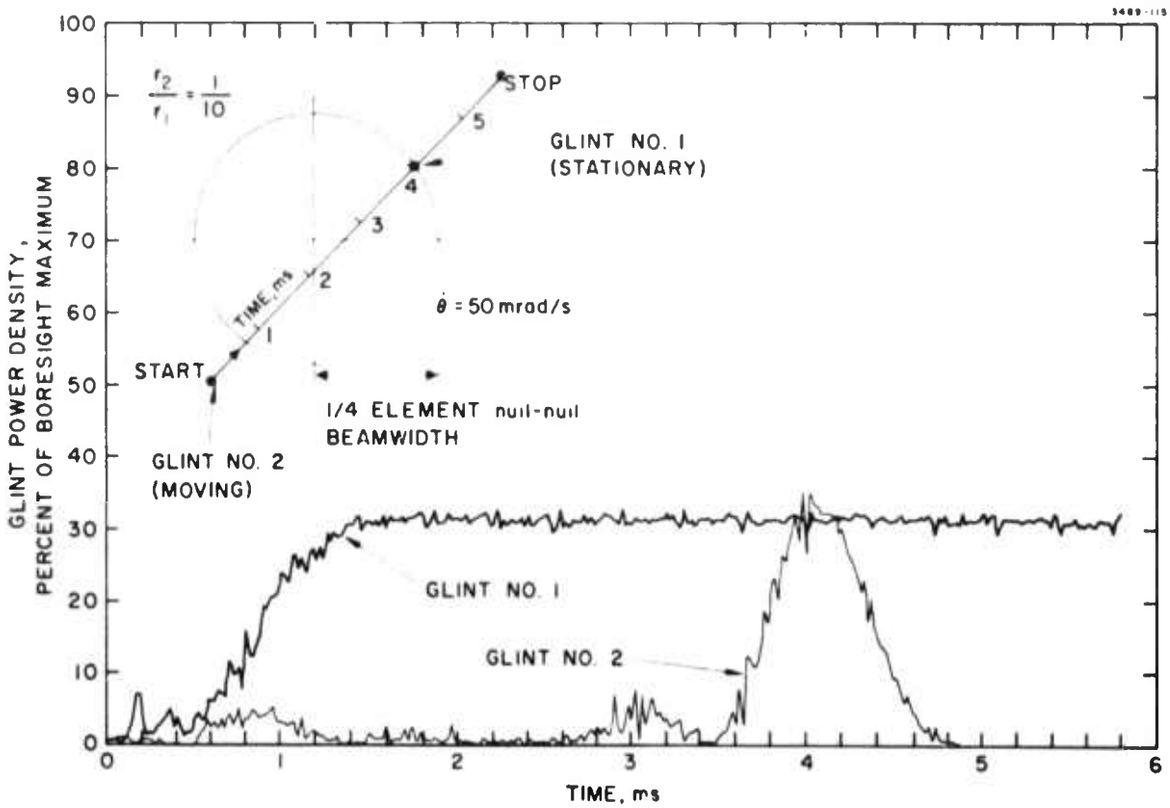

Fig. 63. Computer simulation of the power density on each of the two glints. The stationary gling 1 has a 10 dB higher reflectivity and the moving glint 2 passes through the stationary glint. The COAT-formed beam remains on glint 1 at all times.

Ignoring for the moment any errors in our simulation, this result says that the COAT system can on a temporary basis put a diffraction-limited power density on two widely separated points. This seems to be a contradiction in terms, but the key word is power density. The integrated total power through an aperture one beamwidth in diameter centered on each glint must be smaller (roughly one-half) than for a diffraction-limited beam formed completely on one glint.

If the two glints are made equal in reflectivity, the power sharing becomes even more pronounced. Figure 64 shows what happens in this case. Everything in the run is identical to the run in Fig. 62 except $R_2/R_1 = 1$ instead of 2. For times between 3.5 and 20.5 ms, the net reflectance of the moving glint 2 is larger than that of the stationary glint 1. The COAT system should thus converge the beam fully on glint 2. As can be seen, this does not occur until t = 13 ms, halfway through the run. From t = 16 ms to t = 24 ms, the power on each glint is identical to that shown in Fig. 62. This latter behavior we expected; the behavior up to t = 13 ms we did not expect and have no tested explanation for. As noted earlier, however, this unexpected behavior and power sharing may be a computational error in the simulation code.

Three conclusions from all the multiple glint studies are as follows: (1) The COAT system can distinguish between resolved glints, forming the beam on the strongest glint. The glints must differ by at least 3 dB for this discrimination to be reliable. (2) Under carefully adjusted and controlled conditions, the system can get confused in a sense, and tries to put power on more than one glint. There is always a definite convergence, however, and the glints must be very close in net reflectance for power sharing to occur. We do not feel this property would be a deficiency in a COAT system dealing with a real target having a complex, dynamic glint structure. In fact, the more readily observed behavior was power switching between equal glints rather than power sharing. (3) The behavior with one moving and one fixed glint is the same as with two fixed glints; the system locks onto and tracks the stronger glint, effectively ignoring the weaker one. These conclusions remain valid for both weak and strong turbulence.

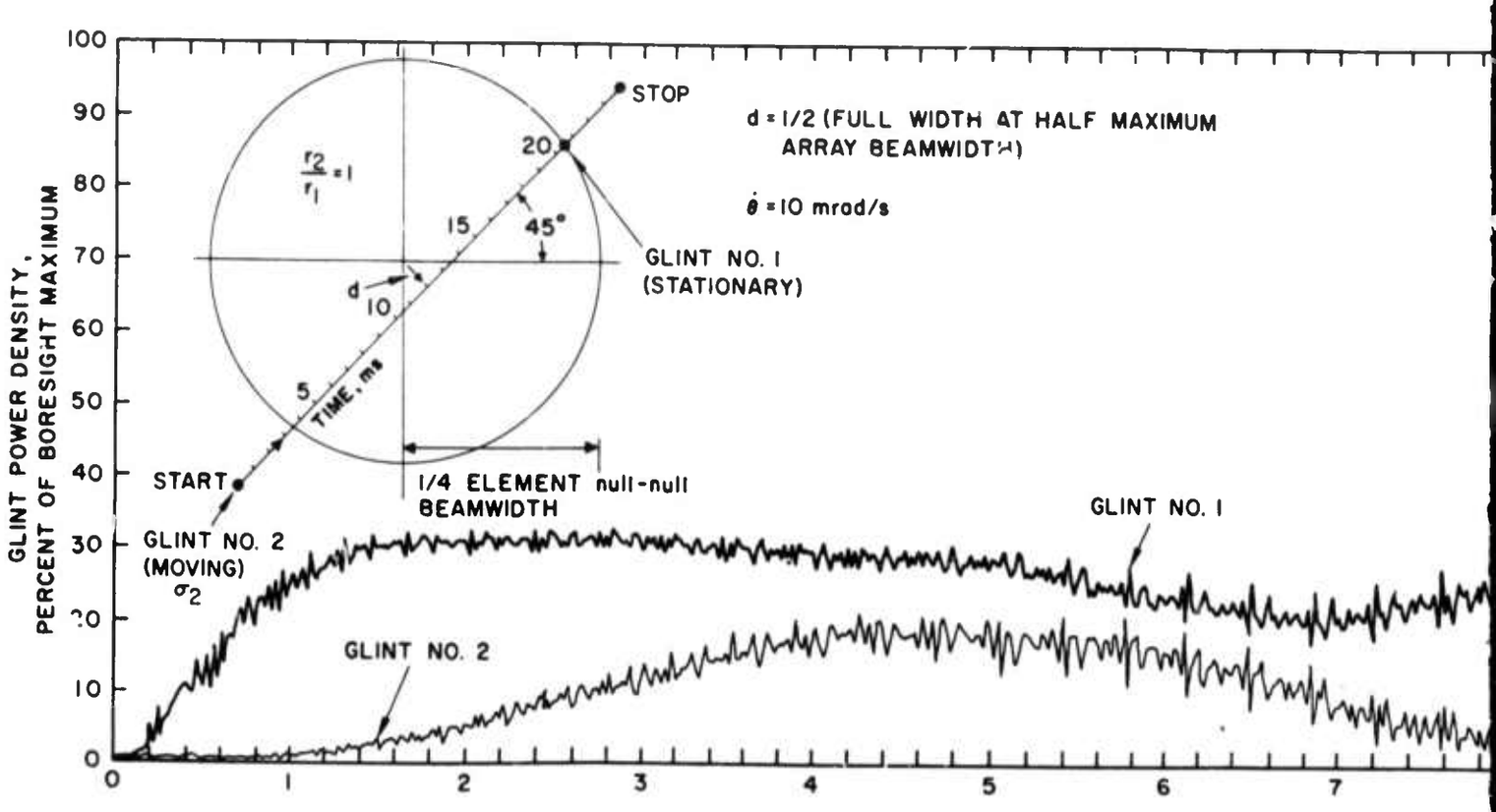

Fig. 64. Computer simulation run identical to that in Fig. 6 reflectivity: $r_2/r_1 = 1$. The time scale changes at sharing is evident for t < 13 ms.

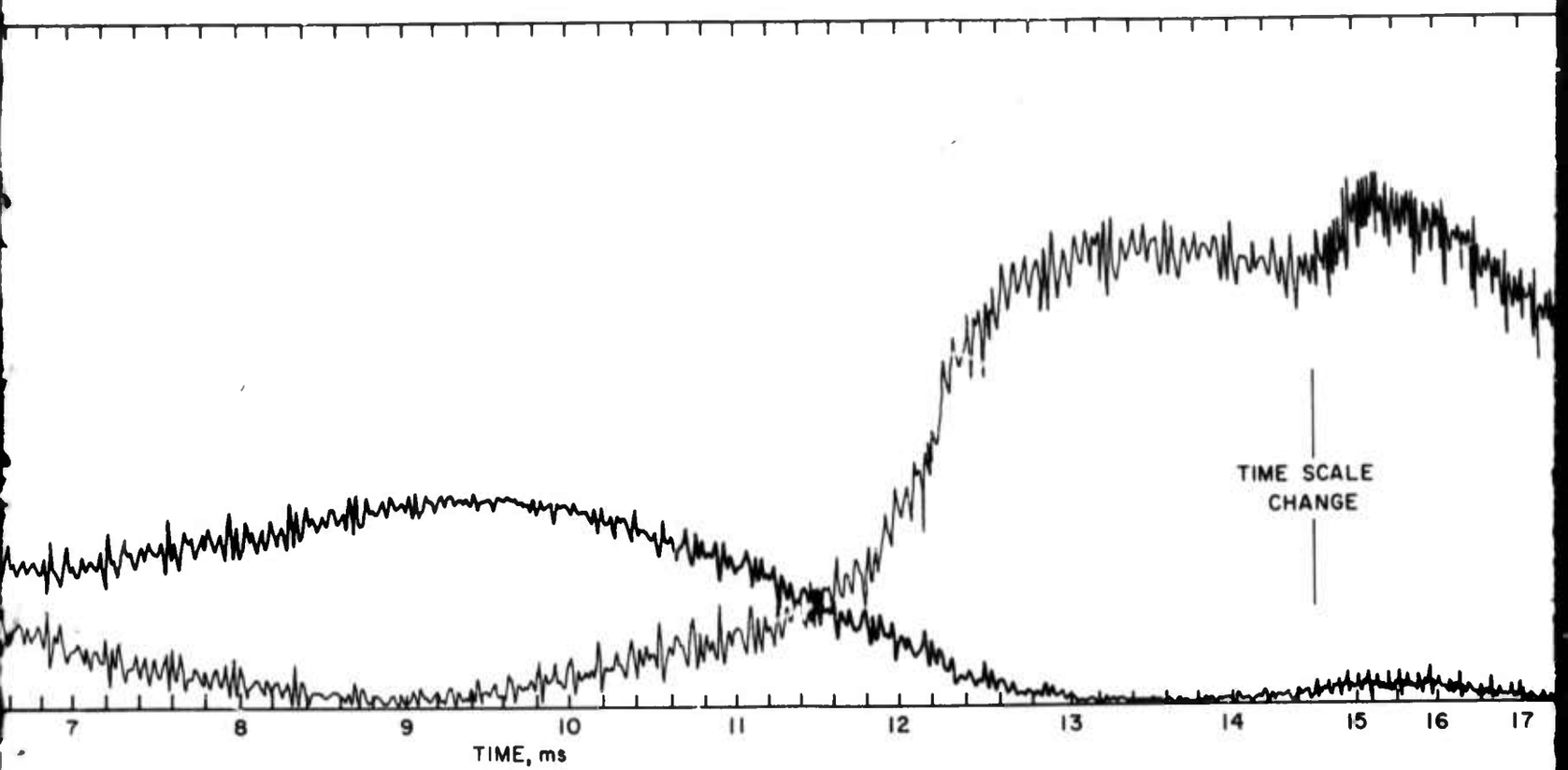

hat in Fig. 60 except the glints have equal
le changes at t = 14.5 ms. Significant power

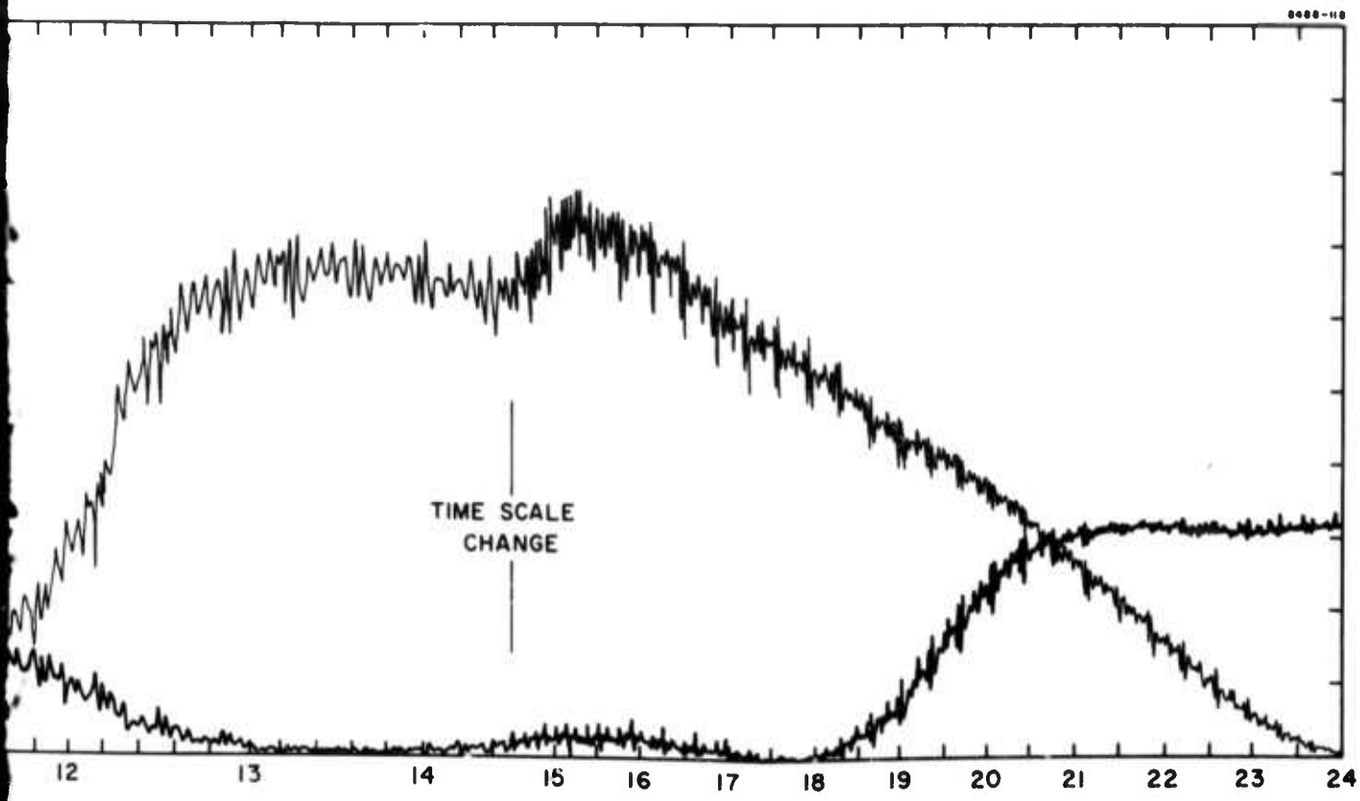
TIME SCALE
CHANGE
12
13
14
15
16
17
18
19
20
21
22
23
24

3. Complex Targets

Time on this contract did not permit extensive study of targets more complex than those discussed in the preceding sections. We did look at three targets, however, which presented a much more complex and less well defined glint structure. The first target was a large piece of scotchlite. When placed flat and perpendicular to the laser beam, this target acts like a diffuse scatterer with no clearly defined and resolved glints. As might be expected, the COAT system could not lock up on this target. When the scotchlite was curled slightly, however, to form a cylindrical surface not unlike the side of an aircraft, the COAT system could form the beam quite well even though the target was effectively a line glint.

The second target was a cats-eye glint placed in front of a large flat piece of scotchlite. This arrangement was used to measure what effect a large, bright diffuse reflector containing a very fine glint structure would have on convergence. The test showed that the system converges the beam on the cats-eye glint in an identical manner whether or not the scotchlite is present.

The third target used was an array of small retroreflector corner cubes resembling a bicycle reflector. The whole array was about as wide as an element null-null beamwidth at the target. The individual corner cubes are small enough that about three would fit across a formed array central lobe pattern. This target is thus a complex array of unresolved glints. One additional complicating feature of the target is a smooth, curved plastic cover which can act like the glint from a spherical surface. The COAT system was able to form the beam very well on this target, usually selecting two or three points to track and switch between as the retro array was moved across the beam.

For informational purposes, the relative returns from each of these targets is indicated by the photomultiplier signals shown in Fig. 65. As can be seen, the total peak return from the retro array is roughly equal to that of the single glint in front of the scotchlite. The scotchlite produced a signal at the receiver only one-tenth as large as the single cats-eye glint.

A true appreciation of this target can only be achieved by actually seeing it. We have photographed both the return from the array and the COAT-formed beam pattern as the array is moved. This sequence is in included in the movie which is an addendum to this report.

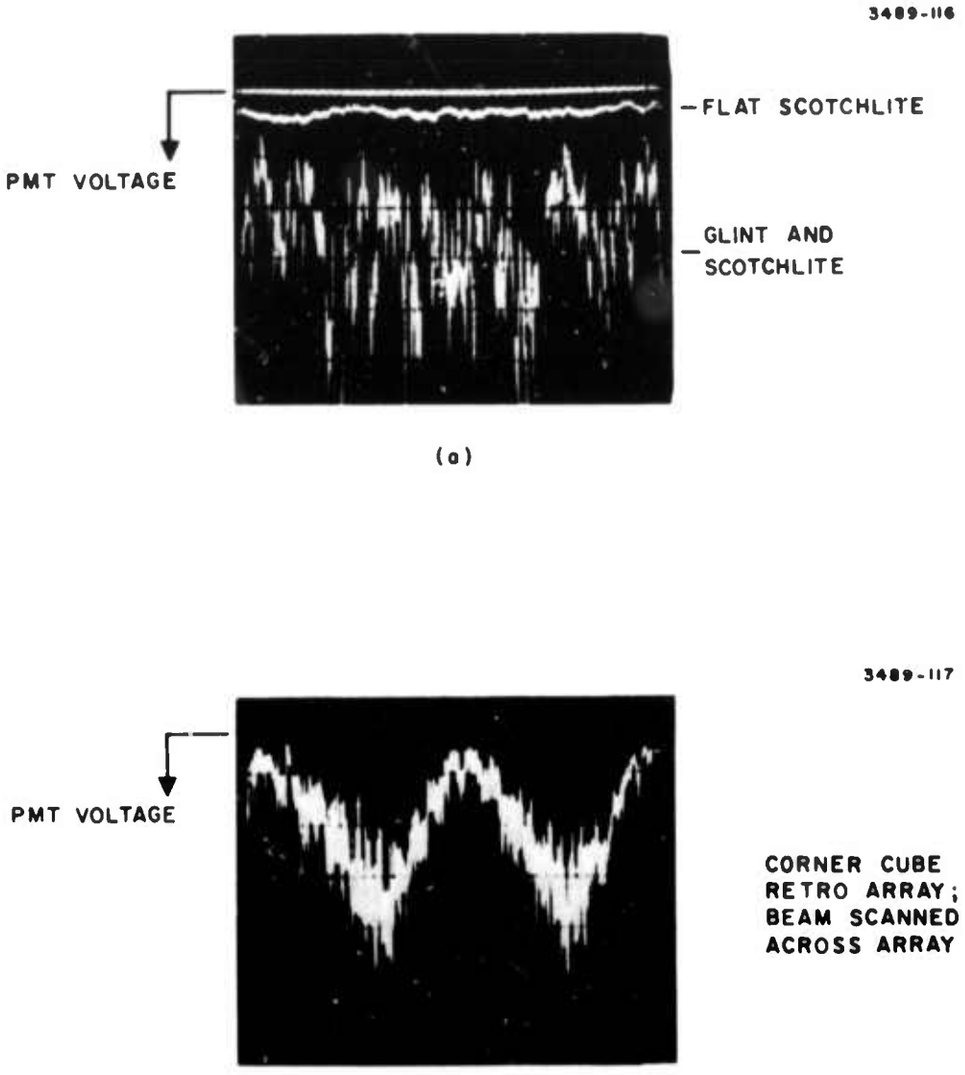

Fig. 65. Photomultiplier signals for three different targets. (a) Returns from flat scotchlite and from a single cats-eye glint in front of the scotchlite. (b) Return from an array of corner cubes as the COAT-formed laser beam is scanned periodically across it.

From these very brief tests, we may tentatively conclude that complex targets will not confuse this type of COAT system; it will select the brightest glint, form the beam on it, and track it. It is clear, however, that a more sophisticated type of glint discrimination is required for complex, moving targets if a beam is to be locked onto the target and held there without jumping from glint to glint as the glint pattern changes in time.

4. Offset-Pointing

The RADC/COAT system has two methods for offset pointing, mechanical using microslewing mirrors, and electronic using a pre-programmed phase scan. The mechanical scan has the advantage of being capable of large scan angles (many element beamwidths) but is relatively slow and subject to mechanical vibrations and bounce in the mirrors and drivers. The electronic scan is inherently fast and bounce-free but is limited to one-half an element peak-null beamwidth in order to avoid significant power loss due to grating lobe formation.

Both types of offset-pointing have been demonstrated in the laboratory[3] with a 6-element linear array and no turbulence. Near ideal performance was observed with both systems, indicating that the sample-and-hold circuitry is functioning properly. When using electronic offsetting, sample times as low as 2 to 4 ms (one convergence cycle) are adequate. The mechanical scan, however, requires a minimum sample time of 80 ms because of mirror bounce.

Attempts to demonstrate offset-pointing on the outdoor range have met with limited success. In high turbulence, the atmospheric dephasing time can become as short as 20 to 40 ms. In addition, the atmospheric correlation length for our range can get as small as 3 mm (see Fig. 21) so that the maximum offset angle is limited to about 2 to 3 array beamwidths* in high turbulence. This is no restriction for electronic scanning which is limited to 1/2 an array beamwidth, but does limit the mechanical offset.

The real limitation in the RADC/COAT system on mechanical offset-pointing in high turbulence is the required 80 ms sample time. If the

*The diffraction-limited null-to-null beamwidth at the target is defined as $1.2\,\lambda R/D_T$ where λ is the wavelength, R is the range, and D_T is the transmitter diameter.

hold (offset) time is set equal to one-half the atmospheric time constant, say 20 ms, only 20% of the total energy can be delivered to the offset point. If longer hold times are used, the beam will be severely degraded as we have shown in the previous report.[4]

The electronic scanning is thus the only feasible method in high turbulence as long as there are troubles with bounce in the microslewing mirrors. With a 4 ms sample time and a 20 ms hold time, 83% of the energy can be delivered to the offset point. Unfortunately, we have experienced some difficulty in programming and maintaining the proper offset signals for the 18-element system. The problem is caused by dc level drifts in the control channels which make it hard to properly set the offset voltage for each channel. There is no fundamental reason, however why electronic offsetting with the 18-element system in high turbulence should not perform as well as with the 6-element system in the laboratory.[3] Contract time limitations prevented us from remedying the voltage programming problem and demonstrating this conclusion.

D. Permanent Data Records

The data from the range measurements have been recorded in several forms. First, of course, there is the daily measurements log which includes system parameters and details of the measurements performed. Also included in this record are photographs of beam patterns and oscilloscope traces and spectral recordings made using a wave analyzer.

For later playback for display and analysis, we recorded the system performance on video tape and on a multichannel recorder (see Table IX). The video tape recordings contain the beam profiles as observed by the target monitor TV camera. A total data record of 180 min was recorded. The multichannel recorder records contain the data listed in Table IX for various turbulence conditions. Approximately 120 min of data were recorded in this manner.

Video and multichannel recorder records were not made during all measurements. Instead, representative data for single and multiple glint cases in high and low turbulence were recorded. These records have been further distilled and the most important and interesting video data transferred to movie film. These movies show much better than still photographs

how well the RADC/COAT system can compensate for atmospheric turbulence. Excerpts from these films have been shown as part of several papers[26-28] which have discussed various aspects of this work.

A 16 mm color movie is included as an addendum to this report. This movie is a compilation of all the important video data records. The movie was made by photographing a color monitor which is driven by the VP-8 image analyzer discussed in Section II-B of this report. A complete script is included with the film and Table X summarizes the sequences on the film.

TABLE X

Movie Sequences Included as Addendum to this Report

Single glint convergence, low turbulence: COAT-ON, COAT-OFF, no COAT correction
Single glint convergence, high turbulence: COAT-ON, COAT-OFF, no COAT correction
Tracking of a single moving glint, high turbulence
Tracking of a strong glint moving near a weaker glint, high turbulence
Convergence performance with a flat or a curved scotchlite sheet target
Convergence performance with a corner cube retro array target
Two displaced element patterns showing beam steering in high turbulence

IV. NONLINEAR GAS CELL DESIGN

In anticipation of a follow-on contract to this program which would deal with thermal blooming, the original statement of work was modified* to include the design of a nonlinear gas cell. The cell is to simulate forced-convection thermal blooming and will be used in conjunction with the RADC/COAT system in laboratory-scaled thermal blooming studies. This section presents the results of this design study.

A. Design Philosophy and Scaling Considerations

The ideal experiment to test how well a COAT system can compensate for blooming would be to employ a high power infrared, diffraction-limited source, a high power COAT system, and a 2 km or longer outdoor propagation path into which a controlled amount of absorbing gas could be introduced. None of these items is available, of course, but all the important parameters can be scaled so that a laboratory-size experiment using a visible wavelength can provide answers to many important questions about high power infrared systems. In addition, the use of a visible laser in a controlled laboratory environment greatly simplifies the instrumentation of the measurements and allows unexpected effects and system behavior to be observed first hand at the site and in real time.

For almost all atmospheric conditions of interest, heat transfer is dominated by convection rather than conduction. This fact is equivalent to the statement that negligible energy is lost by a gas molecule in the time required for the molecule to move across the optical beam. Mathematically, this condition can be written as

$$P_e = \frac{v\, r_o}{(K/\rho C_p)} >> 1 \quad . \tag{23}$$

The quantity P_e is called the "Peclet" number, v is the transverse wind velocity, and r_o is the beam radius. The thermal conductivity is K, ρ is the gas density, and C_p is the heat capacity at constant pressure. For a

*Change "A" dated 11 January 1974 to Contract F30602-73-C-0248.

given gas, eq. (23) sets a minimum value for the quantity vr_o.

In a medium of refractive index n, the wave equation for an optical field u can be written as

$$\left[i2k \frac{\partial}{\partial z} + \nabla_T^2 + k^2 (n^2 - 1)\right] u = 0 \quad , \tag{24}$$

where $k = 2\pi/\lambda$, z is the propagation direction, and ∇_T^2 is the Laplacian operator for the transverse coordinates. Blooming phenomena are produced by the $k^2(n^2 - 1)$ term; the larger this term, the greater the effect of blooming on the optical beam A convenient coordinate transfer involves the use of the dimensionless variables $\xi = z/L$ and $\underline{\zeta} = \underline{X}_t/r_o$ where L is the propagation path length and r_o is the beam radius. In these coordinates, eq. (24) becomes

$$\left[\frac{\partial}{\partial \xi} - \frac{i}{2} \frac{L}{kr_o^2} \nabla_\zeta^2 - \frac{ikL}{2} (n^2 - 1)\right] u = 0 \quad . \tag{25}$$

The quantity $(n^2 \cdot 1)$ in a gas at pressure p when eq. (23) is satisfied is found from the following expression:

$$\frac{kL}{2}\left[n^2(\xi,\zeta_1) - 1\right] = \frac{-\gamma_o(\gamma - 1)\, k\alpha L \exp(-\alpha L\xi) P_T}{\pi\gamma\, r_o\, v_p} \int_{-\infty}^{\zeta_1} \left|u(\zeta_1')\right|^2 d\zeta_1' \quad . \tag{26}$$

The total absorption along the path is αL, γ_o is the molecular polarizability, and γ is the specific heat ($\gamma = C_p/C_v$). The total optical power at $z = 0$ is P_T and cylindrical coordinates have been used. The integration coordinate is in the direction of the transverse wind velocity, v. By defining the quantities

$$a_L(\xi) = \frac{\gamma_o(\gamma - 1)\, k\alpha L \exp(-\alpha L\xi)}{\pi\gamma\, r_o\, v_p}$$

$$I(\zeta_1) = \int_{-\infty}^{\zeta_1} \left|u(\zeta_1')\right|^2 d\zeta_1' \tag{27}$$

we can write eq. (26) as

$$\frac{kL}{2}\,(n^2 - 1) = -\alpha_L(\xi)\, P_T I(\zeta_1) \quad . \tag{28}$$

Wavelength and power scaling can be achieved by maintaining $\alpha_L(\xi = 1) \cdot P_T$ constant, since $I(\zeta)$ involves only dimensionless variables. Table XI presents a scaling example comparing 10.6 μm propagation in the atmosphere to 0.488 μm propagation in a 50 cm cell filled with SF_6 and NO_2. The reasons for SF_6 and NO_2 are discussed in the following section. As can ben seen from Table XI, scaling to a 460 kW, 10.6 μm blooming experiment can be achieved within the laboratory using resonable experimental parameters.

A physical picture of the scaling requirements can be seen by noting that the scaling preserves the Fresnel number. Thus, the relative beam configuration and, hence the blooming effect as a function of path distance is preserved in the laboratory experiment. This is illustrated in Fig. 66 for the example given in Table XI.

TABLE XI

Example of the Scaling Between a 10.6 μm Atmospheric Blooming Experiment and a 0.488 μm Laboratory Gas Cell Experiment

Experiment Parameters	10.6 μm Atmospheric Experiment	0.488 μm SF_6 + NO_2 Experiment
Gas Pressure	1 atm	1 atm
α_L	0.5	0.5
L	2 km	50 cm
r_o	0.35 m	0.13 cm
v	10 m/s	3 cm/s
P_e (eq. 23)	2×10^5	12
α_L	2.66×10^{-5}	122
P_T	4.6×10^5 W	0.1 W
$\alpha_L P_T$	12.2	12.2

T1224

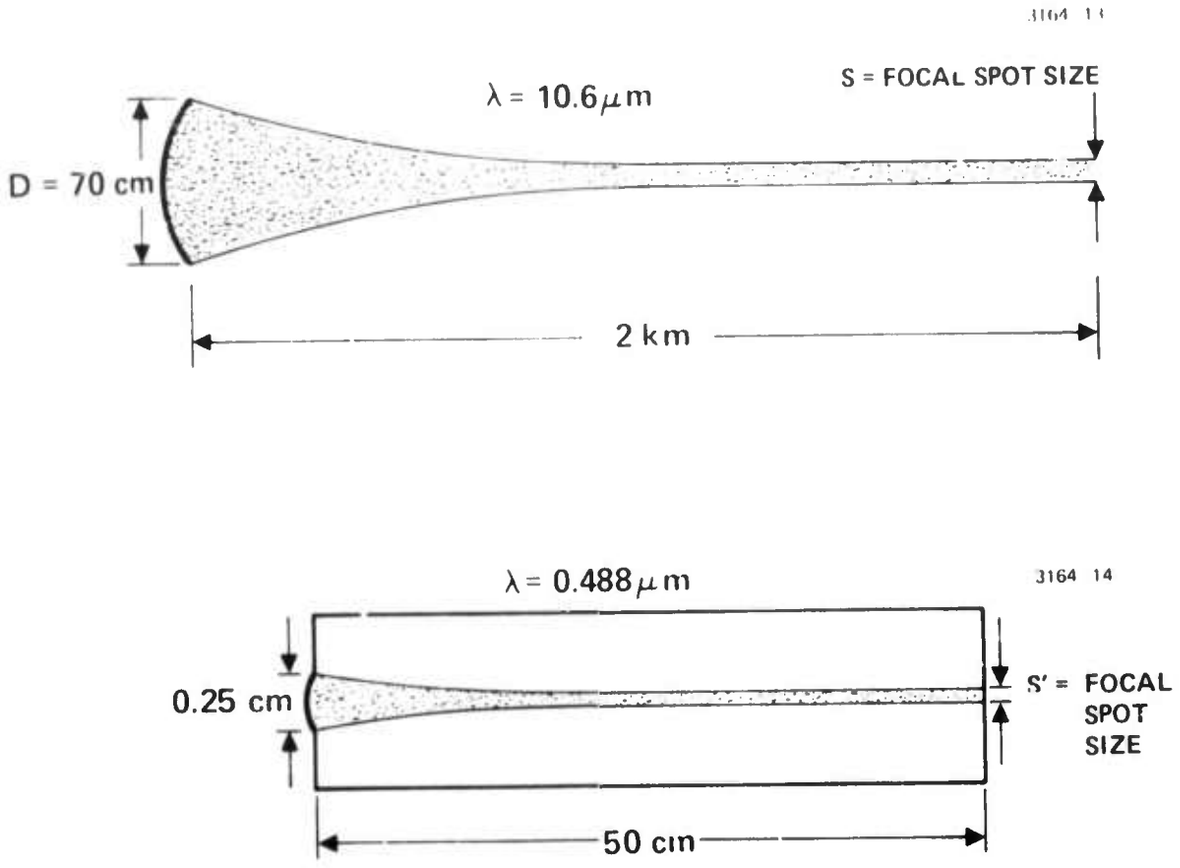

Fig. 66. Scaling example. By preserving the same Fresnel number F, the blooming effect as a function of path distance is preserved in the laboratory experiment.

B. Blooming Medium

Four requirements that determine the choice of a gas for blooming experiments are

1. Sufficient optical absorption at the desired wavelength
2. Maximum variation of index with respect to temperature, dn/dt, which is proportional to $\gamma - 1$ (see eq. (26))
3. Minimum thermal conductivity, K
4. Maximum gas density, ρ.

The last two requirements are equivalent to minimizing the diffusivity $D = K/\rho C_P$. Equations (23) and (26) can be combined to show that for a given gas

$$(n^2 - 1) \leq \frac{(\gamma - 1)}{pD\gamma} \times (\text{constant}) \tag{29}$$

where p is the pressure.

For a fixed pressure, a blooming "figure of merit" can be defined as

$$M = \frac{\gamma_o(\gamma - 1)}{D\gamma} \quad . \tag{30}$$

The larger the value of M, the greater the blooming at a given laser power. Note also that

$$\gamma_o \text{ and } \frac{1}{D} \propto \rho \propto p$$

so that for a given medium, the amount of blooming is proportional to pressure if the total absorption is constant.

The only readily available gases which have significant absorption at 0.488 μm are bromine, chlorine, and nitrogen dioxide (NO_2). Of these three, NO_2 has the strongest absorption, and so less of it is required for a desired attenuation. Unfortunately, none of these three gases is desirable for fulfilling the other three requirements listed above. Consequently, a second gas must be chosen which fulfills requirements 2 through 4 and NO_2

can be used for optical absorption. The actual blooming is then done by this second or buffer gas after the NO_2 transfers its absorbed energy to it.

The best candidates for a buffer gas are sulfur hexafluoride (SF_6), xenon, CO_2, argon, and nitrogen (N_2), in that order. Table XII lists the important properties of these gases and of NO_2 along with the figure of merit, M, computed for a total pressure of 1 atm. Sulfur hexafluoride is the best gas for maximum blooming, being 1.2 times as effective as xenon, and 4.8 times as effective as CO_2 in producing blooming. Although xenon is comparable to SF_6 in producing blooming, the much lower cost of SF_6 makes it the logical choice.

When using one gas to accomplish the absorption and another to perform the blooming, the relaxation rate of the absorbing gas must be considered. The absorbing gas, NO_2, must transfer most of its added energy to the buffer gas in a time small compared with the time required for an NO_2 molecule to move out of the optical beam and before the energy is lost by spontaneous emission (fluorescence). The absorption of 0.488 μm light in NO_2 involves a transition from the molecular ground state into the first electronic state, about seven vibrational levels from the bottom of the band.[29]

TABLE XII

Gas Properties Important in Producing Thermal Blooming

Property / Gas	$Y_o \approx 2(\alpha - 1)$	D, cm^2/s	α Absorption Coefficient at 0.488 μm	Gamma	$M \times 10^4$ (eq. (30))
SF_6	1.54×10^{-3}	0.032	Negligible	1.33	119
Xe	1.42×10^{-3}	0.054	Negligible	1.66	103
CO_2	9×10^{-4}	0.086	Negligible	1.31	25
Ar	5.6×10^{-4}	0.188	Negligible	1.67	12
N_2	5.9×10^{-4}	0.187	Negligible	1.40	9
NO_2 (absorber only)	—	—	$0.01\ cm^{-1}$ at a partial pressure of 4 Torr	—	—

T1463

The most recent measurement[30] of the collisionless lifetime of the first electronic state is 44 μs and the lifetime for a transition between vibrational levels in the same band is even longer. With 1 atm of another gas present, say SF_6, the collisional deactivation rate is roughly $1.4 \times 10^{+9}$ s^{-1}. A general rule of thumb is that 10^3 collisions are required to cause a molecule-like NO_2 to relax one vibrational level in a vibrational-translational (V-T) transition. With roughly 21 V-T levels from the initial absorption level to the ground state, the NO_2 will completely transfer its energy to the SF_6 in 15 μs with only 0.7 μs between V-T level changes (NO_2 molecules can make a radiationless transition from the first electronic state to an excited vibrational level of the ground state[31]). When compared with the time for a molecule to cross the beam because of "wind" (about 30 ms), the transfer of energy from NO_2 to SF_6 is effectively instantaneous. In addition, the long collisionless lifetime and high deactivation rate ensures negligible energy loss by fluorescence. The same conclusions also apply when xenon, CO_2, argon, or nitrogen is used as the buffer gas.[32]

C. Cell Design

1. Wind Generation

Several designs[33] have been evaluated for producing the transverse wind required for convection-dominated blooming. The design we have chosen is shown schematically in Fig. 67. The design is a variant of those which employ a stationary cell and use beam motion to stimulate a transverse wind. Only one moving mirror is used, but four stationary mirrors are placed so that the beam is brought to the back side of the moving mirror. With this arrangement, the output beam remains stationary, greatly simplifying the beam diagnostics. The solid and dashed beam paths in Fig. 67 correspond to the mirror positions labeled 1 and 2, respectively.

The two lenses labeled f_1 and f_2 in Fig. 67 have the same focal length. Lens f_1 focuses the collimated input beam through the cell with the focal point occurring near the output window of the gas cell. Lens f_2 then reimages this focal point at infinity (recollimates the beam). Additional optics are required at the input to f_1 to ensure proper scaling of the beam Fresnel number at the cell input and at the output of f_1 to obtain the far field of the beam within the laboratory (in effect, reimaging and magnifying the focal plane of f_1 which is also the effective glint target plane).

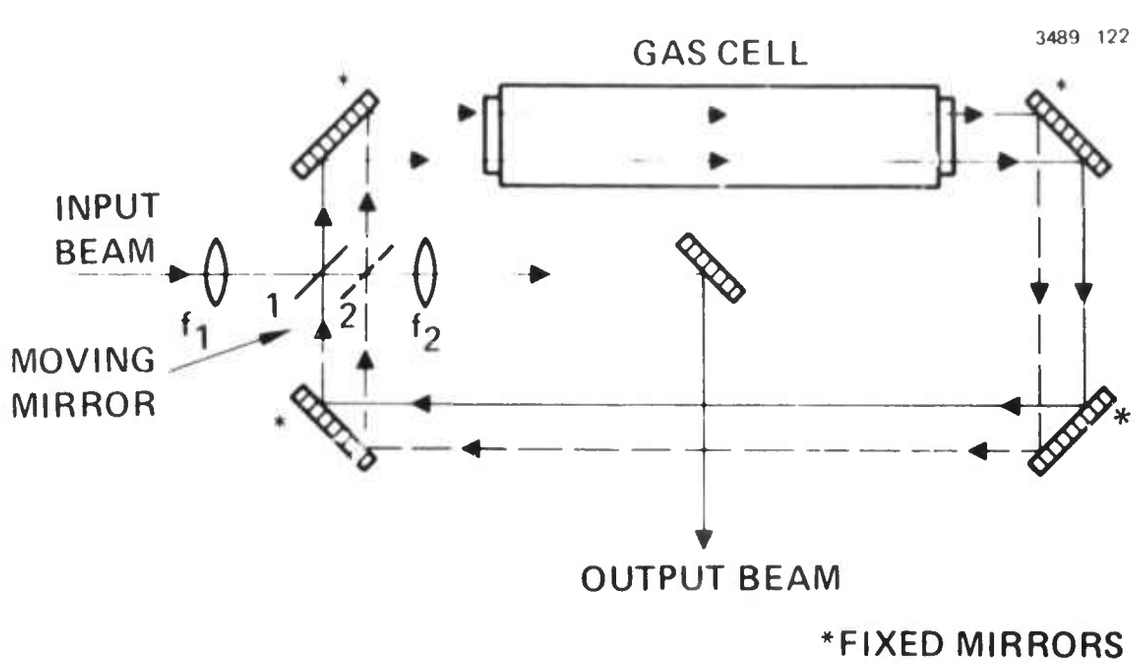

Fig. 67. "Wind generation apparatus. The moving mirror causes the input beam to move relative to the gas cell. The fixed mirrors bring the moving beam to the back of the moving mirror so that the output beam is stationary.

This method of wind generation was chosen for three reasons. First, it is very simple and requires moving only one small mirror. Second, the output beam appears stationary, just as it would if the gas were moved across a stationary beam. Finally, the gas cell construction is very simple. The design has two disadvantages, however. The most important is that the focal plane moves relative to the cell. This should present no serious problems in interpreting the results, however, as long as the focal plane remains inside the cell. The second drawback of this design is the periodic nature of the "wind." The moving mirror is driven sinusoidally and so the wind direction reverses periodically. Also because of the sinusoidal mirror motion, only about one-third of the total excursion can be used if the wind velocity is to be held constant. This feature of the design is only a cosmetic deficiency, however, and in no way complicates either the instrumentation or the interpretation of the data.

2. Gas Cell Design

There are two overriding considerations in the design of the blooming cell. First, it must be able to hold a reasonable vacuum of about 0.1 Torr so that fill gases can be accurately metered into it. Second, it must be able to withstand the corrosive nature of NO_2. Since the "wind" generation is accomplished by external means, both of these requirements are easily met by a stainless steel cylinder with glass windows on each end. The design is shown schematically in Fig. 68. The 50 cm cell length was chosen for convenience: long enough so large f-number lenses can be used and short enough to be convenient in the available laboratory space.

Since NO_2 is highly toxic as well as corrosive it is metered into the cell through a precision needle valve. A second needle valve at the NO_2 gas bottle is used to restrict the flow rate in the event of leaks or a line breakage. For safety reasons, the line from the NO_2 bottle to the cell is kept as short as possible and the main valve on the NO_2 bottle is closed at all times except during a fill cycle.

As indicated in Fig. 68, two vacuum gauges are used. Since a pressure of only 4 Torr of NO_2 is required for 50% absorption along a 50 cm path,[33] a precision differential vacuum gauge is used to monitor the introduction of precise and reproducible amounts of NO_2. A coarse pressure

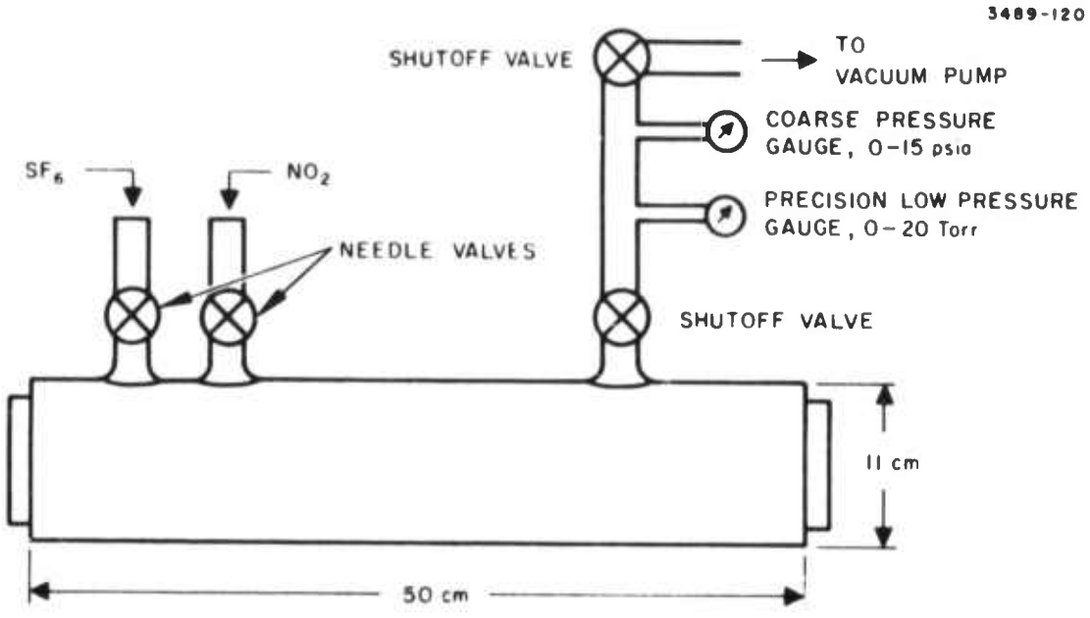

(a)

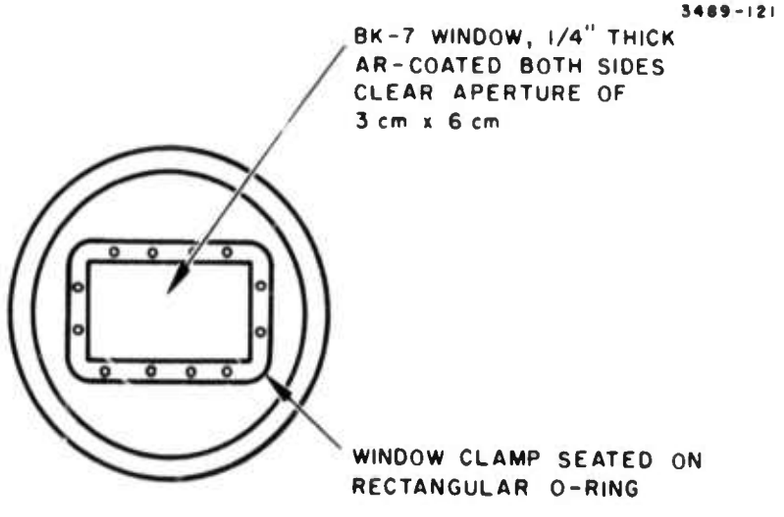

(b)

Fig. 68. Gas cell schematic diagram. (a) Side view showing inlet and outlet ports, valves and pressure gauges. (b) End view showing glass window mount.

gauge is then monitored as SF_6 is put into the cell up to a pressure of 760 Torr (1 atmosphere). When the cell is filled, it is closed off and the gauges pumped out to prevent corrosion by the NO_2.

All of the parts and materials have been ordered for the cell, for the gas and vacuum handling station, and for the moving mirror. Because of the simplicity of the design, no serious obstacles are foreseen in the construction and implementation of this thermal blooming simulator. We plan to use the cell in a horizontal configuration, assuming that the low total power absorption (50 mW or less) and the moving beam will prevent formation of convection currents. If convection currents do cause problems, the cell can be mounted vertically without too much additional hardware.

V. CONCLUSIONS

The performance data from this program and the conclusions drawn from the data are contained in previous sections of this report. The impact of these studies on the design of high power COAT systems and components is part of the addendum proprietary document which addresses "Task III" of the contract. This section summarizes the conclusions about multidither COAT systems and their performance in turbulence compensation which can be drawn from the work performed on this contract. Our conclusions are presented below.

Multidither COAT Turbulence Compensation

- A multidither COAT system can produce a nearly diffraction-limited beam even for beams propagating through very strong atmospheric turbulence. Residual errors in the optical system are also removed without affecting the turbulence compensation performance. An 18-element, 15 mm diameter transmitter proved sufficient for the turbulence levels encountered on a 100 m range with a 0.488 μm optical wavelength. A larger number of elements may be required for larger transmitter diameters, larger ranges, or higher turbulence levels at other wavelengths. The minimum number of COAT servo channels depends on all these parameters.

- The servo electronics for a multidither COAT system are relatively simple and compact and can be constructed using all solid-state off-the-shelf components.

- A correction bandwidth of 50 Hz is sufficient for atmospheric turbulence compensation with static targets. Bandwidths up to the 500 Hz limit of the RADC/COAT system will be necessary for moving targets and slewing beams and if a 2 ms convergence time is required.

- Peak-to-peak phase errors on the order of 1.3 wavelengths are present in strong turbulence for a 15 mm diameter beam transmitted across a 100 m path. A total phase correction capability in a COAT system of ±1 wavelength is thus sufficient for turbulence compensation. A larger dynamic range of about ±2 wavelengths is desirable, however, to allow for offset errors in the electronics and to allow electronic offset-pointing without

exceeding the maximum allowable phase excursion of the system.

- Turbulence correction performance is not degraded by moving, multiple glint targets. A multidither COAT system will select and lock onto the strongest glint in a multiglint target. Glint discrimination is perfect if one glint has at least 2 to 3 dB larger return than any other single glint. The presence of a large diffuse target has no effect on system performance as long as the target also contains a brightest glint.

- Moving targets can be tracked by a 500 Hz servo bandwidth COAT system at rates exceeding 10 mrad/s. More rapidly moving targets can also be tracked, but the peak power density on the target is reduced. Servo system bandwidths in excess of 500 Hz will be required for faster electronic tracking and slewing performance. Tracking performance is not affected by a multiple glint target; the COAT system will converge on and track the strongest glint.

- Adaptive xy-pointing control is desirable to remove atmospheric beam steering which cannot be removed by transmitter phase control. This type of active control can be implemented using a dithered servo system similar to the phase control system in the RADC/COAT system. The control loop can be closed around the target utilizing the same intensity detector used for the phase control loops.

- Offset-pointing is straightforward to implement with this type of COAT system using sample-and-hold circuitry in the servo electronics. Pointing can be done either mechanically with microslewing mirrors or electronically using preprogrammed phase control of the transmit aperture. When a sample-and-hold technique is used, secondary glints in the beam offset region of the target are ignored by the COAT system.

- The measurements in this program were performed using a 0.488 μm laser wavelength. The transmitter diameter, range, and turbulence levels used, however, are scalable to interesting scenarios at 10.6 μm and 3.8 μm wavelengths. All of the conclusions based on these visible wavelength studies will thus also apply to multidither COAT turbulence compensation at 10.6 μm or 3.8 μm laser wavelengths.

VI. RECOMMENDATIONS FOR FUTURE WORK

The work on this contract has demonstrated that multidither COAT can correct for beam distortions caused by atmospheric turublence. A DARPA/RADC follow-on contract (No. F30602-75-C-0001) is designed to investigate COAT compensation for thermal blooming distortions. Both of these contracts will also produce design guidelines for high power laser COAT systems. When taken together, this contract and the follow-on to it will demonstrate by experiment and analysis (1) whether a multidither COAT system can simultaneously correct for optical system distortions, thermal blooming, and turbulence, (2) how well a given COAT system can compensate for various types and strengths of distortions, (3) what effects, if any, certain target glint structures have on the operation of a COAT system, and (4) what the design tradeoffs are for implementing a COAT system on a high power laser.

With this rather complete data base, additional desirable investigations fall into three broad areas: (1) high power component development, (2) advanced system concepts demonstration, and (3) high power system demonstration. In the area of high power components, there are several key components which need further development. These include cooled deformable mirror surfaces which have the necessary resonance-free frequency response characteristics, actuators for these mirrors, and cooled high efficiency diffraction gratings.

A multidither COAT system requires two types of deformable mirrors (or the acousto-optic or electro-optic equivalents). One high amplitude, relatively low frequency response unit for the phase error correction and the second is a low amplitude, high frequency device for generating the dither modulations. With current designs, two separate units are best employed to perform these functions. Recent tests of Hughes cooled mirror designs indicate both types of mirror faceplates can be built.

The IR&D program at the Research Laboratories has recently produced some novel mirror actuator designs which appear very promising for driving both the corrector and dither mirrors. Contract support is recommended to continue this development effort and, in particular, to combine the

new actuator designs with a deformable faceplate to obtain a wide bandwidth, continuous surface dither mirror with 50 or more actuators which will be suitable for high power applications.

Several advanced COAT system concepts, many of which are Hughes proprietary, may offer certain advantages for particular applications. These possible advantages include reduced deformable mirror requirements, reduced mirror actuator requirements, reduced number of mirror actuators, and improved target tracking and glint discrimination. Almost all of the advanced concepts can best be tested and verified under controlled laboratory conditions. Developmental programs should be undertaken to identify any relative advantages of these concepts. In addition, many questions remain unanswered about the interaction between a COAT system and a real moving target with a complex dyramic glint structure. A laboratory-scaled experimental program to investigate these target effects in depth may be required after the initial studies that will be carried out under the DARPA/RADC follow-on contract.

With the successful demonstration of compensation for turbulence and optical system distortions and the anticipated reduction of thermal blooming, there is little remaining doubt that a COAT system can provide significant improvement in target power density. Since the high power component development is also in a reasonably advanced state, it appears to be a propitious time to commit funds to a full high power COAT demonstration. The proof of the usefulness of a COAT system will not occur until a demonstration is made on a high power laser such as the XLD-2. The high level of confidence in multidither COAT operation and the state of component development indicate minimal risk in proceeding at the earliest date toward a high power COAT demonstration.

REFERENCES

1. W. B. Bridges, et al., "Coherent Optical Adaptive Techniques (COAT)," Contract F30602-73-C-0248, Technical Report No. 1. (AD772 639)
2. W. B. Bridges, et al., "Coherent Optical Adaptive Techniques (COAT)," Contract F30602-73-C-0248, Technical Report No. 2. (AD776 814)
3. W. B. Bridges, et al., "Coherent Optical Adaptive Techniques (COAT)," Contract F30602-73-C-0248, Technical Report No. 3. (AD779 668)
4. W. B. Bridges, et al., "Coherent Optical Adaptive Techniques (COAT)," Contract F30602-73-C-0248, Technical Report No. 4. (AD783 281)
5. M. R. Spiegel, Statistics, Schaum's Outline Series (McGraw-Hill, New York, 1961).
6. S. Hansen, "Optical Phase Shifter," Hughes Patent Docket No. 074010 (1974).
7. G. R. Ochs, "A Resistance Thermometer for Measurement of Rapid Air Temperature Fluctuations," ESSA Technical Report IER47-ITSA 46 (U.S. Dept. of Commerce, Washington, D. C., October 1967).
8. D. L. Fried, J. Opt. Soc. Am. 57, 175 (1967).
9. N. I. Tatarski, Wave Propagation in a Turbulent Medium (McGraw-Hill, New York, 1961).
10. A. Kolmogorov, in Turbulence, Classical Papers on Statistical Theory, S. K. Friedlander and L. Topper eds. (Interscience, New York, 1961).
11. P. M. Livingston, Appl. Opt. 11, 684 (1972).
12. G. R. Ochs, R. R. Bergman, and J. R. Snyder, J. Opt. Soc. Am. 59, 231 (1969).
13. D. L. Fried and J. B. Seidman, J. Opt. Soc. Am. 57, 181 (1967).
14. J. A. Dowling and P. M. Livingston, J. Opt. Soc. Am. 63, 846 (1973).
15. G. E. Mevers, M. P. Keister, Jr., and D. L. Fried, J. Opt. Soc. Am. 59, 491 (1969).
16. J. R. Kerr, J. Opt. Soc. Am. 62, 1040 (1972).
17. J. R. Dunphy and J. R. Kerr, J. Opt. Soc. Am. 63, 981 (1973).
18. D. L. Fried, J. Opt. Soc. Am. 55, 1427 (1965).

19. D.L. Fried J. Opt. Soc. Am. 56, 1372 (1966).

20. "COAT Planar Array," Technical Proposal 73M-3186/C8902, Hughes Research Laboratories, January 1973.

21. D.M. Chase, J. Opt. Soc. Am. 56, 33 (1966).

22. W.P. Brown, unpublished.

23. G.W. Reinhardt and S.A. Collins, Jr., J. Opt. Soc. Am. 62, 1526 (1972).

24. A.J. Huber, "Measurements of the Temporal Power Spectra of a Propagating 10.6 Micron Wave Front," RADC Report No. RADC-TR-74-44, February 1974. (AD777 259)

25. R.L. Fante, J. Cpt. Soc. Am. 56, 33 (1966).

26. W.B. Bridges, S. Hansen, L.S. Horwitz, S.P. Lazzara, T.R. O'Meara, J.E. Pearson, and T.J. Walsh, "Coherent Optical Adaptive Techniques," J. Opt. Soc. Am. 64, 541 (1974), abstract only.

27. J.E. Pearson, W.B. Bridges, L.S. Horwitz, T.J. Walsh, and R.F. Ogrodnik, "Atmospheric Turbulence Compensation Using Coherent Optical Adaptive Techniques," presented at the OSA Topical Meeting on Optical Propagation Through Turbulence, Boulder, Colorado, 9-11 July, 1974.

28. W.P. Brown and J.E. Pearson, "Multidither COAT Compensation for Thermal Blooming and Turbulence: Experimental and Computer Simulation Results (U)," presented at the First Classified Conference on High Energy Laser Technology, San Diego, California, 1-3 October 1974.

29. G. Herzberg, Electronic Spectra and Electronic Structure of Polyatomic Molecules, Vol. III (Van Nostrand, New York, 1966).

30. D. Neuberger and A.B.F. Duncan, J. Chem. Phys. 22, 1693 (1954).

31. A.E. Douglas, J. Chem. Phys. 45, 1007 (1966).

32. W.A. Noyes and P.A. Leighton, Photochemistry of Gases (Dover, New York, 1966).

33. Dixon, J. Chem. Phys. 8, 157 (1940).

34. "COAT Measurements and Analysis," Hughes Technical Proposal 74M-4641/C8902-3, April 1974.

19. D.L. Fried J. Opt. Soc. Am. 56, 1372 (1966).

20. "COAT Planar Array," Technical Proposal 73M-3186/C8902, Hughes Research Laboratories, January 1973.

21. D.M. Chase, J. Opt. Soc. Am. 56, 33 (1966).

22. W.P. Brown, unpublished.

23. G.W. Reinhardt and S.A. Collins, Jr., J. Opt. Soc. Am. 62, 1526 (1972).

24. A.J. Huber, "Measurements of the Temporal Power Spectra of a Propagating 10.6 Micron Wave Front," RADC Report No. RADC-TR-74-44, February 1974. (AD777 259)

25. R.L. Fante, J. Cpt. Soc. Am. 56, 33 (1966).

26. W.B. Bridges, S. Hansen, L.S. Horwitz, S.P. Lazzara, T.R. O'Meara, J.E. Pearson, and T.J. Walsh, "Coherent Optical Adaptive Techniques," J. Opt. Soc. Am. 64, 541 (1974), abstract only.

27. J.E. Pearson, W.B. Bridges, L.S. Horwitz, T.J. Walsh, and R.F. Ogrodnik, "Atmospheric Turbulence Compensation Using Coherent Optical Adaptive Techniques," presented at the OSA Topical Meeting on Optical Propagation Through Turbulence, Boulder, Colorado, 9-11 July, 1974.

28. W.P. Brown and J.E. Pearson, "Multidither COAT Compensation for Thermal Blooming and Turbulence: Experimental and Computer Simulation Results (U)," presented at the First Classified Conference on High Energy Laser Technology, San Diego, California, 1-3 October 1974.

29. G. Herzberg, Electronic Spectra and Electronic Structure of Polyatomic Molecules, Vol. III (Van Nostrand, New York, 1966).

30. D. Neuberger and A.B.F. Duncan, J. Chem. Phys. 22, 1693 (1954).

31. A.E. Douglas, J. Chem. Phys. 45, 1007 (1966).

32. W.A. Noyes and P.A. Leighton, Photochemistry of Gases (Dover, New York, 1966).

33. Dixon, J. Chem. Phys. 8, 157 (1940).

34. "COAT Measurements and Analysis," Hughes Technical Proposal 74M-4641/C8902-3, April 1974.

MISSION
of
Rome Air Development Center

RADC is the principal AFSC organization charged with planning and executing the USAF exploratory and advanced development programs for electromagnetic intelligence techniques, reliability and compatibility techniques for electronic systems, electromagnetic transmission and reception, ground based surveillance, ground communications, information displays and information processing. This Center provides technical or management assistance in support of studies, analyses, development planning activities, acquisition, test, evaluation, modification, and operation of aerospace systems and related equipment.

Source AFSCR 23-50, 11 May 70